Max Born Institute

Ultrafast Soft Mode Dynamics in Ferroelectrics studied with Femtosecond X-Ray Diffraction

DISSERTATION

zur Erlangung des akademischen Grades

Dr. rerum naturalium

(Dr. rer. nat.)

im Fach Physik

eingereicht an der

Mathematisch-Naturwissenschaftlichen Fakultät

Humboldt-Universität zu Berlin

von

Herr Dipl.-Phys. Antonio Andrés Hernández Salvador

Präsidentin der Humboldt-Universität zu Berlin:
Prof. Dr.-Ing. Dr. Sabine Kunst

Dekan der Mathematisch-Naturwissenschaftlichen Fakultät:
Prof. Dr. Elmar Kulke

Gutachter:

1. Prof. Dr. Thomas Elsässer
2. Prof. Dr. Matias Bargheer
3. Prof. Dr. Oliver Benson

Tag der mündlichen Prüfung: **18.12.2019**

Abstract

Ferroelectrics are an area of current research, with important technological applications such as ferroelectric random access memories, infrared cameras or medical ultrasound equipment. This class of crystalline solids do not commonly only exhibit a ferroelectric phase, but rather go through an abundant variety of para- and ferroelectric phases that depend on the temperature. The ferroelectric phases present a spontaneous electric polarization even in the absence of an external field, in contrast to paraelectric phases and also exhibit a hysteresis loop in analogy to ferromagnets. This macroscopic feature has its origin in their peculiar electronic structure, which results from a rich diversity of lattice geometries and complex microscopic charge distributions. At the atomic level, however, the intricate characteristics of ferroelectrics are only partially understood. The link between microscopic charge distributions and macroscopic electric polarization poses a crucial question to be solved. The interplay of charge dynamics and lattice excitations are still unresolved on atomic length and time scales. In this thesis, femtosecond X-Ray powder diffraction is used to find questions for these opened questions. This method allows for the experimental determination of time-resolved charge density maps from where the structural, charge and polarization dynamics are can be derived. These maps are determined for photoexcited ferroelectric ammonium sulphate just below its Curie temperature. Data analysis has revealed a newly discovered low frequency lattice oscillation with a 3ps period and sub-picometer nuclear displacements that is related to periodic charge relocations on a 100pm length scale, which is a feature indicative of soft mode behavior. Finally, the dynamics of the variation of polarization are derived for the first time, showing an oscillatory reversal of polarity that holds potential for ultrafast switching applications.

Zusammenfassung

Ferroelektrische Materialien sind ein Schlüsselbereich der aktuellen Forschung und weisen zahlreiche wichtige technologische Anwendungen auf. Diese Klasse kristalliner Feststoffe zeichnet sich üblicherweise durch eine Vielzahl von para- und ferroelektrischen Phasen auf. Letztere sind dadurch charakterisiert, dass sie auch in Abwesenheit eines äußeren Feldes eine spontane elektrische Polarisation aufweisen. Diese Eigenschaft hat ihren Ursprung in der besonderen elektronischen Struktur ferroelektrischer Materialien, die sich aus einer großen Vielfalt von Gittergeometrien und mikroskopischen Ladungsdichteverteilungen ergibt. Auf atomarer Ebene sind die komplexen Eigenschaften der Ferroelektrika bis jetzt jedoch nur teilweise verstanden. Insbesondere die Verbindung zwischen mikroskopischen elektronischen Ladungsverteilungen und der daraus resultierenden makroskopischen elektrischen Polarisation wirft eine entscheidende, momentan noch offene Frage auf. Die Ladungsdynamik und ihr Zusammenspiel mit Gitteranregungen, insbesondere Softmoden, sind auf atomaren Längen- und Zeitskalen ungelöst. In dieser Arbeit wird das Potenzial der Femtosekunden-Röntgenpulverbeugung aufgezeigt, diese Frage zu adressieren. Diese Methode ermöglicht im Rahmen dieser Arbeit die Bestimmung transienter elektronischer Ladungsdichtekarten für das prototypische ferroelektrische Ammoniumsulfat direkt unterhalb seiner Curie-Temperatur nach einer optischen Anregung. Die Analyse der experimentellen Daten deckte eine bislang unbekannte niederfrequente Gitteroszillation mit einer Periode von 3 ps und nukleare Verschiebungen im Sub-Picometer-Bereich auf, die Ladungsverschiebungen auf einer 100-pm-Längenskala induzieren. Dies sind klare Merkmale, die auf die Anregung einer Softmode hinweisen. Schließlich wird zum ersten Mal die Dynamik der makroskopischen Polarisationsänderung abgeleitet, die eine oszillatorische Umkehr der Polarität aufweist und für ultraschnelle Schaltanwendungen geeignet ist.

Contents

Chapter 1

Introduction

The motivation of this work is to further the knowledge of lattice structural, charge density and polarization dynamics in the photoexcited prototypical ferroelectric ammonium sulphate. Ferroelectric materials are a key area of current research, with important technological applications such as ferroelectric random access memories, infrared cameras or medical ultrasound equipment. This class of crystalline solids do not commonly only exhibit a ferroelectric phase, but rather go through an abundant variety of para- and ferroelectric phases that depend on the temperature. The ferroelectric phases are characterized by presenting a spontaneous electric polarization even in the absence of an external field, in contrast to paraelectric phases ([1–3]), and also exhibit a hysteresis loop in analogy to ferromagnets. This macroscopic feature has its origin in the peculiar electronic structure, which results from a rich diversity of lattice geometries and complex microscopic charge density distributions.

Transitions between the ferro- and paraelectric phase occur at a critical transition temperature (or Curie temperature), T_C, being ferroelectric below it and paraelectric above it, although in general, the phase transitions can be triggered by several means, e.g., thermally, or also by applying an external mechanical stress or an external electric field ([4–6]). At the atomic level, however, the underlying mechanisms of ferroelectricity are only partially understood: The link between microscopic electronic charge distributions and the macroscopic electric polarization is not entirely understood and poses a crucial question to be solved ([7, 8]).

The crucial question is that there is no clear understanding of how lattice dynamics relate to polarizations dynamics. In this sense, comprehensive theoretical work by Resta and others has demonstrated that, in contrast to initial simplistic conceptions, the classical macroscopic polarization in a crystal, $\mathbf{P}$, cannot be derived uniquely from the knowledge of the periodic equilibrium charge distributions in a lattice ([9–11]). Although the macroscopic polarization is the basic quantity in the phenomenological description of dielectric media, one should only consider the *polarization variation*, $\Delta\mathbf{P}$, between two different states of the crystal which results from a variation of the charge density, $\Delta\rho(r, \lambda)$, (or equivalently a microscopic current) as a function of a certain external parameter λ. In the case studied here, the parameter λ corresponds to time ([9]). The formalism developed by Resta and others ([11–14]) expresses the variation of polarization in terms of a quantum geometric (Berry) phase determined by the cell-periodic component of the electronic wavefunction ([15]). This approach has been used to calculate

the variation of macroscopic polarization between stationary states for various prototype ferroelectrics whereas, recently, this theoretical framework has been extended to allow for the determination of the variation of polarization between different states in a dynamical case ([16]), rather than just between stationary states.

Typically, time-dependent polarizations of ferroelectrics have been treated in the context of nuclear displacements in the crystal lattice. The relation between atomic rearrangements and electronic charge distributions is far from being understood ([17–19]). In this sense, the concept of a soft mode which exhibits a frequency that approaches zero in the vicinity of the phase transition temperature plays a key role. Cochran's Theory ([20, 21]) qualitatively describes macroscopic properties of the ferro- and paraelectric phases for certain crystalline materials, but the relation between transient macroscopic polarizations and the lattice motions is not described at a microscopic level, and experimental insight on related phenomena has remained very limited.

Although X-Ray diffraction has been successfully used to follow ultrafast structural changes ([22, 23]), so far only the X-Ray powder diffraction approach has been able to deduce microscopic transient electron densities with which this question can be addressed in a quantitative and direct way ([7, 8, 24, 25]). In a pump-probe scheme, a pump pulse can induce different effects, e.g., it can excite the crystal with a strong non-resonant electric field ([26]), it can generate lattice motions via resonant pumping ([27, 28]), or it can produce displacive phonon excitations in the lattice upon electronic excitation ([7, 23]). A hard X-Ray probe synchronized with the optical pump is diffracted from the excited sample, producing a diffraction pattern from where the transient electronic charge distribution is derived. In various ionic materials, this method has produced accurate understanding of the transient charge displacements and their relation with lattice motions ([7, 26, 29]).

In this thesis, ultrafast X-Ray powder diffraction is used to map the transient electron density linked to low-frequency lattice vibrations in the vicinity of the transition temperature for the prototypical ferroelectric ammonium sulphate $[(NH_4)_2SO_4]$ and to address the problem of the relation between the transient microscopic electronic dynamics and the macroscopic polarization.

.

Outline

The thesis is organized as follows:

In Chapter 2 the general principles of ferroelectricity are reviewed. Subsequently follows a discussion of the main ferroelectrics, their structures, the mechanisms that govern their phase transitions, their applications in science and technology, and the role that ammonium sulphate plays among them.

In Chapter 3, powder diffraction and the most important mechanisms of absorption and scattering of X-Rays by matter are discussed. Subsequently, the kinematical theory of diffraction which models the intensity of weakly scattered X-Rays from powder material is described. This chapter ends with a discussion on how the transient changes of the electron density can be reconstructed from the measured variation of diffracted X-Ray intensity.

In Chapter 4, the femtosecond pump-probe experimental set-up used to study the transient structural changes in photoexcited ferroelectric ammonium sulphate is presented. Subsequently, the Maximum Entropy Method is explained along with the methodology used to calculate the transient charge density maps that reveal the structural dynamics in the crystal.

In Chapter 5, the experimental results for photoexcited ferroelectric ammonium sulphate are presented. Finally, the analysis of the charge density maps is given, and the new physical insight and conclusions are discussed.

Chapter 2

Ferroelectricity and the Physics of Soft Modes

In this chapter, the general principles of ferroelectricity are reviewed, along with Cochran's theory of displacive ferroelectricity, and the crystallographic structure and properties of ammonium sulphate.

2.1 Introduction to Ferroelectric Materials

Ferroelectrics consist of crystals that display a wide diversity of lattices and complicated microscopic charge density distributions ([1, 2]). They receive their name in analogy to ferromagnets, i.e., materials that can display a spontaneous magnetization even in the absence of an externally applied magnetic field, and also exhibit a hysteresis loop. Ferroelectrics are polar materials that present a so-called *remnant or spontaneous electric polarization*, P_S, which has its origin in their different complex electronic structures, and that can be oriented in at least two different equilibrium positions in the absence of an externally applied electric field. These two different thermodynamically metastable polarization states can be switched back and forth by applying a sufficiently strong external electric field ([1, 30]). There exists a certain minimum threshold field necessary to achieve the switching, which is called the *coercive field* ($\mathbf{E}_C$). This mechanism happens on length scales larger than the unit cell and, usually, is associated to a growth and/or shrinking of domains through the displacement of domain walls as discussed in the work by Lichtensteiger, Dawber and Triscone ([31]), and Paruch and Giamarchi ([32]).

Another characteristic property is that, structurally, very different ferroelectric materials can present different phases associated to a critical temperature, T_C, where the material is ferroelectric below T_C and paraelectric above it.

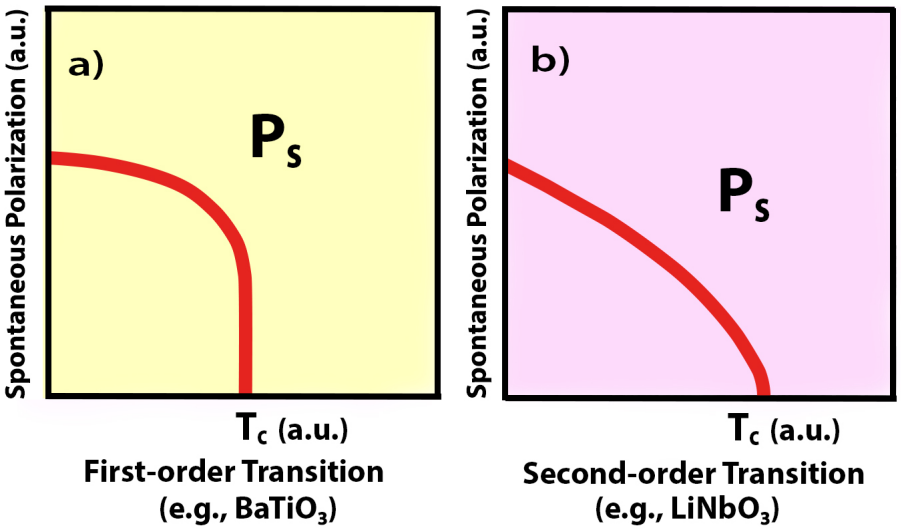

Figure 2.1: Schematic drawing of the temperature dependence of the spontaneous polarization (P_S, order parameter) for a first- and second-order para- to ferroelectric transition (figures a and b, respectively, [33]).

The phase transition can be classified as being of first or second order (Fig. 2.1). For the first-order type, the spontaneous polarization varies discontinuously during the transition with a sudden drop at $T = T_C$, while for the second-order type, the spontaneous polarization varies continuously. The prototypical ferroelectrics Barium Titanate ($BaTiO_3$) and Lithium Niobate ($LiNbO_3$) are examples of materials with a first- and second-order phase transitions, respectively ([33]). It is important not to confuse ferroelectrics with *electrets*, which are materials that do not present different metastable states, and are the electric equivalent to magnets ([34]). The para-to-ferroelectric phase transition of ammonium sulphate corresponds to a first-order transition, whereas a typical characteristic dielectric constant divergence takes place in a narrow temperature interval around the transition temperature, $T_C = 223K$ ([35] and Fig. 2.11).

The classical electric classification of materials is presented in Fig. 2.2(a) according to the polarization that they display (ordinate) in response to an applied external electric field (abscissa). In this representation, the dielectric permittivity, i.e., the capacity of a material to get polarized under the influence of an applied electric field, corresponds to the slope of the curve. The three existing types of materials according to their electric properties are represented: dielectrics (brown line), paraelectrics (blue curve) and ferroelectrics (orange curve). Dielectric materials are the most common and correspond to electric insulators, which experience an induced linear polarization under the effect of an external applied electric field. Paraelectrics show a linear polarization only when the applied electric field is relatively weak, yet beyond a certain threshold the paraelectric material saturates and its response is a decreasing variation of polarization. Ferroelectrics, finally, present a spontaneous polarization even in the absence of applied external electric field, $P_s(0) \neq 0$, where there exist two possible orientations for its vector, $\mathbf{P}_s$ and -$\mathbf{P}_s$, that can be switched by applying a strong enough electric field. The graphical

representation of this effect produces the characteristic so-called *hysteresis loop* where the coercive field and spontaneous polarization correspond to its crossings with the abscissa and ordinate, respectively.

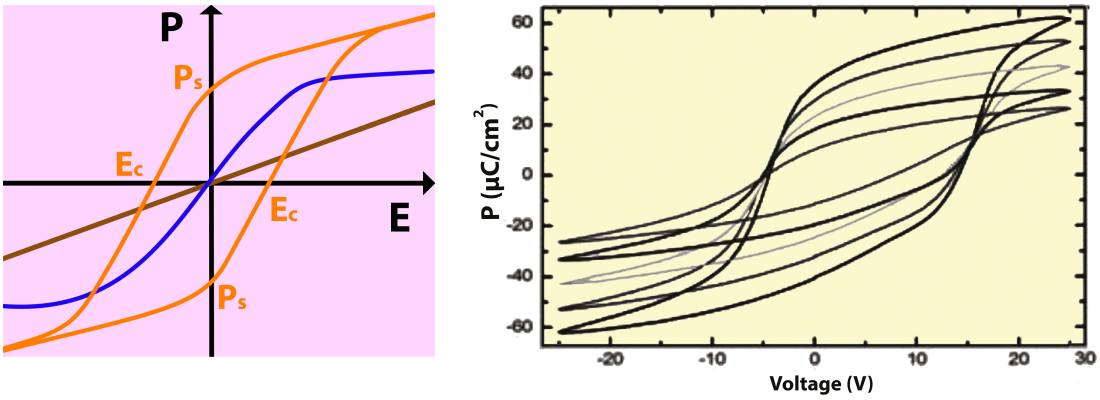

(a) (b)

Figure 2.2: Fig.2.2(a): polarization response (**P**) under the effect of an applied external electric field (**E**) in dielectrics (brown line), in paraelectrics (blue curve), and in ferroelectrics (orange curve, also known as 'hysteresis loop'). In Fig.2.2(b), one can see the experimental hysteresis loops (represented in a Polarization-Voltage scheme) for various $PbTiO_3/SrTiO_3$ superlattice samples with different spontaneous polarizations ([31]). In its canonical form (2.2(a)), the hysteresis loop is symmetric, and the coercive field and the spontaneous (or remnant) polarization (P_S) can be easily calculated. However, there exist a number of potential pitfalls when measuring the electrical properties of a ferroelectric since, some times, the material can only be assessed when it is integrated in a device (typically a capacitor). Any evaluation, under this conditions, actually involves the estimation of a whole system. Therefore, different techniques have had to be developed to avoid that the electrical responses of the other electric elements, in which the ferroelectric is integrated, dominate in the measurement. Figure 2.2(b) shows an experimentally measured hysteresis loop.

Nonetheless, the graph in Fig.2.2(a) is only a schematic representation, and it is crucial to exercise due care when measuring the ferroelectric properties of a material. Nowadays, most ferroelectric materials are used in the form of thin-film ferroelectrics on a substrate, which commonly will not be perfectly insulating, and many factors, e.g., crystal defects, grain boundaries, or conduction processes (Schottky injection, Fowler-Norheim tunnelling) can produce leakage currents making it difficult to differentiate a simple dielectric from a true ferroelectric ([2]). In other occasions, ferroelectrics are fabricated in the form of an integral device (most typically a capacitor) with which its properties cannot be directly measured, and any real assessment has to consider a whole electric system that involves wires, electrodes, interfaces, etc. Some times, the responses of these other elements produce hysteresis artifacts ([2]) giving rise to ambiguous results that overshadow the real intrinsic properties of the ferroelectric material. Different solutions have been developed to solve this problem, e.g., the Sawyer-Tower circuit, which was the original method used to measure ferroelectric hysteresis in a material ([36, 37]).

Actually measured hysteresis loops for a number of Lead Titanate/Strontium Titanate superlattice samples ($PbTiO_3/SrTiO_3$) are given as a descriptive example in Figure 2.2(b) ([31]). As can be appreciated, the representation is noticeably different from the perfectly symmetric curve in the theoretical hysteresis loop in Fig. 2.2(a).

2.1.1 The wide variety of Ferroelectric Materials

By the year 2007, approximately 700 ferroelectric materials had already been identified. Some of the most important families are:

- Perovskite oxides. This terminology designates the compounds that have the crystal structure of the perovskite mineral ($CaTiO_3$, calcium titanate), i.e., *perovskite structure*. It is the largest, most studied and technologically important family of ferroelectrics. Its main technological representative is the prototypical barium titanate, $BaTiO_3$, while other important examples are potassium niobate ($KNbO_3$), lead titanate ($PbTiO_3$), or strontium titanate ($SrTiO_3$), ([31]).

- Lithium niobate ($LiNbO_3$) and analogous materials, e.g., bismuth ferrite ($BiFeO_3$) or lithium tantalate ($LiTaO_3$), ([31]).

- Layered oxides, e.g., the *Aurivillius phases* that consist of layered bismuth oxides ([31, 38]).

- Magnetic ferroelectric oxides, which are characterized for being both ferroelectric and ferromagnetic, e.g., ferroelectric hexagonal manganites, $YMnO_3$ ([39–41]).

- Electronic ferroelectrics, characterized by the fact that electronic degrees of freedom and electronic interactions are directly accountable for the electric polarization and ferroelectric transition, e.g., the rare-earth compound SmB_6 ([41]).

- Non-bulk ferroelectrics in which, contrarily to expected, a switchable polarization for thicknesses in the order of a few nanometers is maintained ([42]).

- Other ferroelectric oxide families that cannot be classified as any of the previous, e.g., boracites, tungsten bronzes, $Li_2Ge_7O_15$, $Gd_2(MoO_4)_3$, $Pb_5Ge_3O_{11}$, R_3 Sb_5O_{12}, $LiNaGe_4O_9$, Mn_3TeO_6, and $BaAl_2O_4$ ([1, 31]).

Some of the most relevant prototype crystalline materials displaying ferro- and paraelectric phases are mentioned now, along with their phase transition temperatures and the values of their spontaneous polarization. The purpose is to have a reference with which to compare the experimental values for the ferroelectric ammonium sulphate studied in this thesis :

- **Barium titanate** ($BaTiO_3$, perovskite): exhibits a paraelectric phase over 393K (cubic perovskite structure) and different ferroelectric phases under 393K (tetragonal phase), 278K (orthorhombic phase) and 183K (rhombohedral phase) with spontaneous polarization of $\sim 33\ \mu C/cm^2$, $\sim 36\ \mu C/cm^2$, and $\sim 27\ \mu C/cm^2$, respectively ([43, 44]).

- **Potassium niobate** ($KNbO_3$, perovskite): isostructural material with $BaTiO_3$ that exhibits the same sequence of phases with transition temperatures at 701K (cubic-tetragonal), 488K (tetragonal-orthorhombic), and 223K (orthorhombic-rhombohedral), and spontaneous polarization in the tetragonal phase (701K-488K) of $\sim$35 $\mu C/cm^2$ ([43, 44]).

- **Lead titanate** ($PbTiO_3$, perovskite): exhibits a transition from ferroelectric to paraelectric at 760K, and presents one of the highest spontaneous polarization for ferroelectrics with ~ 75 $\mu C/cm^2$ at room temperature ([43, 44]).

- **Lihitum niobate** ($LiNbO_3$): the para- to ferroelectric transition takes place at the critical temperature 1483K, with a spontaneous polarization of $\sim$ 71 $\mu C/cm^2$ at room temperature ([43, 44]).

2.1.2 Development and Applications of Ferroelectric Materials

Ferroelectricity was initially observed in hydrogen-bonded materials such as potassium sodium tartrate (first ferroelectric ever identified in 1920 by J. Valasek, also known as Rochelle Salt, $KNaC_4H_4O_6{\cdot}4H_2O$, [45]) and potassium dihydrogen phosphate (KDP, KH_2PO_4, [29]). However, it was not until 1943, that the identification of the structure of the much simpler perovskite oxides (e.g., $BaTiO_3$, [46]) spurred deeper theoretical work on the origin of ferroelectricity, and allowed for first-principles quantitative modelling. In direct consequence, a long-standing industry of electronic ceramics was born, with billions of $BaTiO_3$ capacitors still manufactured in our days. Later, by the 1970s, the long-lasting period of identification of new ferroelectric materials stagnated, and the most interesting scientific challenge in those days consisted in the discovery and modelling of new phase transitions ([47]). The possibility of growing single crystals was prohibitively expensive in those years and, in general, ferroelectrics in technological applications were limited to those that only included bulk ceramics. Even in that case, devices as pyroelectric detectors and sonars, were successfully developed.

By the year 1984, the situation changed dramatically with the introduction of the new submicrometer thin-film single crystals. Thin-films allow for the use of coercive fields of less than 5 volts, which makes it possible to integrate them into semiconductor silicon chips. Although much of the theory required to understand thin-film ferroelectrics comes directly from the studies on bulk ferroelectrics, to fully explain their behavior it was necessary to develop a whole new field of physics. Presently, there exists a whole industry completely dedicated to the manufacture of thin-film ferroelectric capacitors ([2]), which have very different technological applications, such as ferroelectric random access memories (FeRAMs), medical ultrasound equipment, fire detection sensors, infrared cameras, fuel injectors for diesel motors or vibration sensors ([3]).

2.2 Cochran's Theory of Displacive Ferroelectricity

Cochran's theory of displacive ferroelectricity is a phenomenological concept based on the Clausius-Mossotti model ([48, 49]) where the presence of electronic charge is clearly identifiable and bound to localized ionic units ([10, 11]). It can be summarized as a core-shell model based on a lattice of massive balls that correspond to atoms and electron shells, which are connected by a network of elastic springs that model the bonds (Fig.2.4).

This model, however, presents fundamental inexactitudes. By the beginning of the 1990s, very good first-principles electron-density maps were available, in particular for selected ferroelectric perovskites ([49, 50]), but the classical vision of polarization based on Cochran's model of lattice dynamics failed to connect the microscopic charge densities in a crystal with its macroscopic polarization. The reason for this proved to be the evidence for charge transfer among different ions upon excitation ([26]). For typical ferroelectric oxides, the bonds resulting from the electronic charge distribution have a mixed ionic and covalent character ([50]) with displacements of localized electronic charge (which nonetheless remains strongly-bound around the nuclei), and completely delocalized electronic net charge transfer among the different ions. In this sense, Cochran's theory cannot explain materials that present net charge transfer among ions. Nevertheless, Cochran's theory of lattice dynamics is able to successfully model certain properties for a number of ferroelectric materials, as shall be seen in the following.

In this section is reviewed the concept of soft mode and its historic development. Subsequently, a classical simple model based in Cochran's theory is presented. This model is able to model satisfactorily the temperature-dependence of the soft mode frequency, the divergence of the dielectric constant, and the phenomenon of *polarization catastrophe* .

In the final part of this section, it is discussed how the variation of macroscopic polarization can be fully resolved making use of the experimental time-resolved charge density maps by means of the *modern theory of polarization*, the concept of Berry's phase, and the methodology recently developed in Ref. [16].

2.2.1 Historic development of Cochran's Theory

Cochran put forward his theory of ferroelectricity for the first time in 1959 ([20]), and expanded it greatly in 1960 ([21]). It states that the phase transitions in certain ferroelectric (and also anti-ferroelectric[1]) crystals are the result of an instability against a particular temperature-dependent normal mode called *soft mode* that can be treated as a problem in lattice dynamics. More in particular, Cochran precised that at a second-order ferroelectric transition (where the dielectric constant diverges), the soft mode

[1] Antiferroelectricity is closely related to ferroelectricity, being its relationship analogous to that of antiferromagnetism and ferromagnetism. Antiferroelectric crystals are composed by an array of electric dipoles, yet with the particularity that adjacent dipoles are oriented in opposite directions, in contrast to ferroelectric materials where all the dipoles point in the same direction. In this sense, since adjacent dipoles cancel each other out, its spontaneous polarization is reduced to zero ([51, 52]).

must consist of a transverse optical lattice normal mode whose frequency goes to zero as the transition is approached. The characteristics of soft modes are described in detail in section 2.2.2, here are only mentioned some of the more relevant hallmarks of the theoretical work on lattice dynamics and soft modes developed by previous authors on which the Cochran's theory is grounded.

The soft mode concept was rediscovered by several authors at different occasions, but the earliest mention in history of what would later be known as soft mode, corresponds to a structural alpha-beta phase transition in quartz described by Raman and Nedungadi in 1940 ([53, 54]). Even with this early experimental detection, the soft mode concept made a slow entrance into modern physics. Power demonstrated in 1942 that a crystal with a face-centered cubic structure and one atom in the unit cell, e.g., NaCl, is stable for all homogeneous deformations ([55]). Force constants between nearest neighbour atoms where taken into account for the first time in his work, which would later prove to be an advance in the theory.

In 1949, Fröhlich in his work *Theory of Dielectrics* ([56]) invoked for the first time the Lyddane-Sachs-Teller relation that helps modelling the behavior of an ionic crystal for the case of long wavelengths (zero wavevector, $\mathbf{k} = 0$). It gives the ratio of the frequency of the longitudinal optical lattice normal mode, ω_{LO}, to the natural frequency of the transverse optical lattice normal mode, ω_{TO} and connects it with the dielectric constant ([57]):

$$\frac{\omega_{LO}^2}{\omega_{TO}^2} = \frac{\varepsilon_{st}}{\varepsilon_{\infty}} \tag{2.1}$$

where ε_{st} corresponds to the static dielectric constant (often also denoted as $\varepsilon(0)$) and ε_{∞} corresponds to the dielectric constant for frequencies in the visible range (often also denoted as $\varepsilon(\omega_s)$). The LST relation was used to prove that the *divergent dielectric constant*, which occurs in the polarization catastrophe, must be associated with a transverse optical normal mode whose frequency tends to zero. Later, in 1954, Born and Huang gave a full account on the stability in crystals in their classical work *Dynamical Theory of Crystal Lattices* ([58]). They concluded that, a crystal is stable for all small deformations if, and only if, all the normal modes have real frequencies.

Nonetheless, even with these advances, by the beginning of the decade of the fifties, research in ferroelectricity was limited to phenomenological theories or consisted of attempts at microscopic theories for particular crystal structures. Building on these previous works, Cochran stimulated the interpretation of ferroelectricity as a lattice dynamics problem, and the corresponding ideas he formulated about soft modes would be proven to be true in the following years. He started developing his theory by considering an ionic crystal with a simple diatomic cubic structure (CsCl or NaCl type) and establishing dynamical stability conditions for its lattice under small deformations. Even this simple model exhibits phase-transition characteristics that are surprisingly similar to those of barium titanate. Subsequently, Cochran would extend his theory with satisfying results to ferroelectric transitions in other crystals with cubic structure and to anti-ferroelectric transitions in diatomic crystals.

Somewhat later, in 1960, the lattice dynamics theory was extended by Woods et al. ([59]) to include ion polarizability and the fact that there exists a short-range *overlap force* between ions that depends on their state of polarization and vice versa. This theory successfully explained the dispersion relations for germanium (presented in the works of Brockhouse and Iyengar in 1958, [60]), and sodium iodide (presented in the works of Woods et al. in 1960, [59]). This proved that the dipole moment of an atom in a crystal is not only determined by the effective field, but also by the displacements of ions from the equilibrium positions and the dipole moments of neighbouring atoms. All the previous works that had attempted to explain the theory of ferroelectricity had not considered this feature, which in the following years would prove to be a successful model for a number of ferroelectric transitions.

The first experimental confirmation of the existence of a soft mode was the infrared study of strontium titanate ($SrTiO_3$) by Barker and Tinkham in 1962 ([61]). In the same year, Cowley ([62, 63]) confirmed the correctness of the soft mode concept with his neutron scattering experimental work on $SrTiO_3$ where, in particular, one of the optical modes with wavevector zero presented a soft mode behavior. Throughout the rest of the sixties, the recognition of the fundamental relation between lattice dynamics and ferroelectricity led to an intense experimental study of soft modes via X-Ray diffraction, neutron scattering and, Raman and IR Spectroscopy ([64, 65]). Some of the more notorious studied ferroelectrics have been the perovskite group (e.g., $BaTiO_3$, $KNbO_3$, $PbTiO_3$, etc.), perovskite-related materials (like $LiNbO_3$), and hydrogen-bonded ferroelectrics (like those belonguing to the KDP family, [65]).

To conclude this section, it is also interesting to remark that the theoretical work by Cochran ([21]) and Cowley ([66]) also focused on understanding the mechanism of the para-to-ferroelectric structural transition, which may be classified into two groups according to the type of transition that they undergo, i.e., Displacive Transitions ([67]) and Order-Disorder Transitions ([68])

2.2.2 Characteristics of soft modes

One of the crucial achievements of Cochran's theory is that, for certain crystals, ferroelectricity can be treated as a problem in lattice dynamics, where the phase transitions are the result of an instability against a particular temperature-dependent unstable normal mode called *soft mode*. The great value of the soft mode concept is that, it consists of an unified simple microscopic theory to describe ferroelectricity (and also antiferroelectricity) that is not affected by the potential complexity of the different crystal structures. It takes advantage of their common features and permits to focus in the study of the relation between crystals and their associated structural phase transitions.

The characteristic properties of soft modes can be summarized in the following ideas:

- Soft modes present a frequency that tends to zero as a structural phase transition is approached. This occurs typically when the temperature approaches the change of phase temperature, T_C, in

a para-to-ferroelectric phase transition. When T_C is finally reached, the normal mode of vibration *freezes*, i.e., the crystal's stability against the soft mode of vibration is lost, and the atoms become frozen in a different ferroelectric structure that is characterized by having a finite dipole moment and a lower symmetry. The lower symmetry concept is crucial, because if the transition was to take place between crystal structures of the same or higher symmetry, the symmetry breaking dipole (i.e., asymmetric electronic distribution) that originates the spontaneous polarization in the ferroelectric state could not exist.

- The decrease of the soft mode frequency when the temperature tends towards T_C occurs concomitantly with a strong divergence of certain magnitudes such as the dielectric constant, the spontaneous polarization, or the specific heat ([35, 69]). This phenomenon is known as polarization catastrophe in analogy to ferromagnetic transitions, where the magnetic susceptibility is the magnitude that is expected to diverge. Although, it is not the general case, Cochran has shown that the transverse optical soft mode ($\mathbf{q} = 0$) with lowest frequency follows the relation ([21]):

$$\omega_{TO} \sim (T - T_C)^{1/2}$$

whenever the dielectric constant obeys the Curie-Weiss law:

$$\varepsilon_{st} \sim \frac{1}{(T - T_C)}$$

- Soft modes present a very strong coupling of the ionic vibrational and electronic degrees of freedom. This feature produces strong local electric fields that induce a spatial relocation of the electronic charge over comparatively large distances. In this sense, sub-picometer atomic displacements can induce rearrangement of electronic charge over much larger distances in the 100pm range. This behavior has been revealed by ultrafast X-Ray powder diffraction experiments in which different polar materials were studied under non-equilibrium conditions ([7, 8, 24, 26, 29]). From that previous research, it can be concluded that for soft modes, both the phenomena of frequency decreasing and strong dielectric constant divergence occurring when $T \rightarrow T_C$, are caused by the large contribution of the electronic charge transfer ([20, 21]).

For illustrative purposes, Fig. 2.3 shows the phonon spectrum of strontium titanate ($SrTiO_3$) that corresponds to an archetypical situation in the context of the presence of soft modes (even if $SrTiO_3$ is anti-ferroelectric and not ferroelectric). The figure shows that the lowest optical phonon branch is soft in the region of the origin (i.e., long wavelength components of the optical phonon, $\mathbf{q} = 0$), but quickly stiffens as $\mathbf{q}$ increases, and the modes are only strongly temperature-dependent over a small region of that zone. As can be appreciated, there exists also a certain softening mode at the central region, and

at the Brillouin zone edge. For the anti-ferroelectric $SrTiO_3$, the dielectric constant also becomes very large in vicinity of the phase transition.

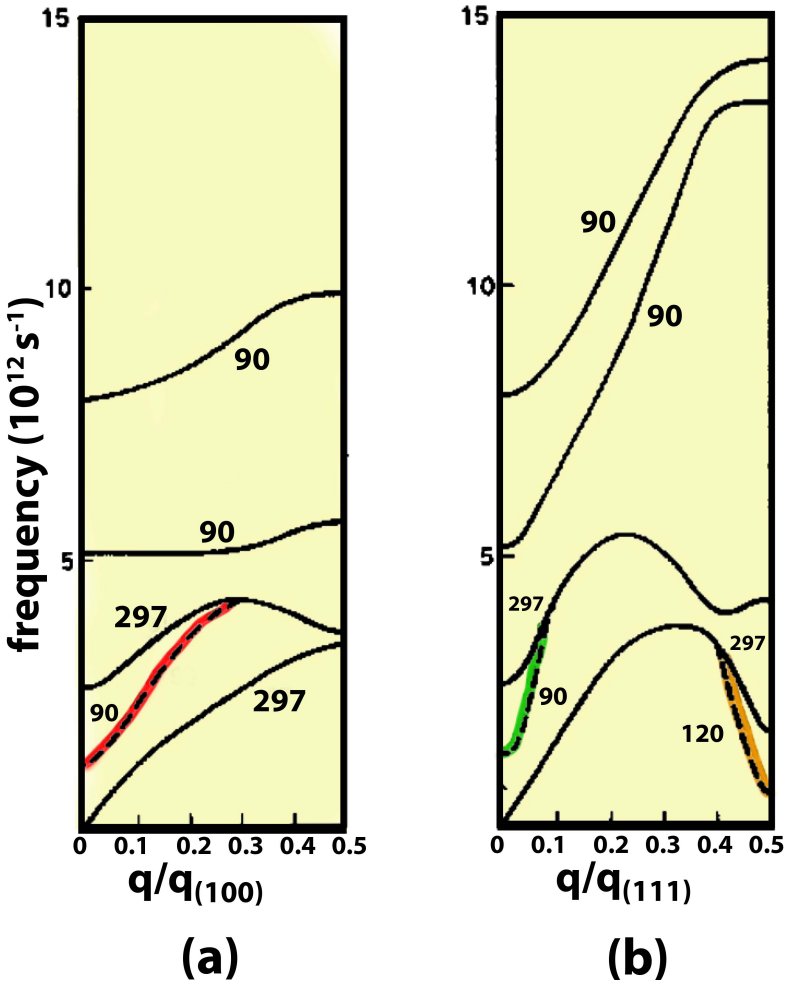

Figure 2.3: Phonon dispersion relations for strontium titanate, $SrTiO_3$, measured at different temperatures for those vibrations where an important variation with the temperature is observed. It is important to point out that there can exist softening of the optical mode at both the near $\mathbf{q} = 0$ and at the zone boundary phonon, $\mathbf{q} = (\pi\ /a)(111)$, ([70]). For $SrTiO_3$ in particular, sub-figure (a) shows that the lowest optical phonon branch in direction $\mathbf{q}/q_{100}$ is soft in the origin region (variation from T = 297K to T = 90K) which extends towards the central region. Sub-figure (b) shows analogously, that the lowest optical phonon branch in direction $\mathbf{q}/q_{111}$ is soft in the origin region (variation from T = 297K to T = 90K) and also shows a soft acoustic branch at the Brillouin zone edge (variation from T = 297K to T = 120K).

One last interesting characteristic to remark is that soft modes are optically active since they give rise to electrical polarizations and, henceforth, can be detected by means of optical spectroscopy in the spectrum of the dielectric permittivity. Spectroscopic studies of soft modes have proven a very powerful tool to investigate ferroelectric transitions ([71, 72]).

2.2.3 Core-Shell model

Cochran's theory of lattice dynamics can be conceptualized as a core-shell model based on a lattice of massive balls that correspond to atoms and electron shells connected by a network of elastic springs that model the bonds. Figure 2.4 shows the simplest example, although much more sofisticated approaches to complex ferroelectric crystals are possible.

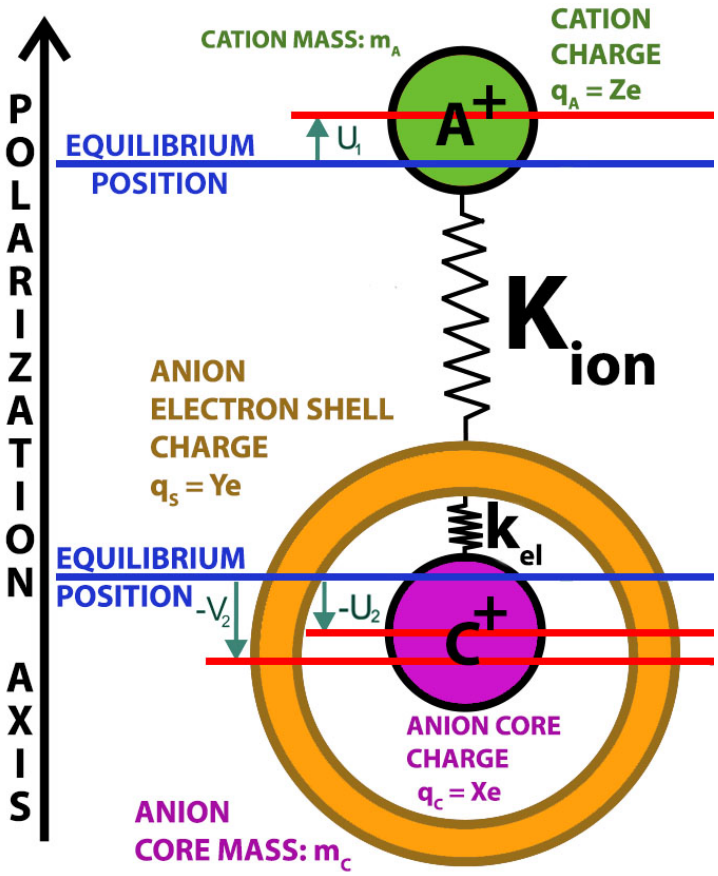

Figure 2.4: Simple core-shell model as defined in the Cochran's theory of lattice dynamics to explain ferroelectricity ([21]). The anion core (magenta) is polarizable and connected to its external electron shell (orange), which in its turn is connected to the cation (green). The bonds are modelled by two restoring forces with force constants k_{el} and K_{ion} ($K_{ion} \ll k_{el}$).

Cochran's theory of lattice dynamics can be understood as a zero-order model, in the sense that it does not attempt to account for real charge densities, which can flow to and from the different atoms and ionic units. Even so, for certain materials where the electronic charge is bound to the nuclei, it successfully explains certain aspects of ferroelectricity as the the phonon dispersion in the lattice, the dielectric constant divergence in the limit of the critical temperature, the polarization catastrophe or the existence of the so-called called soft modes, which contribute to explain the ferro- to paraelectric phase transition.

This theory accounts for one of the more relevant problems in this physics field given that, at this point, there are not enough ab-initio quantum calculations that allow for an assessment of the charge densities in the crystal ground or electronically excited states.

A brief summary of the simplest model of Cochran's theory of lattice dynamics for ferroelectricity is given here, while the details of the treatment of this formalism are given in his original scientific paper ([21]). The nomenclature of the classical shell model is used as defined by Cochran because it is the most straightforward approach.

Derivation of the transverse and longitudinal optical mode frequencies

The mathematical derivation for crystal stability and lattice dynamics to model ferroelectricity proposed by Cochran in Ref. [21] is presented here, as it explains the dielectric constant divergence in the critical temperature, the polarization catastrophe and the concept of soft mode, that shall be used later to asses the experimental results obtained for ferroelectric ammonium sulphate.

The frequency of the transverse and longitudinal optical mode are deducted in an elementary way and, finally, the *polarization catastrophe* is discussed. Cochran proposes the combination of electronic polarizations (related to electronic relocations) and lattice polarizations (related to ionic displacements) within a common approach that describes the ionic displacements in terms of all the normal modes of the crystal lattice (including soft modes). The model consists of a basic classical ball-and-spring lattice concept (Fig. 2.4), where the electron shells are not fixed and can oscillate with the nuclei as centers of gravity. In the simple model explained here, it is a polarizable atom in a diatomic cubic crystal (e.g., the case of sodium chloride or caesium chloride with a face-centered cubic lattice) separated into cations (shown in green), the cores of the anions (shown in magenta) and the electronic shells of the anions (shown in orange), which are connected by elastic restoring forces. For simplicity, it is assumed that only the negative ion is polarizable, and that it is connected to its outer electronic shell by a restoring force of constant k_{el}, while the ions are coupled together by an elastic restoring force of constant K_{ion}. The two restoring force constants comply with the condition: $K_{ion} \ll k_{el}$.

To solve the problem analytically, the Coulomb forces are separated into long-range forces and short-range forces as proposed by Lorentz in his *Theory of the Local Field* ([73]), which relates the macroscopic polarization and the microscopic field acting on individual ions. In this sense, the long-range forces, which are assumed to act through the shell and not the core of the negative ion, are modelled by the Lorentz field: $\mathbf{E}^{L.R.}(\mathbf{r}) = \mathbf{P}(\mathbf{r})/3\varepsilon_0$. The short-range forces are modelled by elastic restoring forces: the inter-ionic force with constant K_{ion} that acts between the cation and the electronic shells, and the anion core-electron shell force with constant k_{el} that acts between the electronic shell of the anion and the cation. Taking this into account, the local field for the cubic crystal is defined as:

$$\mathbf{E}_{LOCAL}(\mathbf{r}) = \mathbf{E}(\mathbf{r}) + \frac{\mathbf{P}(\mathbf{r})}{3\varepsilon_0} \tag{2.2}$$

Cochran writes the equations of motion for the cation, the anion core and electronic shell by defining the displacement from their respective equilibrium positions ([21]). In this sense, $u_1(t)$, $u_2(t)$ and $v_2(t)$ stand for the deviation from their equilibrium position of the cation, of the anion core, and of the electron shell, respectively. By taking into account the previously mentioned local field corrections, and making use of classical mechanics, the following equations are derived. Eq. 2.3 and Eq.2.4, correspond to the equations of motion of the cation and of the anion core, respectively, and Eq. 2.5, specifies the equilibrium condition for the shells and nuclei:

$$m_{CAT} \cdot \ddot{u}_1 = K_{ion}(v_2 - u_1) + \frac{1}{3\varepsilon_0} \cdot PZe \tag{2.3}$$

$$m_{CORE} \cdot \ddot{u}_2 = k_{el}(v_2 - u_2) + \frac{1}{3\varepsilon_0} \cdot PXe \tag{2.4}$$

$$0 \approx m_{e^-Shell} \cdot \ddot{v}_2 = k_{el}(u_2 - v_2) + K_{ion}(u_1 - v_2) + \frac{1}{3\varepsilon_0} \cdot PYe, \;\; (m_{e^-Shell} \ll m_{CAT}) \tag{2.5}$$

where P corresponds to the polarization, m_{CAT} corresponds to the mass of the cation, m_{e^-Shell} to the mass of the anion electron shell, m_{CORE} to the mass of the anion core, Ze to the effective charge of the cation, Ye to the charge of the anion electron shell, Xe to the charge of the anion core, e to the electron charge (in S.I. units), and where the condition X + Y + Z = 0 ensures overall charge conservation. Also, it is important to mention that this approach makes use of the Born-Oppenheimer approximation, whereby the movement of electrons is decoupled from that of the nucleus based on the important mass difference between the two types of particles ([74]).

For simplicity, the direction of the wavevector **q** can be modelled as taking place along the axis [100], while the atoms displace in parallel to the axis [001]. The polarization is defined generically as a harmonic oscillation in this direction, $P(t) = \mathscr{P} \cdot \exp(i\omega t)$, where $\mathscr{P}$ corresponds to the maximum polarization, and taking into account its general definition must correspond to:

$$\mathscr{P} = (e/\Omega_{UC}) \cdot (ZU_1 + XU_2 + YV_2)$$

,

where Ω_{UC} is the unit cell volume.

To proceed now, an ansatz solution is established, i.e., an educated guess to find the solution of the physical problem based on previous mathematical experience. Under this approach, the motion solutions

are assumed to consist of a harmonic behavior of the displacements:

$$u_1(t) = U_1 \cdot \exp(i\omega t)$$

and

$$u_2(t) = U_2 \cdot \exp(i\omega t)$$

where U_1 and U_2 are the maximum displacements from the equilibrium position.

By substituting and rearranging the ansatz solutions $u_1(t)$, $u_2(t)$, and the polarization P(t) in the motion equations (Eq. 2.3 and Eq. 2.4), and in the electron shell equilibrium equation (Eq. 2.5), the following coupled system of equations is obtained:

$$m_{CAT} U_1 \omega^2 = \tilde{K}_{ion}(U_1 - U_2) - (i/3\varepsilon_0)\mathscr{P}\tilde{Z}e \tag{2.6}$$

$$m_{CORE} U_2 \omega^2 = \tilde{K}_{ion}(U_2 - U_1) + (1/3\varepsilon_0)\mathscr{P}\tilde{Z}e \tag{2.7}$$

with the effective values $\tilde{K}_{ion}$ and $\tilde{Z}$, instead of K_{ion} and Z:

$$\tilde{K}_{ion} = \frac{k_{el} K_{ion}}{k_{el} + K_{ion}} < K_{ion} \qquad \text{since} \quad K_{ion} \ll k_{el} \tag{2.8}$$

and

$$\tilde{Z} = Z + \frac{Y K_{ion}}{k_{el} + K_{ion}} < Z \qquad \text{since } Y < 0 \ (\textit{electronic charge is negative}) \tag{2.9}$$

It is crucially important to point out that the replacement of K_{ion} and Z by the effective values $\tilde{K}_{ion}$ and $\tilde{Z}$ does not come from the fact that the ions are polarizable under the effect of an electric field, but from the fact that dipoles are generated by the short-range forces during the coherent vibration of the lattice.

Combining $\mathscr{P} = (e/\Omega_{UC})(ZU_1 + XU_2 + YV_2)$, with the electronic shell equilibrium equation (Eq. 2.5), with the maximum amplitude for the polarization ($\mathscr{P} = (YeV_2)/\ \Omega_{UC}$, [75]), and considering the effect of an external harmonic electric field that has a frequency (p) high enough to move appreciably only

the electronic shell (i.e., $E(t) = \mathscr{E} \cdot \exp(-ipt)$, where $\mathscr{E}$ is the maximum amplitude), the electronic polarizability α_e of the anion can be derived (fully deducted in the original paper, Ref. [21]):

$$\alpha_e = \frac{\mathscr{P}\Omega_{UC}}{\mathscr{E}} = \frac{(Ye)^2}{k_{el} + K_{ion}} \tag{2.10}$$

By taking advantage of the Clausius-Mossotti formula ([76]), which connects the externally applied electric field with the local internal electric field, and relates the dielectric constant of a material to its polarizability, the following expression is obtained:

$$\frac{\varepsilon_r - 1}{\varepsilon_r + 2} = \frac{n\alpha}{3\varepsilon_0} \tag{2.11}$$

where $\varepsilon_r = \varepsilon/\varepsilon_0$ is the relative dielectric constant (or relative permittivity) of the material, n is a number density (number of molecules per cubic meter), and α is the polarizability (in SI-units: $C \cdot m^2/\Omega_{UC}$).

Since only the movement of electrons at high frequencies is considered, the relation that connects the electronic polarizability to the high-frequency dielectric constant, ε_∞, is defined by:

$$\alpha_e = \frac{3\Omega_{UC}\varepsilon_0}{1} \frac{(\varepsilon_\infty - 1)}{(\varepsilon_\infty + 2)} \tag{2.12}$$

Finally, by rewriting the expression of the polarization, substituting the value $\mathscr{P}$ into the two previously derived coupled equations (Eq. 2.6, and Eq. 2.7), and eliminating U_1 and U_2 (fully derived in the original paper, Ref. [21]), the frequency of the lowest transverse optical mode is retrieved :

$$\mu\omega_{TO}^2 = \tilde{K}_{ion} - \frac{(\varepsilon_\infty + 2)(\tilde{Z}e)^2}{9\Omega_{UC}\varepsilon_0} \tag{2.13}$$

where μ is the reduced mass, $\mu = \mathrm{m}_1\ \mathrm{m}_2/(\mathrm{m}_1 + \mathrm{m}_2)$.

The frequency of the lowest longitudinal optical mode, ω_{LO}, can be derived in an analogous fashion, with the particularity that, in this case the effect of the local Lorentz field, which arises from the combined effect of all the neighbouring dipoles in the crystal has to be included, i.e., $\mathbf{E}_{LOCAL}(\mathbf{r}) = \mathbf{P}(\mathbf{r})/\varepsilon_0$ ([77]). The longitudinal optical mode final expression is, accordingly, given by:

$$\mu\omega_{LO}^2 = \tilde{K}_{ion} - \frac{2(\varepsilon_\infty + 2)(\tilde{Z}e)^2}{9\Omega_{UC}\varepsilon_\infty\varepsilon_0} \tag{2.14}$$

Remarkably, other authors reached similar conclusions as Cochran by following different theoretical paths. In 1954, Born and Huang in his classic account of the quantum mechanical foundation of lattice dynamics, *Dynamical Theory of Crystal Lattices* ([58]), analogously derived the frequency of the longitudinal optical normal mode for wavevector $\boldsymbol{q} = 0$ (lowest longitudinal mode), by accounting for the presence of a macroscopic field, -$\mathbf{P}/\varepsilon_0$, in addition to the local Lorentz field $\mathbf{P}/3\varepsilon_0$, which stems from the average field of all neighbouring dipoles in a solid.

Interestingly, the equations defining the frequencies of the longitudinal and transverse optical modes (Eq. 2.13 and Eq. 2.14) were also obtained in 1960 by Woods ([59]) as special cases of the dispersion relation, $\omega = \omega(\mathbf{q})$, that applies when $\mathbf{q}$ corresponds to a symmetry direction. His theory gave good agreement with the dispersion relations determined empirically for sodium iodide (NaI).

2.2.4 Soft mode charge relocation

To study the electronic contribution to electric currents induced by soft modes, the relation between the distances U_1-U_2 and V_2-U_2 must be analysed. These values represent, respectively, the nuclear motions connected to the soft mode and the distance of the electron shell to the anion core (understood as a benchmark for the electronic charge relocation).

The variables U_1 - U_2 and V_2 - U_2 can be derived from the equations that describe the polarization:

$$\mathscr{P} = (V_2 - U_2)\frac{Ye_0}{\Omega_{UC}} + (U_1 - U_2)\frac{Ze_0}{\Omega_{UC}} \tag{2.15}$$

and the balance of forces:

$$\left(\frac{Ye_0}{3\varepsilon_0}\right)\mathscr{P} - (V_2 - U_2)(k_{el} + K_{ion}) + (U_1 - U_2)K_{ion} = 0 \tag{2.16}$$

By introducing the expression of the polarization from Eq. 2.15 into Eq. 2.16, substituting the electronic polarizability of the anion, and re-arranging the terms, the expression that shows how the electronic shell motion is related to the ionic displacement is retrieved:

$$(V_2 - U_2) = \left(\frac{\frac{K_{ion}}{k_{el}+K_{ion}} + \frac{\alpha_e}{3\Omega_{UC}\varepsilon_0}\frac{Z}{Y}}{1 - \frac{\alpha_e}{3\Omega_{UC}\varepsilon_0}}\right)(U_1 - U_2) \tag{2.17}$$

Two distinct situations can be differentiated from Eq. 2.17 according to the relation between U_1 - U_2 (nuclear motions connected to the soft mode) and V_2 - U_2 (distance of the electron shell to the anion core). These two situations are the so-called *low polarizability* and *high polarizability* cases.

The low and high polarizability cases are discussed now, taking into account that, since the system is modelled with the condition $K_{ion} \ll k_{el}$, necessarily: $\frac{K_{ion}}{k_{el}+K_{ion}} \ll 1$.

Low Polarizability Case:

The low polarizability case (per unit volume) corresponds to the situation where $\frac{\alpha_e}{3\Omega_{UC}\varepsilon_0} \to 0$ by which the Equation **??** can be approximated by:

$$(V_2 - U_2) \approx (U_1 - U_2)\left(\frac{K_{ion}}{k_{el}+K_{ion}}\right) \tag{2.18}$$

and, henceforth, given that $\frac{K_{ion}}{k_{el}+K_{ion}} \ll 1$, the following affirmation withholds:

$$(V_2 - U_2) \ll (U_1 - U_2)$$

This means that in the low polarizability case, the electronic charge displacement contribution to an electronic dipole is negligible in comparison to the contribution of the anion-cation displacements from the equilibrium position.

High Polarizability Case: Polarization Catastrophe

Much more interesting for this work is the high polarizability case, which explains the *Polarization Catastrophe* phenomenon. It is characterized by the fact that, when the temperature tends to the Curie temperature, $T \to T_C$, the electronic charge relocates over large distances in comparison to the displacements of the nuclei, the dielectric constant diverges, and the frequency of the transverse optical phonon tends to zero (Fig. 2.5).

To model the static dielectric constant in the context of the Cochran's theory of lattice dynamics, the Lyddane-Sachs-Teller relation ([57]) is applied, and by making use of the results obtained in Sec-

tion 2.2.3, it can be seen that the lattice vibrations induce a linear dependence of the force constants with the temperature, giving the relation:

$$\mu\,\omega_{TO}^2 = \tilde{K}_{ion}\,\gamma\,(T - T_C) \tag{2.19}$$

where γ is a temperature factor that is in the same order of magnitude of the coefficient of volumetric expansion. Therefore, when T $\rightarrow$ T_C, the frequency of the soft mode tends to zero, i.e., the mode "softens". This is consistent with the fact that, as commented before, the condition for lattice stability requires that the frequencies of its normal modes are strictly positive.

Now, by making use of the Curie-Weiss law:

$$\varepsilon_{st} = \varepsilon_\infty + \frac{C}{T - T_C} \tag{2.20}$$

with:

$$C = \frac{(\varepsilon_\infty + 2)^2\,(\tilde{Z}\,e)^2}{9\,\gamma\varepsilon_0\,\tilde{K}_{ion}} \tag{2.21}$$

it can be seen that, when T $\rightarrow$ T_C, the short range forces described by $\tilde{K}_{ion}$ lead to a rapidly growing dielectric function, and in the limit

$$\tilde{K}_{ion} \rightarrow \frac{(\varepsilon_\infty + 2)\,(\tilde{Z}\,e)^2}{9\,\varepsilon_0\,\Omega_{UC}}$$

the dielectric function diverges.

Also, from the previous results and the Clasius-Mossotti equation (Eq. 2.11), it can be seen that, when T $\rightarrow$ T_C, the denominator in Equation 2.13 tends to 0:

$$1 - \frac{\alpha_e}{3\Omega_{UC}\varepsilon_0} \rightarrow 0$$

with which:

$$(U_1 - U_2) \ll (V_2 - U_2) \tag{2.22}$$

The behavior in this situation is, henceforth, completely reversed with respect to the low polarizability case: electronic motions contribute highly to the polarization in the material, while the contribution from the anion-cation displacements is negligible. This behavior is fully in accordance with the archetypical characteristics of soft modes ([29]).

This pattern can be appreciated in the representation of the soft mode frequency (Fig. 2.5(a)) and the dielectric constant (Fig. 2.5(b)) against the temperature of the system. In this model, when the temperature finally reaches the critical temperature ($T = T_C$), the crystal is characterized by weak restoring forces whereas the long range interaction becomes predominant, fact which could ultimately lead to a ferroelectric phase transition.

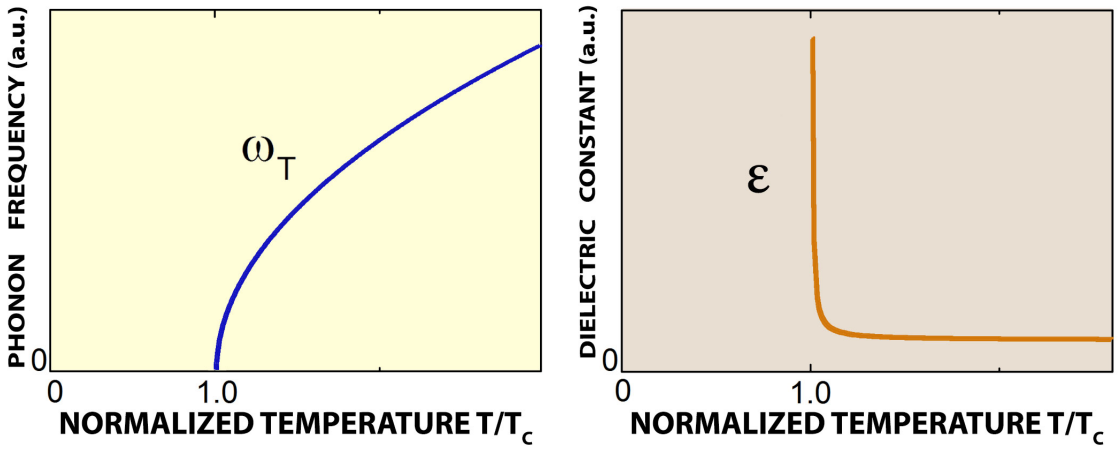

(a) (b)

Figure 2.5: The calculated curves shown here describe the so-called *polarization catastrophe*. It consists of the phenomenon that takes place when the temperature tends to the critical temperature, $T \rightarrow T_C$, by which the soft mode phonon *freezes* (i.e., its frequency becomes zero) and the spontaneous polarization and the dielectric constant diverge. Sub-Fig.2.5(a): Behavior of the transverse optical soft mode frequency as a function of the temperature near the critical temperature, T_C. Sub-Fig.2.5(b): Behavior of the dielectric constant as a function of the temperature near the critical temperature, T_C.

Modern Theory of Polarization

The development of the *Modern Theory of Polarization* in the 1990s is directly related to the study of ferroelectric materials. Even if the macroscopic polarization plays a pre-eminent role in the phenomenological theories, its derivation from microscopic fundamental magnitudes such as the dipole moment,

charge density, or microscopic current, had remained unresolved. In those days, a connection between macroscopic polarization and quantum electrodynamics was still required.

Extensive research has proven that simplistic theories relating the stationary microscopic charge densities to the macroscopic polarizations are ill-defined and lead to ambiguous results, being the only exception the Clausius-Mossoti case where the charge is strongly bound to its ionic sites ([10, 11, 14]).

Until the Modern Theory of Polarization was introduced, the macroscopic polarization could only be calculated from the classical electromagnetic definition whenever the conditions for the Clausius-Mossotti model were fulfilled, i.e., whenever the electronic charge is strongly bound to its ionic units ([48, 49]).

Whereas out of the Clausius-Mossotti conditions, inconsistencies in the concept of polarization quickly appeared ([78]). For example, for a number of materials under certain excitation conditions, there exists charge transfer between different ions in the crystal with which the classical definition for polarization is not applicable. Other inconsistency comes directly out of the definition of the crystal lattice: since the choosing of unit cell is not unique, different polarizations are possible depending on the adopted unit cell.

These and other problems caused commotion in the field, posing fundamental questions as to whether it was even possible to consider the polarization and other dependent magnitudes (e.g., the piezoelectric tensor) as intrinsic properties of an infinite crystal or whether these magnitudes are in fact determined by the particularities of the surface.

The solution came in the beginning of the decade of 1990s, when Resta, King-Smith and Vanderbilt concluded that the classical macroscopic polarization is, essentially, ill-defined and cannot be unambiguously described from the dipoles in the lattice. They concluded that there exists a more fundamental magnitude, i.e., the *variation of polarization* ($\Delta\mathbf{P}$) that a material experiences as a consequence of a transient process as can be the application of an external field. Following this reasoning, only the difference of polarization between two stationary crystal states is a well–defined observabe, that can be linked to measurable observables in an experiment ([79]). In this sense, the variation of polarization can be quantified either as finite differences of polarization (which is the methodology used to describe spontaneous polarization in ferroelectricity), or as derivatives of the polarization (methodology used to explain the susceptibility, the permittivity, the pyroelectric coefficients, the piezoelectric tensor, or the dimensionless Born effective charges).

In their pioneering work, Resta and other authors also presented a quantum mechanical concept, the so-called *geometric or Berry's phase approach*, with which the $\Delta\mathbf{P}$ between different stationary states, can be calculated from differential microscopic charge densities cast as quantum currents. More precisely, the variation of macroscopic polarization can be derived from the Berry's phase variation along a quantum path between two different quantum states whenever the process is cuasi-adiabatic ([9, 11, 13, 80]). The final state of that quantum-mechanical motion can be determined without the necessity to know the spatio-temporal phase of the electronic wave function along the adiabatic path by means of the Stokes' theorem ([15, 16]). It bears mentioning that the Berry's phase approach has

been utilized in this context as a tool to study the variation of polarization, but it is based in highly sophisticated quantum concepts going deep into the mathematics of the Schrödinger equation whose theoretic details are beyond the scope of this work.

As a significant example, it can be mentioned that, Resta in 1992 made use of this methodology to solve the spontaneous polarization of perovskite $KNbO_3$ in a Berry's phase approach using the Bloch functions of its tetragonal structure from where he obtained a calculated value for macroscopic polarization of $P_S = 35\mu C/cm^2$, rather close to the measured value $P_S \approx 35\mu C/cm^2$ ([12]) .

Notwithstanding, the Berry phase approach still presents the crucial limitation that it cannot derive instantaneous microscopic currents from the transient electronic charge density, given the fact that once assumed the adiabatic character of the electronic charge motion in space, the expected value for the current density operator vanishes at all times $<\mathbf{j}(\mathbf{r},t)> = 0$ ([81, 82]) with which in this approximation there is no transient electronic transfer. This issue is related to the fact that the adiabatic electronic translation is, in fact, an idealized process in which the electrons move infinitesimally slow. In reality, however, to be able to displace charge, the electrons need to be accelerated and de-accelerated, which is incompatible with an adiabatic process. This treatment is only valid to calculate the differences of polarization of stationary macroscopic states ([16]), and cannot assess the dynamics of transient macroscopic polarization differences induced by real time-dependent microscopic currents.

A number of succesful experiments in the recent years have validated ultrafast X-Ray powder diffraction as a methodology to derive spatially and time-resolved charge density maps, and study the charge dynamics in polar materials ([7, 24, 26, 29, 83, 84]) . However, according to the ideas exposed previously, the modern theory of polarization cannot be applied to determine the variation of polarization from those transient charge density maps. Recently, an extension of the original theoretical framework has been accomplished, that finally connects the transient variations of macroscopic polarization with the charge dynamics at the microscopic level.

The central idea of this enhanced approach is that the derivation of the microscopic current density, $\mathbf{j}(\mathbf{r},t)$, has to comply with two constraints: the electronic motion must be subjected to the continuity equation and, at the same time, the kinetic energy of the electrons must be minimized during their motion at all times ([16]). These theoretical enhancement finally allows for the determination of the variation of polarization from the transient charge density maps in a general dynamical case, and not just in the Clausius-Mossotti case.

Nonetheless, the derivation of the variation of polarization for the particular case of photoexcited ferroelectric ammonium sulphate studied in this work, can be simplified due to its particular structure, as shall be explained in detail in Section 5.5.

2.3 Properties of Ammonium Sulphate

The most relevant properties of ammonium sulphate, $(NH_4)_2SO_4$, along with its crystallographic structure and symmetries are discussed in this section.

Ammonium sulphate is an inorganic salt of wide commercial and industrial relevance, being most commonly used as a soil fertilizer ([85, 86]). It is a hydrogen-bonded material composed by the polyatomic ammonium cation (NH_4^+) and sulphate anion (SO_4^{2-}). Ammonium sulphate is the main representative of a family of crystals (other typical examples can be $(NH_4)_2BeF_4$ or K_2SO_4, [87]), that are characterized with particular dielectric qualities such as a small Curie-Weiss constant, weak temperature dependence of the dielectric constant (except for temperatures close to the phase transition temperature), relatively small spontaneous polarization, high spontaneous strain, high transition entropy, and strong anomalies in birefringence ([35, 88, 89]).

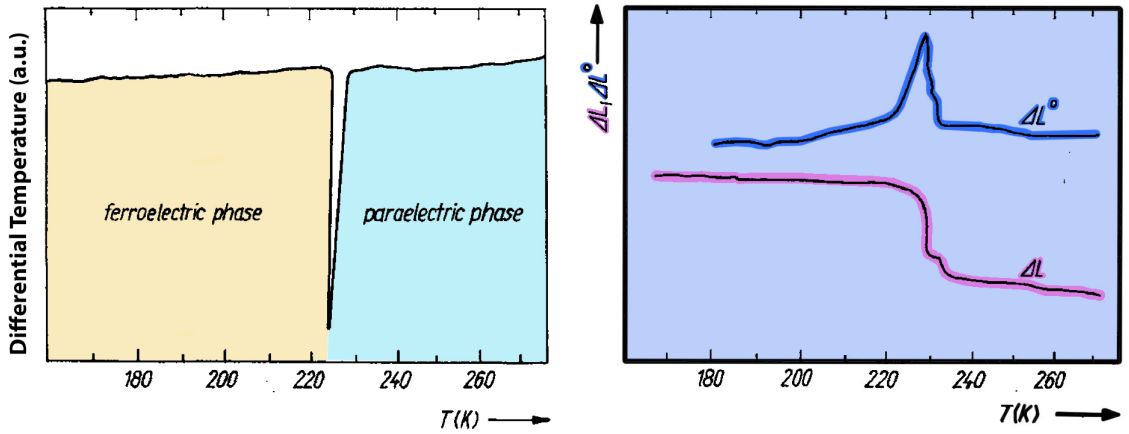

(a) (b)

Figure 2.6: The change of volume in a para- to ferroelectric transition for ammonium sulphate has been measured using different techniques. Sub-Fig. 2.6(a): DTA thermogram for $(NH_4)_2SO_4$, the curve shows that an endothermic phase transition takes place at 223K during cooling. The sudden and sharp variations in the temperature suggest a first-order type of transition as confirmed by the measurements in [35]. Sub-Fig. 2.6(b): Dilatometric measurement for $(NH_4)_2SO_4$ during its phase transition. A large increase in ΔL at about 223K was detected, where its derivative, ΔL^0, shows a peak. The Differential Thermal Analysis (DTA) and the dilatometric measurements presented here are taken from Ref.[104].

Ammonium sulphate has been extensively studied by several physical methods such as Nuclear Magnetic Resonance (NMR, [90–92]), Electronic Paramagnetic Resonance (EPR, [93–96]), Raman and infrared studies ([64, 72, 97–101]), Thermomechanical Analysis (TMA, [92, 102, 103]), Differential Thermal Analysis (DTA) and dilatometric measurements ([104], Fig. 2.6), inelastic incoherent neutron scattering ([102, 105–111]), far infrared transmission and reflectivity measurements ([112]), X-Ray, electron and neutron diffraction ([102, 104, 113, 114]), along with various other studies on its specific heat ([69]), elastic anomalies ([115]), thermal expansion ([35, 69, 116]), and dielectric function ([5, 117, 118]).

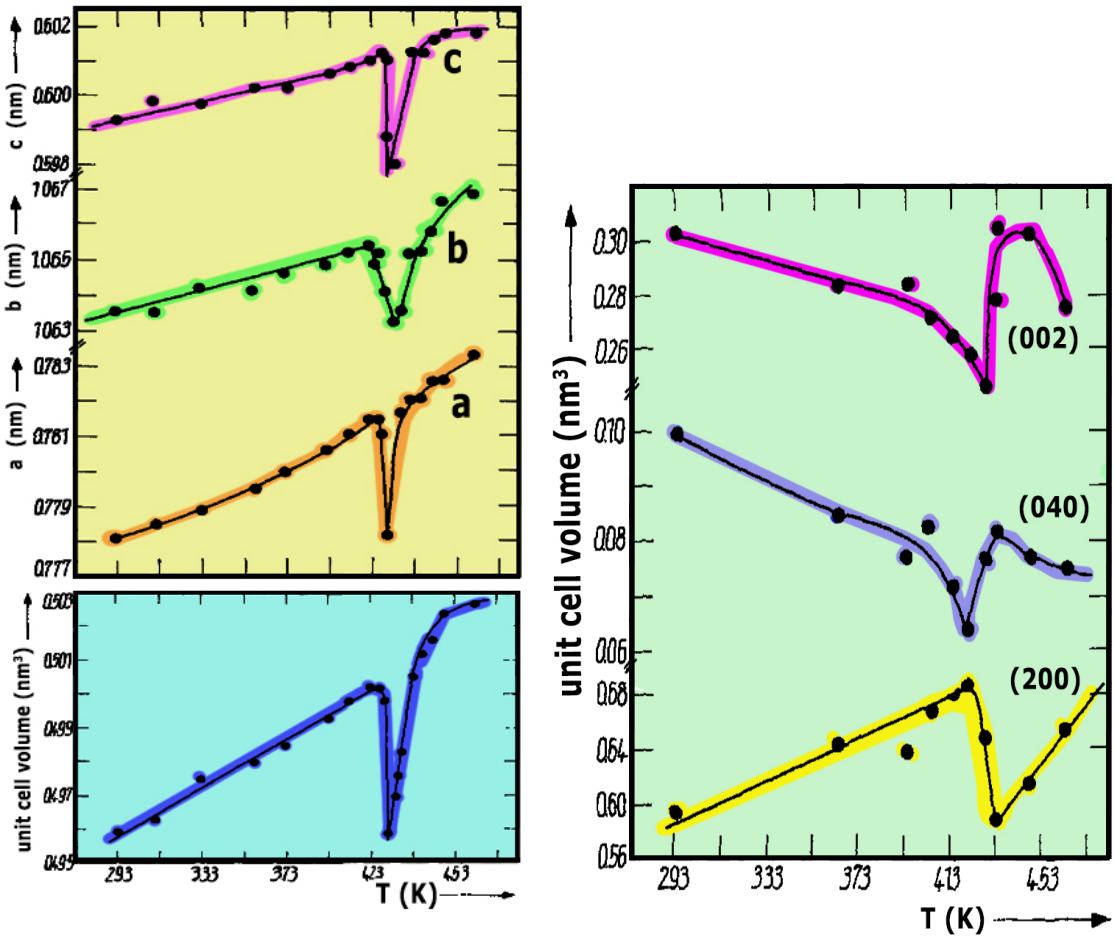

(a) (b)

Figure 2.7: Variation of lattice constants, unit cell volume and relative diffracted intensity for selected Bragg peaks in Ammonium Sulphate (Modified from Ref. [114]). **Sub-Fig. (a)**: Temperature dependence of the AS lattice constants a, b, and c (upper panel), and Volume vs. Temperature for the AS unit cell (lower panel). **Sub-Fig. (b)**: Temperature dependence of Bragg diffractions for the (200), (040), and (002) planes of $(NH_4)_2SO_4$ crystals.

Ammonium sulphate presents a para- to ferroelectric phase transition which is known since Matthias and Remeika discovered it in 1956 ([119]). Below the critical temperature, $T_C = 223K$, it adopts a ferroelectric phase and above a paraelectric phase. The change of volume in a para- to ferroelectric transition for ammonium sulphate has been measured using different techniques, as the DTA thermogram and dilatometric measurements (Fig. 2.6). Specifically, the variation of length and volume of the unit cell for ammonium sulphate in the para- to ferroelectric phase transition shall be discussed later in this work as it helps identifying the precise instant of the change of phase as a sample of ammonium sulphate is cryogenically cooled down (Fig. 4.11(a) and Fig. 4.11(b)).

Apart from the already mentioned para- and ferroelectric phases, ammonium sulphate presents yet another phase, that occurs above $T_C = 423K$, although in that case the crystal structure remains the same even if the unit cell changes its volume (Fig. 2.7, [114]).

2.3.1 Crystallographic Structure of Ammonium Sulphate and Symmetries

This work is focused on the photoexcited ferroelectric phase in the vicinity of the para- to ferroelectric transition temperature. In the ferroelectric phase, ammonium sulphate crystallizes in an orthorhombic lattice structure (Space Group $Pna2_1$) with four formula units per unit cell, and presents two crystallographically independent ammonium ions, NH_4^+(I) and NH_4^+(II), which are surrounded with six neighbouring SO_4^{2-} anions. A three-dimensional perspective depiction of the unit cell, and its projections on the **a-b** and **b-c** planes are presented in Fig. 2.8 and Fig. 2.9.

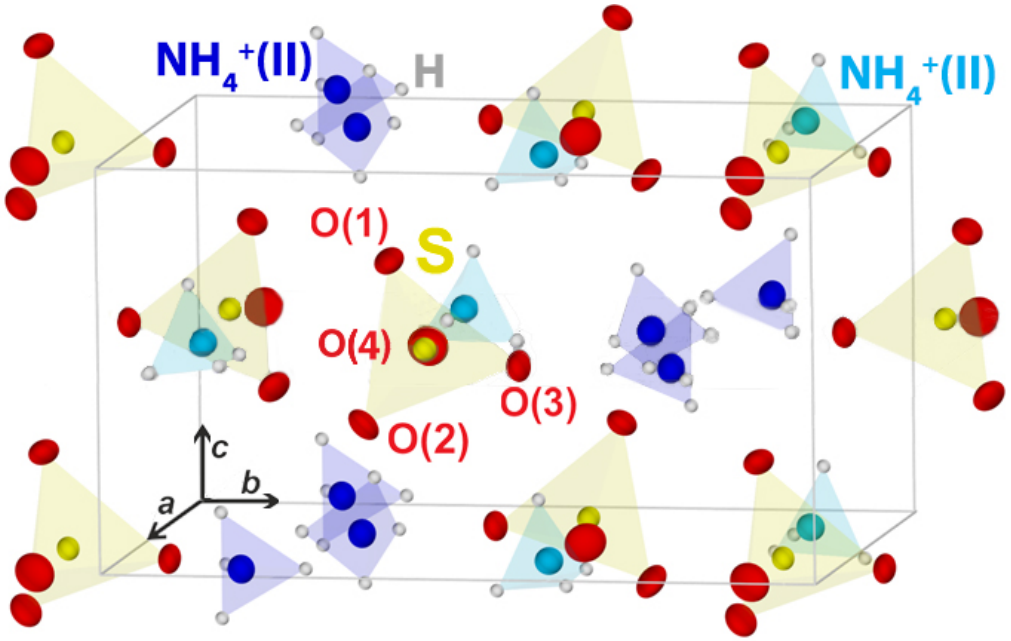

Figure 2.8: Equilibrium crystal structure of ferroelectric ammonium sulphate in an ORTEP representation (50% probability ellipsoids). The dimensions of the ferroelectric ammonium sulphate unit cell are a = 0.78566(3)nm, b = 1.05813(4)nm, and c = 0.59530(2)nm.

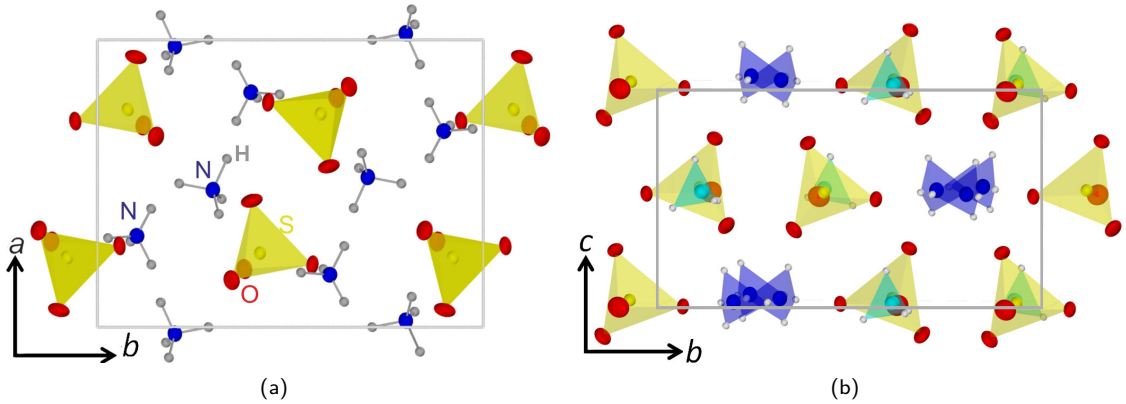

(a) (b)

Figure 2.9: Projections of the ferroelectric Ammonium Sulphate unit cell on the **a-b** (Fig. 2.9(a)) and **b-c** planes (Fig. 2.9(b)).

The details of the projection of one formula unit (out of the four formula units contained in each elementary cell) of the para- and ferroelectric ammonium sulphate onto the b-c plane are shown in Fig.2.10 ([69]). It is the tilting of the NH_4^+(II) and SO_4^{-2} ions with respect to the c-axis what produces a permanent net electric dipole moment in the ferrolectric ammonium sulphate (space group $Pna2_1$) which does not appear in its paraelectric phase (space group Pnam).

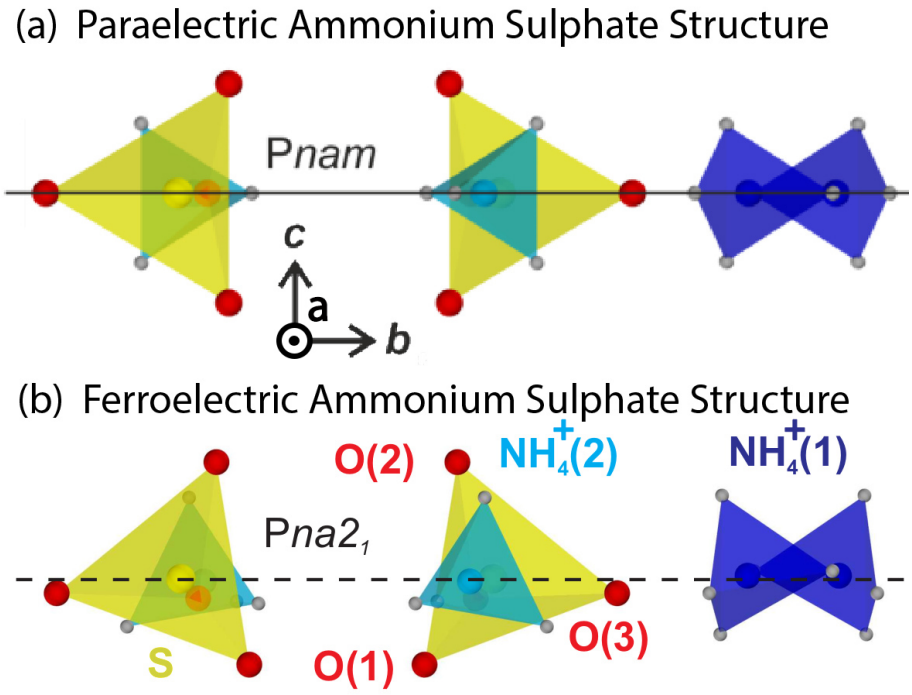

Figure 2.10: This figure shows the projection of one formula unit of the para- and ferroelectric ammonium sulphate onto the b-c plane of the unit cell. In the sub-figure above, can be seen the structure of the paraelectric phase (space group Pnam), and in the sub-figure below, the structure of the ferroelectric phase (space group $Pna2_1$). The most remarkable feature is the detail of the different orientation of the NH_4^+(II) and SO_4^{2-} ions along the c-axis in the para- and ferroelectric ammonium sulphate. The position of the atoms are indicated by coloured spheres, i.e., red is oxygen, grey is hydrogen, yellow is sulphur, and light blue and dark blue are the crystallographically non-equivalent nitrogens).

2.3.2 Ammonium Sulphate Symmetries

Some important physical properties are directly dependent upon the crystal *point group symmetry* (or *crystal class*), e.g., electrostriction, pyroelectricity, piezoelectricity or ferroelectricity [2]. The symmetries for para- and ferroelectric ammonium sulphate are well known ([120–123]), and here only the relevant properties for ammonium sulphate that depend on the crystal class are briefly mentioned.

[2] **Piezoelectricity**: property of materials where there exists a coupling between electrical and mechanical energies; e.g. an applied stress will result in a polarization. **Pyroelectricity**: property of materials, necessarily with an unique polar axis, where the polarization depends on the temperature (due to structural changes that arise from thermal effects). **Electrostriction**: property of dielectrics by which their shape changes under the application of an external electric field.

In this sense, paraelectric ammonium sulphate which is characterized by the space group Pnam, is a centrosymmetric crystal class and, henceforth, it must be electrostrictive, and it is excluded from the possibility of being piezoelectric, ferroelectric, pyroelectric and cannot be optically active. Ferroelectric ammonium sulphate, on the contrary, is characterized by having the space group $Pna2_1$ which is non-centrosymmetric and, therefore, it is piezoelectric, pyroelectric with a polar axis along the c-direction, and optically active.

2.3.3 Dielectric Properties of Ammonium Sulphate

As previously discussed in this chapter, the transition of para- to ferroelectric materials usually leads to strong anomalies in the dielectric constant, and the elastic and thermal properties of the material.

Ammonium sulphate fulfils this condition and presents pronounced changes of the dielectric function ([117], Fig. 2.12), spontaneous polarization ([35], Fig. 2.11), and heat capacity ([69], Fig. 2.13).

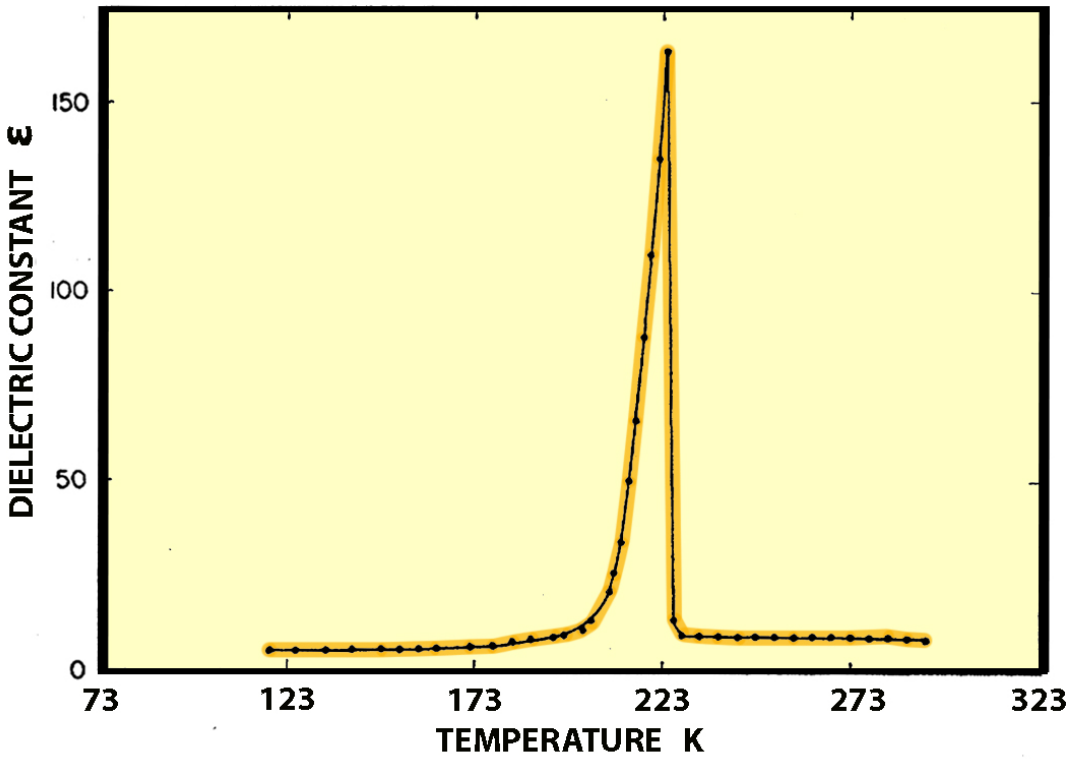

Figure 2.11: Ammonium Sulphate $(NH_4)_2SO_4$: Dielectric constant vs. temperature in the vicinity of the critical point ([35]).

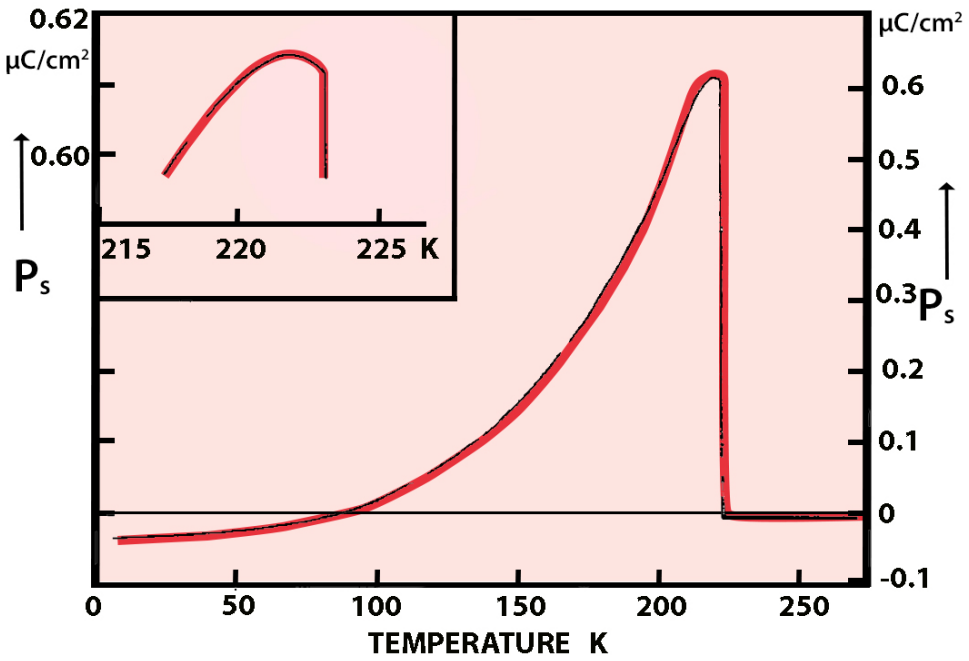

Figure 2.12: Ammonium Sulphate $(NH_4)_2SO_4$: Spontaneous polarization vs. temperature in the vicinity of the critical point (from static pyroelectric measurements, [69]).

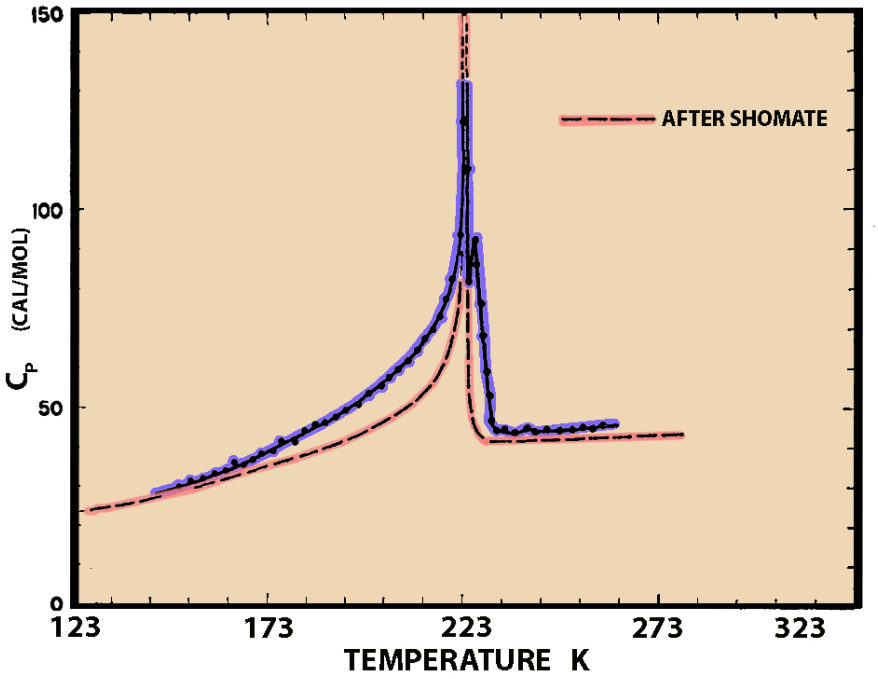

Figure 2.13: Ammonium Sulphate $(NH_4)_2SO_4$: Specific heat vs. temperature in the vicinity of the critical point. Thermal results portraying the typical lambda-type anomaly at the transition temperature are presented here ([35]). The continuous line corresponds to the work of Shomate ([124]), and the discontinuous corresponds to Nitta and Suenaga ([125]).

Chapter 3

Concepts of X-Ray Diffraction

X-Ray diffraction is discussed here in the context of Bragg's law and its equivalent Laue condition, along with the kinematical approximation for weakly X-Ray scattering powder material. Subsequently, the reconstruction of time-resolved electronic charge densities from the transient variation of diffracted intensity in the different Bragg peaks is discussed.

3.1 Powder Diffraction

The interaction of the X-Ray probe with photoexcited powder ammonium sulphate generates the so-called Debye-Scherrer diffraction rings (panel (a) in Fig. 3.1), which are subsequently recorded by the large-area Dectris 1M Pilatus camera. The integration of the intensity over each Debye-Scherrer ring provides the diffracted intensities as a function of the scattering angle 2θ (panel (b) in the Figure 3.1). As can be seen in the figure, the 15 Bragg peaks that can be measured due to geometrical limitations in the experimental set-up are easily identified with the help of Bragg's Law (as fully described in Section 3.2).

An important feature of the X-Ray powder experiments is that some of the Bragg peaks may appear partially or totally overlapped. For example, the (120) and (111) Bragg peaks are overlapped in the Figure 3.1 (panel b). At the wavelength of the characteristic Cu-K_α X-Ray radiation ($\lambda = 0.154$nm) used in the experiment, the diffraction angles (2Θ), for the Bragg peaks (120) and (111) almost coincide, being only separated by the rather small difference $\Delta(2\Theta) = 0.278°$. Since this difference is smaller than the average full width at half maximum (FWHM) for a single Bragg peak ($\Delta(2\Theta) \approx 0.5°$) at the sample-to-detector distance, the conclusion is that these two Bragg peaks are indistinguishable and cannot be individually resolved. However, under certain conditions relevant information can still be extracted from groups of overlapping Bragg peaks with the help of the BayMEM software that implements the Maximum Entropy Method (MEM) and is used to derive the transient charge density. The precise method to minimise this problem is discussed in Section 4.6. If, even with the help of BayMEM, the overlapping feature is too pronounced, a single crystal will need to be used to resolve the single diffraction peaks by applying other X-Ray diffraction methodology, e.g., the rotating-crystal method ([126]).

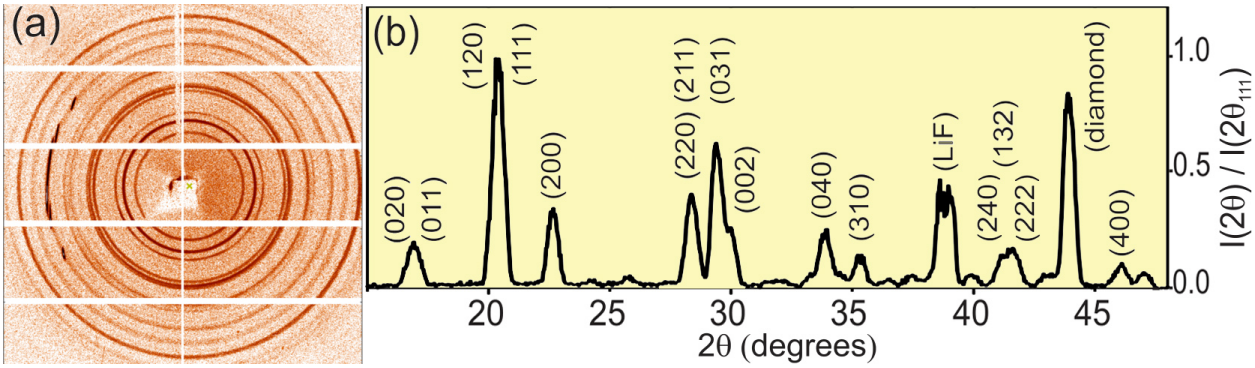

Figure 3.1: **Panel (a)** shows the Debye-Scherrer diffraction ring pattern accumulated for ammonium sulphate after 140 seconds of exposure. **Panel (b)** shows the integration of the diffracted intensity over each Debye-Scherrer ring as a function of the scattering angle 2θ (normalized with respect to the maximum intensity Bragg Peak). The ammonium sulphate powder sample is contained between two crystalline windows of lithium fluoride (LiF) and diamond that shall also generate Bragg peaks. The Bragg peaks associated to those windows is not be considered in the analyses.

3.2 Bragg's Law and Laue Condition

Bragg's law shall be discussed now since it plays an essential role in powder diffraction experiments, by allowing for the identification of the diffraction peaks. Nonetheless, even if essential to the field of X-Ray crystallography, Bragg's law does not permit to calculate the actual intensity of the diffracted peaks which is why the concept *structure factor* shall be introduced in the section dedicated to the *kinematical approximation* (Sec. 3.4). The structure factor allows for the determination of the diffracted intensity and for the reconstruction of the transient charge density maps with which to study the dynamics of the system (Sec. 3.5).

Bragg's law states that constructive interference occurs when the path difference, $2 \cdot d \cdot sin\Theta$, between two beams diffracted from neighboring lattice planes is equal to an integer multiple of the wavelenght of the incident beam, $n \cdot \lambda$ ([127]). As can be seen in the well-known scheme in Fig. 3.2(a), Bragg's law can be derived from a simple crystal model consisting of a set of planes separated by a distance d, where the wavelength (λ) of the incident radiation is known, and the incident angle corresponds to θ ([127]):

$$2 \cdot d \cdot sin\theta \quad = \quad n \cdot \lambda, \ \ where\, n \in \mathbb{N} \tag{3.1}$$

Notwithstanding, when many different sets of lattices are drawn together at the same time, the design rapidly becomes incomprehensible. This problem can be simplified if, instead of using the *direct or real lattice* vectors, each set of planes is characterized by a certain **vector d** whose direction is normal to the planes, and whose length coincides with the inverse plane spacing. Vector **d** is defined in the so-called *reciprocal space* which is generated by the *reciprocal basis*, ($\boldsymbol{b}_1^*$, $\boldsymbol{b}_2^*$, $\boldsymbol{b}_3^*$), ([128]).

The Laue condition ([129]), which is equivalent to Bragg's law, is presented here briefly by reason of being more convenient for the comprehension of X-Ray diffraction experiments. As explained in detail in Section 3.5.1, the Laue condition is crucial to calculate the structure factors that ultimately give the intensity of the different diffracted Bragg peaks (comprehensively visualized with the help of the so-called *Ewald Sphere*, as shown in Fig. 3.3(a) and Ref. [127]).

Since Bragg's Law and Laue condition are equivalent, the mathematical solution to Bragg's Law (Equation 3.1) will coincide with the solution of the Laue Condition:

$$\boldsymbol{Q} \quad = \quad \boldsymbol{G}_{hkl} \tag{3.2}$$

where $\mathbf{Q} = \mathbf{k}$ - $\mathbf{k}_0$ corresponds to the wavevector difference (or scattering vector) and $\mathbf{G}_{hkl} = \mathrm{h} \cdot \mathbf{b}_1^* + \mathrm{k} \cdot \mathbf{b}_2^* + \mathrm{l} \cdot \mathbf{b}_3^*$, defines a point in the reciprocal lattice.

Figure 3.2 shows how the Laue condition can be summarized in the idea that the scattered waves interfere constructively when the wave vector variation, **Q**, is equal to one of the points of the Reciprocal Lattice $\mathbf{G}_{hkl}$ ([130]). Given that Thomson elastic scattering governs the interaction of matter with hard Cu-K$_\alpha$ X-Ray photons ($E_{Cu-K_\alpha} = 8.048$ keV) in this type of experiment, as shall be fully discussed in Sec. 3.3, there is no loss of energy in the diffracted photon, and $|\mathbf{k}| = |\mathbf{k}_0| = 2 \cdot \pi/\lambda$.

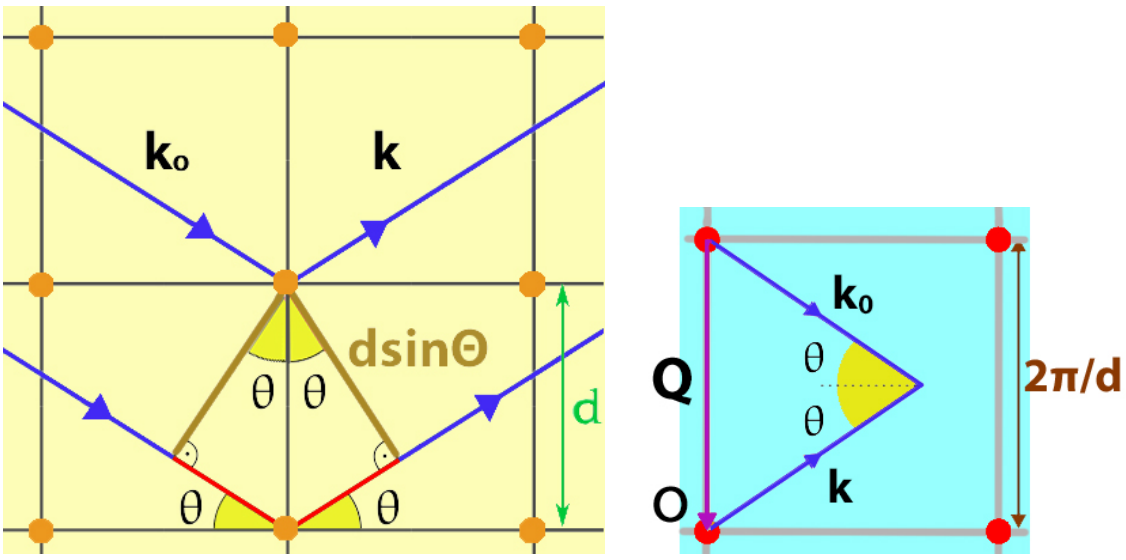

(a) (b)

Figure 3.2: While Bragg's law and the Laue condition are equivalent, the latter is more adequate to interpret X-Ray diffraction experiments ([129]). The examples given here are presented in a 2D-square lattice for simplicity, and the figure on the left corresponds to the direct lattice and on the right to the reciprocal lattice. Sub-Fig. 3.2(a): Classical schematic describing Bragg's law (Eq. 3.1), which states that constructive interference occurs when the path difference between two identical incident beams is equal to an integer multiple of their wavelength. Sub-Fig. 3.2(b): The Laue condition (Equation 3.2) ensures constructive interference wherever the scattering vector **Q** is equal to a reciprocal lattice vector $\mathbf{G}_{hk}$.

An effective way to envisage constructive interference in the reciprocal lattice is represented by the so-called Ewald Sphere (or Ewald circle in 2-Dimensions) shown in Fig. 3.3(a). If a sphere is drawn in the reciprocal space with radius $|k| = |k_0| = 2 \cdot \pi/\lambda$, the Laue condition is fulfilled wherever the sphere overlaps with any point of the reciprocal lattice.

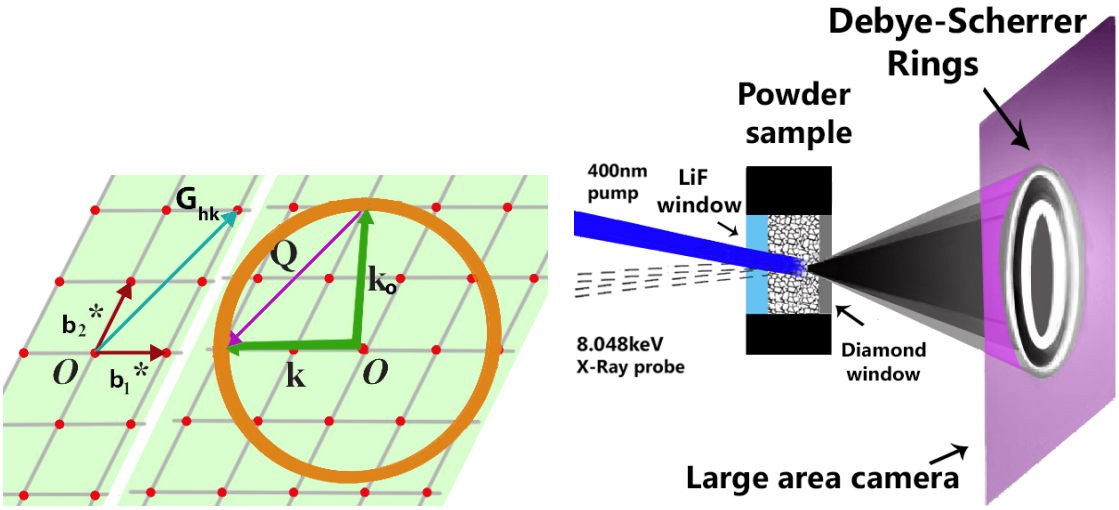

(a) (b)

Figure 3.3: The Ewald sphere and the generation of Debye-Scherrer rings are intimately related. Sub-Fig. 3.3(a): Depiction of the Ewald circle (simplified Ewald sphere in 2 dimensions). The Laue condition ensures constructive interference wherever the scattering vector $\mathbf{Q}$ is equal to a reciprocal lattice vector $\boldsymbol{G}_{hk}$. The radius of the Ewald sphere depends on the photon energy. Since Thomson scattering is elastic, there is no loss of energy in the diffracted photon, with which $|k| = |k_0| = 2 \cdot \pi/\lambda$. Sub-Fig. 3.3(b): schematic of the detail of the interaction of X-Ray with the powder sample. The powder sample corresponds to ferroelectric ammonium sulphate in a pellet of randomly oriented crystallites contained between lithium fluoride and diamond windows (the details of the preparation of the sample are fully explained in Section 4.2). The X-Ray photons emerge from the sample as diffraction cones that give rise to a ring-like pattern called Debye Scherrer rings.

In powder diffraction experiments the crystallites, which individually allow for the single scattering phenomenon, are compacted together in random orientation. The rotation of the crystallites is associated to an analogous rotation around the origin of the reciprocal space which causes that, in particular cases, different points of the reciprocal lattice lie on the Ewald sphere. In this situation, a constructive interference coming from the powder sample in the form of cones is expected for certain 2Θ diffraction angles ([131, 132]). These cones are called Debye-Scherrer cones, whereas the intersection of the cones with a plane produce the Debye-Scherrer rings. Fig. 3.3(b) shows schematically the Debye-Scherrer cones generated by the interaction of X-Ray with the powder sample, and Fig. 4.6 shows the Debye-Scherrer rings as recorded by the plane surface of the large area camera.

3.3 X-Ray Interaction with Condensed Matter

The interaction of electromagnetic radiation with matter depends on different mechanisms of absorption and scattering by the atoms compounding the material.

The most important absorption and scattering phenomena are the Thomson scattering ([133, 134]), Compton scattering ([135–137]), Auger effect ([138–140]), photoelectric absorption ([141–143]), pair production ([144]), and Rayleigh scattering ([145, 146]). This work shall only focus on the effects of Thomson scattering given the fact that it is the phenomenon at the basis of X-Ray crystallography, and all the other effects are negligible under the experimental set-up conditions.

Thomson Scattering

Since Thomson scattering is the most pre-eminent phenomenon explaining X-Ray diffraction, some of its most important characteristics are given here. Thomson scattering is explained by classical electrodynamics as the elastic scattering of electromagnetic radiation by a free or weakly bound non-relativistic charged particle. It is relevant in the low-energy limit of the Compton scattering, i.e., whenever the energy of the incoming photon is much smaller than the rest mass energy of the scattering particle or, equivalently, if the Compton wavelength of the scattering particle, $\lambda_C = h/mc$, is much smaller than the wavelength of the incoming photon. This condition is fulfilled by electrons in condensed matter that scatter impinging X-Ray Cu-K_α photons:

$$E_{Cu-K_\alpha} = h\nu_{Cu-K_\alpha} = 8.048\,keV \ll E_{Rest\,Mass} = m_e c^2 = 0.511 MeV$$

or

$$\lambda_c^e = h/m_e c = 2.426 pm \ll \lambda_{Cu-K_\alpha}^{X-Ray} = 0.154 nm$$

.

The semi-classical description of Thomson scattering explains that a charged particle under the effect of incoming electromagnetic radiation is accelerated primarily by its electric field component, while the effect of its magnetic field is negligible. Subsequently, the accelerated charged particle, in turn, shall emit dipole radiation. Since the Thomson scattering is an elastic phenomenon, i.e., there is no energy transfer, the kinetic energy of the charged particle and the energy of the incoming photon remain unaltered by the interaction ([133]), the wavelengths of the scattered photon and charged particle do not vary, and the coherence of the outcoming electromagnetic radiation is retained ([134]).

In condensed matter, it is the accelerated electrons that make the strongest contribution to the scattering of X-Rays since the nuclei, having a much larger mass than electrons, suffer a much smaller

acceleration which renders the radiation they scatter negligible in comparison ([129, 147, 148]). Given this fact, this thesis will only consider the Thomson scattering of X-Ray radiation by electrons.

3.4 Kinematical X-Ray Diffraction Theory

The *kinematical diffraction theory* consists of an approximation method to model the diffraction of X-Ray radiation by a crystal in the limit of weak scattering. It is based on neglecting all multiple scattering events and describes properly the scattering from thin crystals or powder-samples composed of small crystallites compacted together in a thin film. To develop the kinematical theory, it is convenient to divide the system into structures on short length scales, i.e., atoms or molecules, and long-range crystalline order.

When multiple scattering effects cannot be neglected, e.g., the case of large perfect crystals, the subject is more complex and the kinematical theory is no longer valid. This multiple scattering phenomenon is addressed by the more complicated *dynamical scattering theory* ([129, 131]).

3.5 Reconstruction of charge density maps

In this section, building on what has been learned until now about the Thomson scattering and the interaction of X-Ray radiation with a single electron, the intensity of the diffraction by a crystal in the weak scattering limit and the reconstruction of the electron density shall be addressed.

The Miller indices for the different Bragg peaks diffracted by a crystalline sample are easily identifiable with the help of Bragg's law. However, to reconstruct the transient charge density maps, the intensity of the different Bragg peaks needs to be characterized. The concepts *atomic factor* and *structure factor* are key in this sense, and will be introduced in the following.

3.5.1 The Structure Factor

Once the Thomson scattering of X-Rays by a single electron has been discussed, the next logical step consists in describing the scattering by a single atom. The *atomic form factor* or *complete atomic scattering*, f($\mathbf{Q}$), is generally defined as a measure of the scattering amplitude of an incident wave by an isolated atom. In the non-general case studied here, where only electrons can interact with the incoming monochromatic Copper-K$_\alpha$ X-Ray radiation ($\lambda_{Cu-K_\alpha}^{X-Ray} = 0.154$nm) and no resonance (absorption) phenomena is considered, the atomic form factor is defined as the superposition of the Thomson scattered X-Ray radiation by the weakly-bound electrons distributed in the different layers

surrounding the nucleus. If the electrons of the atom are understood as a distribution of continuous electronic charge, the *complete atomic scattering* or *atomic form factor*, f($\mathbf{Q}$), is defined as the integral of the product of the charge density, $\rho(\boldsymbol{r})$, with the phase factor, e $^{i\boldsymbol{Qr}}$, i.e., the Fourier transform of the electronic charge density ([129]):

$$f(\boldsymbol{Q}) = \int_{\Omega_{Atom}} \rho(\boldsymbol{r}) \cdot e^{i\boldsymbol{Qr}} \cdot d\boldsymbol{r} \tag{3.3}$$

where $\rho(\boldsymbol{r})$ is the electronic charge density, and the infinitesimal scattering volume, d$\mathbf{r}$, provides the contribution $\rho(\boldsymbol{r}) \cdot e^{i\boldsymbol{Qr}} \cdot d\boldsymbol{r}$.

It is worth noting that the scattering amplitude increases with the atomic number, Z, although X-Ray Thomson scattering is not very effective with light atoms and, in general, very little difference can be appreciated between adjacent elements in the periodic table as can be hydrogen and helium.

The Structure Factor for a Crystal

In the field of X-Ray crystallography, the structure factor, F_{hkl}, is the mathematical expression that describes how a crystal scatters the incident radiation. It is crucially important for the work presented here, because it is the magnitude that can be indirectly accessed in the experiment by measuring the transient variation of diffracted intensity (Sec. 3.6), and it is from their interpretation that the transient charge dynamics in the photoexcited crystal are revealed. In the case considered here, where the incident X-Ray beam is monochromatic and no resonance phenomena are considered, it consists of the superposition of the X-Ray scattered radiation by the electronic charge throughout the unit cell.

With the approximation that the unit cell is considered as a distribution of single-atoms where all the electronic charge is exclusively located at the centre of the atomic sites, the structure factor can be calculated as the sum over their atomic scattering factors:

$$F^{UnitCell}(\boldsymbol{Q}) = \sum_{j-ATOM}^{Unit\ Cell} f_j(\boldsymbol{Q}) \cdot e^{-i\cdot\boldsymbol{Q}\cdot\boldsymbol{r}_j} \tag{3.4}$$

where $f_j(\boldsymbol{Q})$ is the atomic factor of each individual *j-atom* within the unit cell.

In the case where there exist constructive interference, the Laue condition is fulfilled ($\boldsymbol{Q} = \boldsymbol{q}_{hkl}$) and the structure factors are given by:

$$F_{hkl} = \sum_{j-ATOM}^{UNIT\ CELL} f_j(\boldsymbol{q}_{hkl}) \cdot e^{-i\cdot\boldsymbol{q}_{hkl}\cdot\boldsymbol{r_j}} = \sum_{j-ATOM}^{UNIT\ CELL} f_j(\boldsymbol{q}_{hkl}) \cdot e^{-2\pi i(hx_i+ky_i+lz_i)} \tag{3.5}$$

In general, structure factors are complex quantities with amplitude and phase, and only become real in the particular case of crystals that have inversion symmetry (with phase either 0 or π). A consequence of this definition is that for certain Bravais lattices, i.e., those that only have one kind of element or that have different atoms with equal atomic factor, the overlapping of scattered waves can produce constructive or destructive interference for certain Miller indices. In this case, selection rules that indicate whether a Bragg peak is allowed or forbidden for a certain set of Miller indices can be deducted ([131]).

When the unit cell is understood, not as a distribution of atoms where all the electronic charge is located at the centre of the atomic positions, but as a continuous distribution throughout the volume of the unit cell, the structure factor is defined as the *Fourier transform* of the electron density, $\rho(x,y,z)$ ([131, 149]):

$$F_{hkl} = \frac{1}{\Omega_{UC}} \int \rho(x,y,z) e^{-2\pi i(hx+ky+lz)} d\boldsymbol{r} \tag{3.6}$$

And vice versa, the transient electron density, $\rho(x,y,z)$, can be calculated by applying the *inverse Fourier transform* to the structure factors F_{hkl} ([150]) as:

$$\rho(x,y,z) = \frac{1}{\Omega_{UC}} \sum_{hkl} F_{hkl} e^{2\pi i(hx+ky+lz)} \tag{3.7}$$

whereby intensity of a certain Bragg reflection depends on the Structure Factor like:

$$I_{hkl} \propto |F_{hkl}|^2$$

3.6 Time-resolved X-Ray Diffraction

From the previous results, it can be deduced that the transient variation of diffracted intensity, $\Delta I_{hkl}(t)$, is related to the transient and static X-Ray structure factors according to the expression:

$$\frac{\Delta I_{Ihkl}(t)}{I^0_{hkl}} = \frac{|F_{hkl}(t)|^2 - |F^0_{hkl}|^2}{|F^0_{hkl}|^2} \tag{3.8}$$

where $\Delta I_{Ihkl}(t)$ is the variation of intensity for the diffracted Bragg peak of Miller index (hkl) with respect to the unexcited diffraction intensity, I^0_{hkl}, and $F^0_{hkl} = F_{hkl}(t = 0)$ and $F_{hkl}(t)$ correspond to the static and transient structure factor, respectively.

One of the key issues here is the so-called *phase problem*. The structure factors are complex quantities, henceforth, characterized by an amplitude and a phase, i.e., $F_{hkl} = |F_{hkl}|e^{\phi_{hkl}}$. Since the measured magnitude in the experiment is the intensity I_{hkl}, only the $|F_{hkl}|$ can be derived, whereas the phase ϕ_{hkl} is unknown. Under certain conditions, it is possible to recover the lost phases and different methods have been developed with this purpose. There exist *direct inversion methods*, that are possible in centrosymmetric cases where the phase can only be 0 or π, or the more complex indirect methods, that are appropriate when the lattice lacks inversion symmetry. The transient electronic charge density of KDP (KH_2PO_4) can be cited as an example where the indirect method was used ([29]).

There is still another question to be considered regarding the derivation of the structure factors from the transient variation of diffracted intensity. In accordance with the Equation 3.8, if the phasing problem could be hypothetically solved, then, the exact transient electronic charge density distribution could be extracted with the help of the Fourier transform by measuring the variations of diffracted intensity in all of the Bragg peaks, $\Delta I_{Ihkl}(t)/I^0_{hkl}$, combined with the previous knowledge of the static structure factors, F^0_{hkl} ([150, 151]):

$$\rho(\mathbf{r},t) = \frac{1}{\Omega_{UC}} \sum_{hkl} F_{hkl}(t) e^{2\pi i(hx+ky+lz)} \tag{3.9}$$

This is an impossibility in practice because, due to the intrinsic geometry of the experimental set-up, only a limited set of diffraction peaks, i.e., only a limited number of structure factors, is accessible (Eq. 3.9). Under this circumstances, the use of the inverse Fourier transform to reconstruct the transient charge density will produce *series truncation errors*. To avoid this problem, the electron density in this work is reconstructed in an iterative fashion by a recursive formalism called Maximum Entropy Method (MEM, [150, 152, 153]), fully explained in Section 4.5).

Chapter 4

Experimental Methods

In this chapter, the femtosecond pump-probe experimental set-up and its most relevant components are presented. Subsequently, the Maximum Entropy Method, which is the approximation method used to derive the charge density maps from the experimentally measured variation of diffracted intensity, is discussed. The importance of the transient charge density maps lies in the fact that ultimately reveal the structural, charge and polarization dynamics in the photoexcited crystal and, in consequence, the software implemented to apply the Maximum Entropy Method (BayMEM) is also presented.

4.1 Experimental Set-up

In general terms, the experimental set-up is based on the ultrashort optical pump/X-Ray probe scheme summarized in Fig. 4.1. It consists of a Titanium:Sapphire laser system, the 'work horse' of ultrafast laser science, from which both the ultra-short optical pump and the X-Ray probe pulses are derived. The figure shows how the 800nm beam coming out of the Ti:Sa Spitfire PRO laser system ([154, 155]) is subsequently steered into a 80%/20% beam splitter that separates the optical pump and X-ray probe arms. Most of the laser beam, i.e., 80%, is dedicated to the generation of the X-rays by focusing it into a copper target, whereas the other 20% is dedicated to the optical pump. This approach ensures a synchronization between pump and probe pulses much better than 100fs.

It is worth mentioning the other key elements in the experimental set-up, that are also shown in the figure, i.e., the high-precision time delay stage and the chopper operating at 12.5Hz with photodiode. The time delay stage is used to vary the delay between pump and probe, thus, scanning the response of the photoexcited sample. The chopper and photodiode system serve the purpose of improving the signal-to-noise ratio (described fully in Sec. 4.4).

In the final stage of the experimental set-up, the optical pump at 400nm, which is obtained by frequency doubling with the help of a BBO, induces ultrafast structural changes in the ferroelectric ammonium sulphate polycristalline powder sample via 3-photon absorption, whereas the X-Ray probe is used to map those dynamics along a certain time range ([156]).

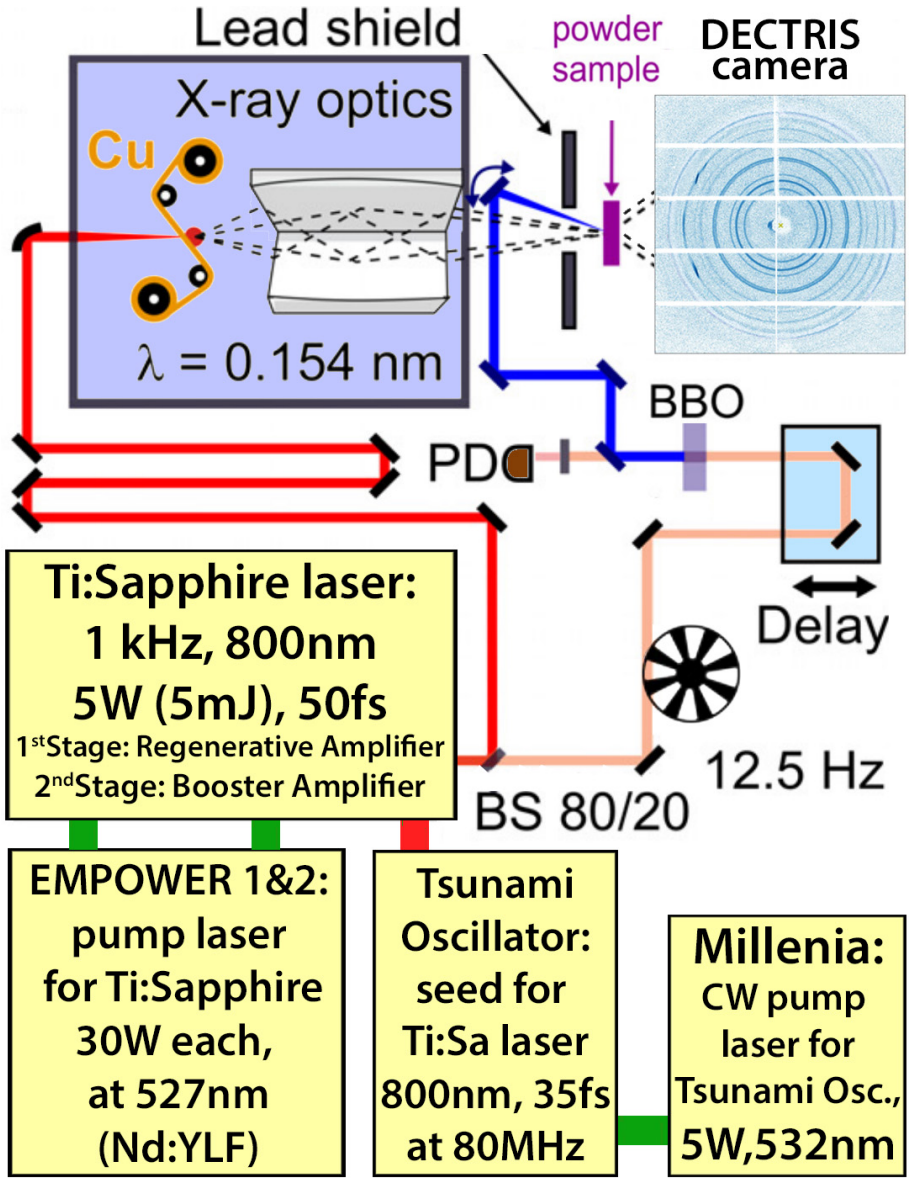

Figure 4.1: Schematic with the details of the different stages of the experimental set-up. The 800nm 50fs-length laser pulses from the Ti:Sapphire Spitfire PRO system ([154, 155]) are produced at a 80MHz rate by a Kerr-lens mode-locked TSUNAMI Oscillator, which is driven by a MILLENIA continuous wave pump laser emitting 5W radiation at 532nm (Spectra Physics, [157, 158]). Some of these low energy pulses are selected and amplified with a 1kHz rate in a two stage CPA set-up, that consists of an initial regenerative amplifier followed by a double-pass booster amplifier. Both of these stages are driven by Q-switched EMPOWER pump-lasers emitting 30W at 527nm radiation. The Spitfire PRO final output beam is p-polarized, i.e., parallel to the optical table on which the system is mounted ([26, 159, 160]). The 800nm beam coming out of the Ti:Sa laser is consecutively steered into a 80%/20% beam splitter that separates it into the optical pump arm (20%) and X-Ray probe arm (80%). In the final stage, the optical pump at 400nm, which is obtained by frequency doubling with the help of a BBO, photoexcites ferroelectric ammonium sulphate polycristalline powder sample via 3-photon absorption, whereas the transient X-Ray pattern is recorded by the dectris camera to map its dynamics with the help of the delay stage ([156]). The whole X-Ray source is enveloped in a lead cocoon to avoid leakings of the dangerous hard X-Ray generated within (Cu-K_α with photon energy of 8.048keV and λ=0.154nm). The X-Ray pulses are focused onto the sample with the help of a Montel optics component. Finally, the chopper at 12.5Hz and photodiode will allow a data treatment that greatly reduces the noise in the X-Ray measured signal (fully described in Sec. 4.4).

4.1.1 Spitfire PRO Ti:Sapphire Laser System

The technical details of the Ti:Sapphire laser system, the optical pump and X-ray probe arms are given here ([26, 159, 160]).

The commercially available two-stage Ti:Sa Spitfire PRO laser system is at the centre of the experimental set-up ([154, 155]). It is based on chirped pulse amplification (CPA) technology, which is used to amplify ultrashort laser pulses up to the petawatt level. CPA is currently state-of-the-art technology, and almost all of the highest power lasers in the world, i.e., greater than ∼100 terawatts, currently utilize it. The necessity for the CPA technique is based on the fact that the usual peak intensity of ultrashort pulses exceeds the damage threshold of the optical components the laser system.

The Tsunami oscillator is pumped by a continuous wave Millennia Pro laser (Spectra Physics, [157, 158]). By means of its prism-free chirped mirror design, it is able to generate low-energy pulses centered at 800nm, with a duration of 35fs, and a repetition rate of 80MHz ([161]). The Tsunami beam subsequently acts as a seed for the Spitfire Pro where a fast-switching high-contrast Pockels cell selects one in 8×10^4 pulses, and with the help of the regenerative amplifier and the double-pass booster amplifier (pumped with two Q-Switched, intracavity frequency-doubled Nd:YLF 20-Watt lasers at 527nm, [162]) yields at the exit of the Spitfire a pulsed beam of 1kHz repetition rate of 5mJ (5 Watts) with a duration of 50fs and intensities on the order of $10^{18}\,\mathrm{W/cm^2}$ ([163, 164]).

The *Amplified Spontaneous Emission* (ASE) is an important parameter that affects the temporal contrast of the main pulse with relation to the background emission, and has to be considered in these type of systems to ensure proper functioning. The background emission originates spontaneously in the regenerative cavity creating pre-pulses in the ps-range ([165–167]). A low ASE is important to avoid the appearance of pre-pulses that would impair the generation of X-Ray, and in this system the background emission is reduced by at least five orders of magnitude ([168]). Another important parameter is the shot-to-shot peak energy fluctuation which for the Ti:Sa Spitfire PRO system is at the low value of ≈0.3% ([169, 170]).

The main parameters of the laser system ([156, 171]) are summarized in Table 4.1.

Ti:Sapphire Spitfire Pro Laser System	
Ti:Sa Laser central Wavelength	λ = 800nm
Ti:Sa Pulse Energy	5mJ
Ti:Sa Pulse Duration at 800nm	50fs
Repetition Rate	1kHz
Diameter of outcoming beam	2.5cm
Ti:Sa Laser Power	5W

Table 4.1: Main parameters of the Ti:Sa laser system at the heart of the experimental set-up.

4.1.2 Optical Pump Arm Set-up

As previously introduced, in the optical pump branch there are three main elements, the delay stage, the chopper with photodiode, and the BBO. Right after the beam splitter, 20% of the 800nm beam is directed through a delay stage to be able to collect transient experimental data along a certain time range, and the chopper with photodiode allows for the improvement of the signal-to-noise ratio (fully described in Sec. 4.4), and Refs. [25, 172, 173]).

At the end of the path for this branch, an optical pump at 400nm the pump beam is finally focused onto the sample. The optical pump at 400nm is generated by frequency doubling of the fundamental 800nm beam from the Ti:Sapphire system in a 250-μm-thick BBO (type I phase-matching), and consists of pulses with 110μJ energy and 70fs length. Although in the experiment presented in this thesis a 400nm pump is used, the system offers the possibility of also working with the fundamental 800nm pump or a 266nm pump produced by frequency tripling.

In the final stage of the experimental set-up, the optical pump is finally focused onto the sample where it induces ultrafast structural changes in the ferroelectric ammonium sulphate polycristalline powder sample via 3-photon absorption, whereas the Cu-K$_\alpha$ X-Ray probe is used to map those dynamics (fully explained in [156]).

4.1.3 X-Ray Probe Arm Set-up

The process of generating and focusing the X-Ray probe onto the powder ferroelectric ammonium sulphate sample with which to map its transient interaction with the pump consists of the following steps:

- Right after the beam splitter, 80% of the energy of the 800nm output beam is steered onto a 20 micrometer-thick spooling copper target located in the interior of a vacuum chamber at $\sim$0.1 mBar by means of a 2-inch diameter 90° off-axis parabolic golden mirror with focal length of 100mm. The actual position of the focused beam in the vacuum chamber can be tuned by means of different electrical micrometer screws controlled from the outside, and must be optimized for a focal spot size on the copper target of $\sim$10 micrometer diameter (FWHM), which corresponds to a power density of I_{peak} $\sim$1.3·10^{18} W/cm^2.

- The interaction of the focused 800nm beam on the copper target generates an X-Ray source that emits radiation with different characteristic energies in a 4π sphere (the underlying physics of the X-Ray generation are described in the following section). The necessity to contain this part

of the system in a vacuum chamber at a low pressure is due to the fact that without it, pre-plasma appears on the surface of the copper target due to the remanent amplified spontaneous emission (ASE), which severely impairs the generation of X-Ray ([174]). The irradiated area will be damaged irreversibly by the continuous operation of the laser beam, given the peak intensities $\sim 10^{18}$ W/cm^2, which makes it necessary to procure a fresh metal target for each laser pulse that arrives at every millisecond ([156]). With this purpose, the copper tape is mounted on a rotating spool, that moves the target at a certain pace ($\sim$ 9 cm/s), to maximize the generation of X-Ray.

It also bears mentioning that since the 800nm beam is focused on the surface of the copper target, a shock wave appears due to the thermal heating, that ejects copper dust and small fragments ([175]). To properly maintain the generation and stability of the X-Ray source, two additional bands moving at a speed of $\sim$10 cm/s are mounted in the vacuum chamber. There is a 50 micron-thick band before the copper target composed of polyesther, which is mostly transparent to the incoming 800nm beam. After the copper target, there is a 23 micron-thick hostaphan band, likewise, mostly transparent to the outcoming X-Ray pulses. These bands prevent the debris accumulation that would provoke the degradation of the copper band and absorb an important part of the generated X-Ray.

- Subsequently, part of the X-Ray radiation escapes out of the vacuum chamber through a slit, which is sealed by a 35µm-thick Kapton tape (high X-Ray transmitivity material, i.e., $\approx$99.9%, [176, 177]) to maintain the $\sim$0.1 mBar pressure. A Montel X-Ray optics will collect a part of those exiting Cu-K_α photons and focus them onto the powder sample (flux of $\approx 4 \cdot 10^6$ photons/s, [156]). These kind of optics are necessary in time-resolved experiments to monochromatize the source of X-Ray, and achieve a proper Signal-to-Noise Ratio (SNR) by maximizing the photon flux on the sample (the operation of the Montel optics is described in the following section).

- In the final step of the experiment, the time-resolved powder diffraction pattern (i.e., Debye-Scherrer Rings) generated from the interaction of the X-Ray probe beam with the photoexcited sample is recorded by the large-screen Dectris Pilatus 1M detector (described in Section 4.1.3). By means of a complex treatment of the large collected data (about 5 Gigabytes per 8 hours of experiment) and with the help of the Maximum Entropy Method ([152]) the transient charge density maps with a spatial resolution of 30pm and 100fs temporal resolution ([25, 171]) are derived (fully explained in Section 4.5.1).

X-Ray Source

The underlying physics of the process of X-Ray generation are explained in this section (Fig. 4.2).

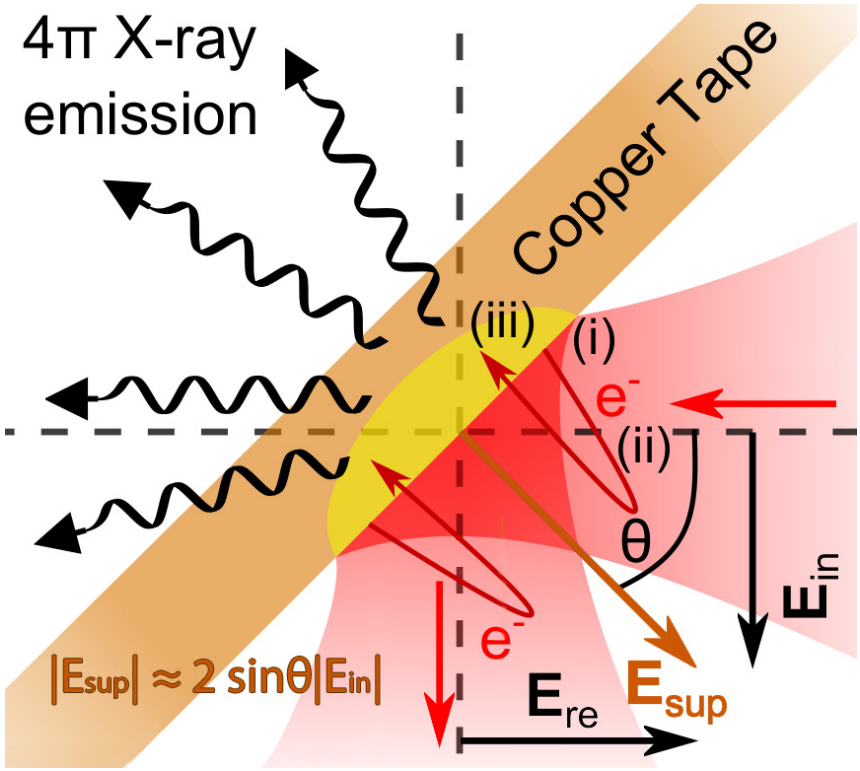

Figure 4.2: The scheme describes the X-Ray generation process in three steps: i) Some copper electrons are ejected out into the vacuum by the process known as *'strong field tunnel ionization'* ([178]) under the effect of a strong induced electric field. ii) Part of the expelled electrons gain high kinetic energy under the effect of the strong oscillating field, and are smashed back into the copper target. iii) When the fast electrons re-enter the copper target, decelerate by collisional inner-shell ionization, and generate a characteristic X-Ray emission and Bremsstrahlung into the full $4{\cdot}\pi$ solid angle (shown in Fig. 4.4). The black straight arrows on the picture symbolize, respectively, the incoming electric field (E_{in}) and the reflected electric field (E_{re}). Both fields add up to a total superimposed oscillating electric field of $E_{sup} \sim 2 \cdot \sin\theta{\cdot}E_{in}$.

The process of X-Ray generation can be summarized into three distinct steps:

1. When the incoming 800nm pulse impacts onto the 20µm-thick copper surface, it produces a strongly oscillating induced electric field in the form of a standing wave, E_{sup}. It is generated by the sum of the incoming electric field (E_{in}) and the reflected electric field (E_{re}), that add up to a total superimposed oscillating electric field of $E_{sup} \sim 2 \cdot \sin\theta{\cdot}E_{in}$ (Fig. 4.2). The field E_{sup} reaches a peak in the order of $E_{sup} \sim 10^3$ V/nm (i.e., intensity peak in the order $I_{peak} \sim 10^{18}$ W/cm^2), which is high enough to extract electrons through the metal-vacuum barrier by tunneling ([171]), and eject them into the vacuum surrounding the metal target.

The probability of extraction is described by quantum mechanics and is maximized for a superimposed oscillating electric field, E_{sup}, that is perpendicular to the metal surface, reaching strengths in the order of E_{sup} ∼100-1000 V/nm. In this sense, the relative angle of incidence of the incoming 800nm beam focused onto the metal surface has an influence, being the optimal situation Θ ∼60°, which procures the perpendicular superimposed oscillating electric field, E_{sup} ([156, 178, 179]).

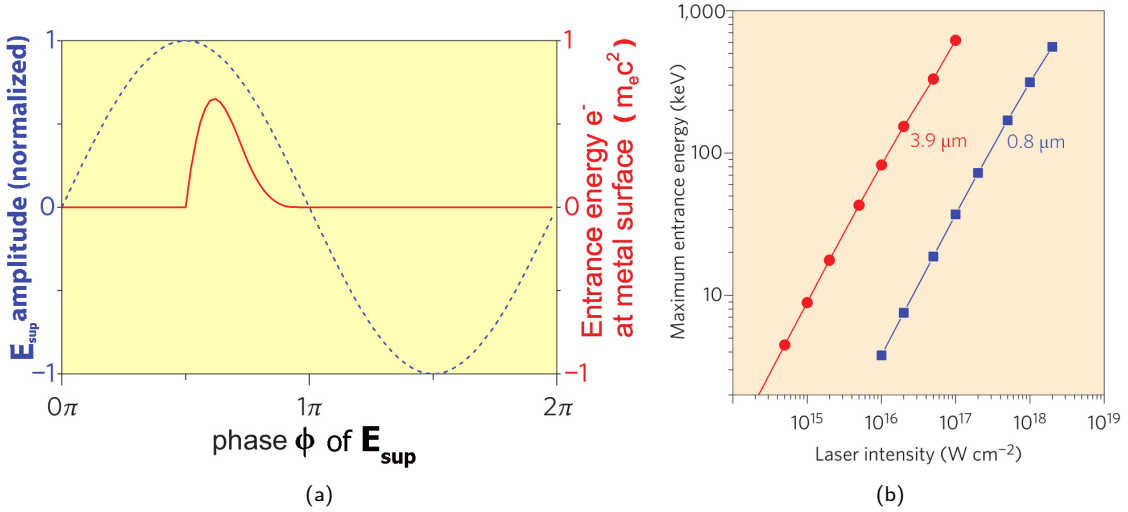

Figure 4.3: Sub-Fig 4.3(a): The electron trajectory depends sensitively on the phase ϕ of the cycle of the electron-driving oscillating electric field in the form of a standing wave, E_{sup} (dashed blue curve, scale in left ordinate). The solid red line shows the entrance energy of the electrons when they reach back the surface of the copper target as a function of the phase ϕ of the oscillating electric field E_{sup} (scale in the right ordinate). Sub-Fig 4.3(b): entrance energy of the electrons hitting the metal surface as a function of the laser intensity for two different driving lasers (λ=0.8μm in blue and λ=3.9μm in red) [179].

2. Not all the electrons expelled out of the copper surface by the tunnelling effect (*vacuum heating* or *Brunel effect*, [180]) induced by the electron-driving oscillating electric field, E_{sup}, will contribute to the generation of X-Rays. It depends on the phase of the optical cycle of E_{sup} as shown in Fig.4.3(a). As can be seen, only the generated free electrons that are driven by the oscillating electric field E_{sup} that points outwards of the copper target,i.e., only the electrons that are driven by the oscillating electric field E_{sup} with phase $\pi/2 \leq \phi \leq \pi$, are capable of impinging back onto the target, while the effect is maximized for the phase $\phi = 3\pi/4$ ([171]).

   Contrarily, the generated free electrons under the effect of the driving field with phase $0 \leq \phi \leq \pi/2$ are accelerated out into the vacuum due to the high electric fields but their kinetic energy remains so low that these do not strike back onto the metal within the optical period and do not contribute to the generation of X-Ray radiation.

Finally, the generated free electrons under the effect of E_{sup} in the second half-cycle, $\pi \leq \phi \leq 2\pi$, suffer no acceleration since the direction of the driving electric field points inwards the surface of the copper band and gets shielded within a few nanometers into the metal.

It is worthwhile to mention that the maximum kinetic energy that the electrons reach by the end of this process depends on several factors, the most important being the electric field strength (or equivalently, the intensity of incoming pulse), and the wavelength of the driving field, i.e., $K_{max} \sim I_0 \cdot \lambda^2$ ([171]). According to this fact, electrons will reach higher kinetic energies under the effect of longer wavelengths since, generally speaking, in that case the electric field accelerates them for longer periods of time.

This fact has been proven by experiments comparing the effect of the 800nm Ti:Sapphire laser system with a 3.9μm optical parametric chirped pulse amplifier (OPCPA) driving laser system (Fig. 4.3(b) and [171, 181, 182]). The maximum kinetic energy acquired by the electrons with the Ti:Sapphire laser system at 800nm can be estimated to be ∼200keV, which corresponds to an electron driving-electric field of $E_{peak} \approx 1.7 \times 10^3$ V/nm perpendicular to the surface or, equivalently, to an intensity of $I_{peak} \approx 1.3 \times 10^{18}$ W/cm^2 [171]).

3. In the final step, the electrons that are smashed back into the copper target with high kinetic energy will penetrate its surface and decelerate abruptly by various interactions. The most relevant are the Bremsstrahlung and K-shell ionization, the latter with cross-section for 200keV electrons of $\sim 3.10^{-26}$ m^2 ([183, 184]). As can be seen in Fig. 4.4, electrons from higher shells will relax into the vacant K-shells (1s ground state) by emitting characteristic X-Ray photons isotropically into the full 4π solid angle that correspond, for the most part, to transitions from L_3, L_2 and $M_{2,3}$, associated to $K_{\alpha 1}$, $K_{\alpha 2}$ (transition 2p→1s), and $K_{\beta 1}$ (transition 3p→1s), along with broad Bremsstrahlung spectrum. In particular, the characteristic $K_{\alpha 1}$ photon is emitted as the recombination of a K-shell hole with an L-shell electron. Since $K_{\alpha 1}$, $K_{\alpha 2}$ are very close spectrally, these will be named K_α in general. The proportion between the generated Cu-K_β and Cu-K_α is an atomic characteristic value which for copper, in particular, is: Cu-K_β/Cu-K_α ∼0.12 ([176, 185–187]).

This process is based on the phenomenon of *fluorescence* (*spontaneous emission*) from which the lifetime of the hole states can be estimated to be at sub-fs according to the uncertainty principle and to the 3eV line width for Cu-$K_{\alpha 1}$ ([188, 189]). Therefore, it can be concluded that the temporal broadening of the X-Ray pulse duration due to the lifetime of this electronic state is negligible. Also, since the electrons are only accelerated under the direct effect of the 800nm 50fs-laser pulse, the X-Ray pulse duration has been measured to be ∼100fs ([151]).

The X-Ray source presents a shot-to-shot fluctuation in the order of 20-30% ([156]) due to different factors, the most relevant being the mechanical instabilities of the copper target and the variation of intensity from the Ti:Sapphire main beam (∼0.3%).

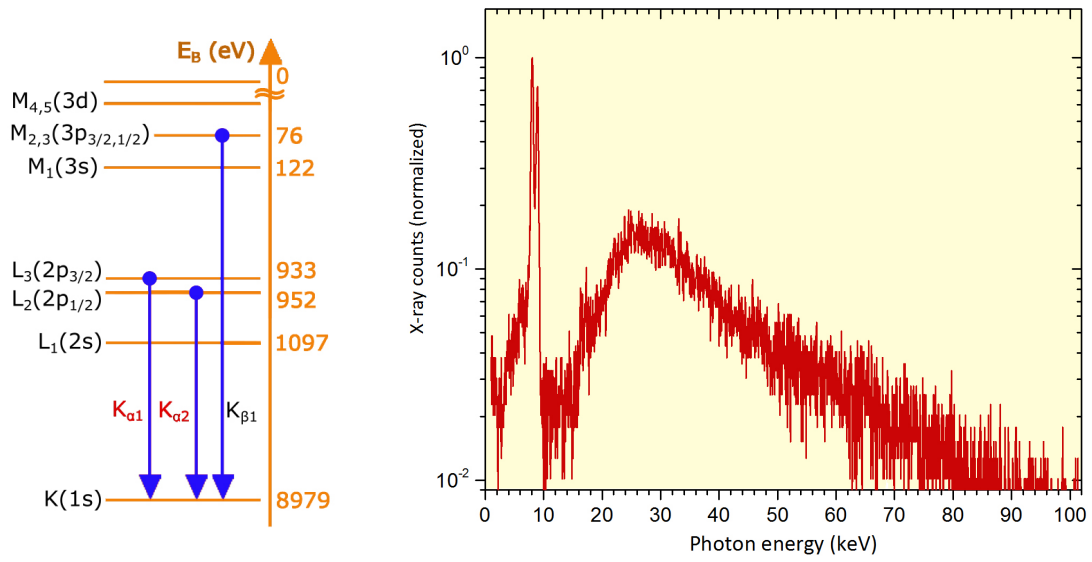

(a) (b)

Figure 4.4: **(a)**: Copper atomic energy levels with the electronic transitions corresponding to the characteristic radiation $K_{\alpha 1}$ (photon energy: $E_{K\alpha 1} = 8.048$ keV), $K_{\alpha 2}$ ($E_{K\alpha 2} = 8.027$ keV) and $K_{\beta 1}$ ($E_{K\beta 1} = 8.903$ keV). Also, here is introduced the nomenclature to label the absorption edges of the different elements. For example, the K edge consists of the energy required to eject one electron from the 1s shell to the continuum of free states, etc. The different electronic shells are labelled as (nl_j) where where n, l_j and j correspond to the quantum numbers principal, orbital angular momentum, and total angular momentum, respectively, and the multiplicity is given by $2j + 1$. **(b)**: X-Ray Spectrum generated by the interaction of the 800nm beam focused in a copper target accumulated in 4 minutes of exposition. The characteristic radiation for copper can be clearly identified in the K_α peak ($K_{\alpha 1}$ and $K_{\alpha 2}$ are indistinguishable with this energy resolution and conform an unique peak), and K_β peak. The rest of the radiation corresponds to interactions with the lead wall surrounding the X-Ray source and the broad Bremsstrahlung spectrum ([171, 188]). The strong decrease of Bremsstrahlung between 10 and 20 keV is due to the K-shell absorption in this range of energies for copper. The decay of the Bremsstrahlung between 30 and 100 keV is exponential, where its 'decay constant' corresponds to the temperature (i.e., energy) of the photons ([171]).

A summary of the most important features of the X-Ray Source for Cu-K_α is given on the Table 4.2.

X-Ray Source Characteristics	
Peak 800nm Pump Intensity in the focus	$1.3 \cdot 10^{18}$ W/cm^2
Pump 800nm Beamwaist in the Focus	2.6 μm
X-Ray Photons emitted in full sphere (4π sr)	$4 \cdot 10^{10}$ photons/s
Source Dimensions	$10(\pm 2)\mu$m
Cu-K_α Photon Energy	8.048 keV
Repetition Rate	1 kHz
X-Ray Photons on Sample	$4 \cdot 10^{6}$ photons/s
X-Ray Photons on Sample (per laser shot)	$4 \cdot 10^{3}$ photons/shot
X-Ray Probe Diameter on Sample	200 μm

Table 4.2: Parameters of the X-Ray Source ([156, 171]).

X-Ray Detection: Pilatus 1M Dectris Detector

One of the most important elements in the experimental set-up is the commercially available X-Ray detector Pilatus 1M Dectris. It consists of a camera with a large detection area (16.9×17.9 cm^2) divided in 2×5 detector modules with 981×1043 pixels on the whole. As can be seen in the Figure 4.5, the detection system that allows for the direct conversion of X-Ray photons into digital signals consists of the so-called *Hybrid Pixel Technology* (HPT, Fig. 4.5(a)) which incorporates two main components in each pixel: a so-called *sensor pixel* (silicon depletion volume with 320 µm of thickness and 172µm$\times$172µm of area) and also the *CMOS-based readout pixel*.

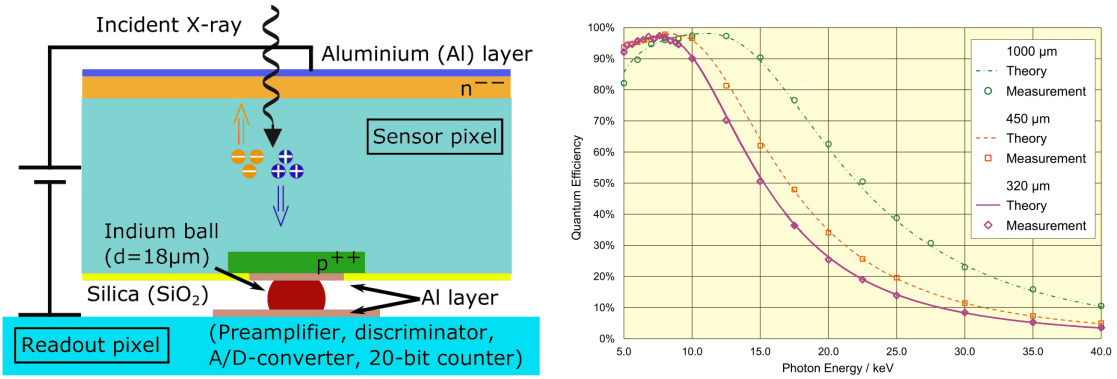

(a) (b)

Figure 4.5: Sub-Fig. 4.5(a)): Schematic of the Hybrid Pixel Technology for the Dectris Pilatus 1M, which is compounded by a silicon sensor pixel and a CMOS-based readout pixel ([190]). Sub-Fig. 4.5(b): Quantum efficiency of the silicon sensor in the Dectris 1M Pilatus camera detection system as a function of the incoming X-Ray photon energy ([191]).

The detection process starts with the generation of electron-hole pairs in the silicon-layered sensor pixel when X-Ray photons with a certain energy arrive on its surface. This primary photons are converted into electron-hole pairs with a quantum efficiency of $\geq$97 % as can be seen in Fig. **??** ([190–192]). The detector has a finely-adjusted point-spread function, i.e., less-than-one-pixel wide, to avoid the virtual spreading of intensities among consecutive pixels even when the signals are distinctively different.

The induced charge is transferred later with the help of an applied voltage bias through an 18μm-diameter indium channel to the readout pixel, where the outcome is amplified and recorded digitally with a high dynamic range readout of 20 bits. This permits that a whole X-Ray image is recorded with a frequency of up to 30Hz. The detector can reach a count rate of 2×10^6 photons/pixel/s when set in the so-called *continuous operation*, although in the present experimental set-up, the so-called *triggered-operation detector* is used, which permits to gate it electronically, and set the exposure time. Like that, the readout pixel is enabled only during 1 microsecond with which unwanted cosmic X-Rays can be discriminated. Given that the X-Ray pulses are generated at 1kHz, the counting rate is limited to a maximum of $2\times$ 10^3 photons/pixel/s.

In contrast to integrating detectors such as the charged coupled devices (CCD), the charge generated

when detecting the X-Ray is not accumulated with CMOS technology. Rather, it is directly digitized during the exposure to X-Ray, being the generated pairs of electron-holes directly proportional to the quantity of X-Ray photons. This makes the detector essentially free of dark current and, in general, of any analogue read-out noise.

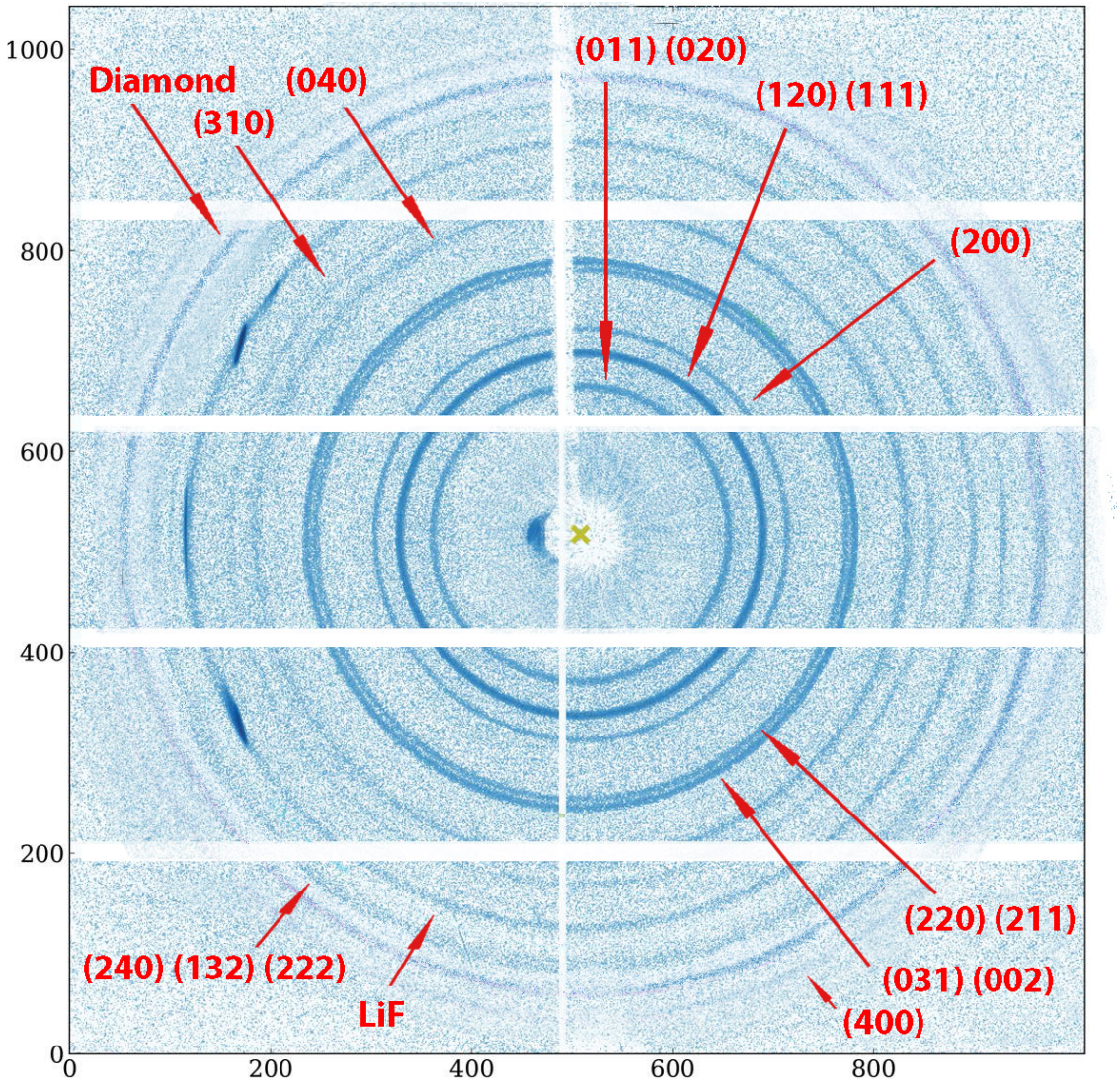

Figure 4.6: 2-Dimensional powder X-Ray diffraction pattern from unexcited powder ferroelectric ammonium sulphate at T = 200K as collected by the Dectris 1M Pilatus Camera during a exposure of 140 seconds. The miller indices corresponding to the Debye-Scherrer rings are given in the figure. The miller indices are obtained from the previous knowledge of the unexcited structure of ferroelectric ammonium sulphate in combination with the Bragg's law.

Figure 4.6 shows the diffraction pattern of the unexcited powder ammonium sulphate in its ferroelectric state at T = 200K, as recorded by the Dectris 1M Camera after 140 seconds of continuous exposition. As can be seen, there exist gaps in the detection area that for construction reasons are not sensitive to X-Ray photons. Nonetheless, the influence of the gaps on the measurements of the pho-

toexcited 2D powder diffraction patterns is minimized, since the crucial magnitude in the experiment is the transient variation of X-Ray diffracted intensity along the Debye rings ($\Delta I_{Ihkl}(t)/I^0_{hkl}$) rather than the absolute value for the X-Ray diffracted intensity ($I_{hkl}(t)$).

Additionally, it is worthwhile to note that, the samples consist of pellets composed of a compacted distribution of randomly oriented individual crystallites. Additionally, the powder sample is placed perpendicularly to the incoming X-Ray beam and continuously rotated with a speed of ∼1Hz during the experimental data acquisition, which results in almost homogeneous Debye-Scherrer diffraction rings with virtually no angular dependence for the X-Ray diffracted intensity.

Secondary detector: Amptek XR-100T Cd-Te

Since the generation of X-Ray is directly dependent on the proper tight focusing of the 800nm laser beam onto the copper target, a second X-Ray detector is used to optimise the position of the parabolic mirror that controls it by monitoring the total X-Ray flux.

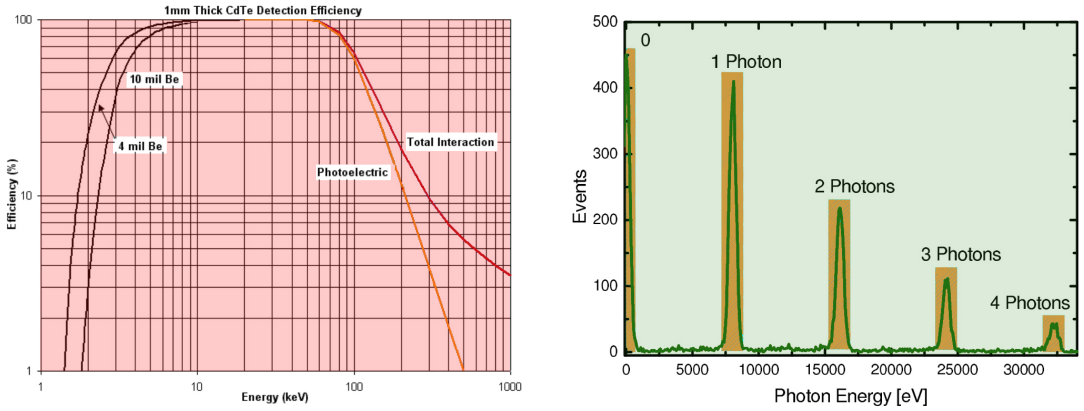

(a) (b)

Figure 4.7: The Amptek XR-100CdTe is an X-Ray detector based on a cadmium-teluride diode. 4.7(a): Photon-counting quantum efficiency as a function of the incoming X-ray photon energy. The high stopping power of the Cd-Te diode allows for the high efficiency detection of X-Ray photons with energies of up to 100keV. 4.7(b): Histogram of the photon energy for a certain Bragg diffraction when recorded with the AmpTek XR-100CdTe detector.

The smaller secondary Amptek XR-100T Cd-Te detector is based on direct detection by interaction of the X-Ray photons with an unique cadmium telluride photodiode with volumen 3mm× 3mm×1mm, and total surface active area of 9mm^2. It is mounted on a two-stage thermoelectrical cooler, and to allow for the vacuum with which the detector needs to work, a high X-Ray transmission 100μm–Beryllium window seals its entrance.

The detector has an energy resolution of 200eV, can spectrally resolve the arrival of X-Ray photons of up to 100keV and offers a very high quantum efficiency, i.e., 99% when counting photons with ∼10keV, or 97% in the case of Cu-K$_\alpha$ with 8.048keV (Fig. 4.7, and Refs. [193, 194]).

The Amptek Cd-Te photodiode can read with frequency of up to 1kHz and if necessary, it can be synchronized, i.e., triggered, by the Ti:Sa laser system. The figure 4.7(b) shows that the measurement of a Bragg-diffraction is a histogram of the photon energy. It was recorded from the set-up X-Ray source and, as can be seen, multiphoton events occur. However, these can be resolved by basing on the energy information received by the detector and identified accordingly.

Montel Optics

An X-Ray optics component is mandatory in this sort of time-resolved experiment to focus and achieve a sufficiently large flux of X-Ray photons on the sample and increase the Signal-to-Noise Ratio (SNR, [156]). There exist various types of X-Ray optics that base their operation in mirrors. These are classified by the different arrangements of the mirror substrates and their geometry, e.g., Schwarzschild Optics uses curved mirrors, Wolter Optics uses an elliptical or parabolic mirror followed by another hyperbolic mirror, Montel Optics uses multi-layer mirrors, etc. Several X-Ray optics have been considered in the past for this experimental set-up, being the multilayer X-Ray Montel optics (Incoatec GmbH) the optimal option ([175, 195]). It is composed of two perpendicularly arranged elliptical multilayer mirrors (Fig. 4.8) described by the Kirkpatrick-Baez scheme ([196]) where high reflectivity is ensured by the gradual variation of thickness along their surfaces.

As previously commented, the X-Ray radiation escapes out of the X-Ray source located within the vacuum chamber through a slit that is sealed by the almost transparent-to-X-Ray Kapton tape. Right in front of the slit is located the Montel optics that will collect and focus the X-Ray photons on a spot of the sample surface with $\sim$200μm diameter (Full Width Half Maximum, FWHM). The Montel optics is spectrally selective since it is based on the Bragg's Law for reflections at a very small diffraction angle, i.e., $\sim 3°$. For this situation, virtually only the copper K_α photons satisfy the Bragg condition along its surfaces.

Finally, it bears mentioning that the sample is positioned at a distance of 50cm away from the X-Ray source because like that, the divergence of the beam is minimized due to the 1:3 magnification of the Montel optics ([156]). Also, given that the penetration depth of the X-Ray photons into the multilayer stack is very small, it only causes a temporal broadening of the X-ray pulse duration in the order of $\sim$5fs that can be considered as negligible.

The Montel optics ensures a high suppression of the generated radiation that does not correspond to the Cu-K_α as can be the Bremsstrahlung radiation or the other characteristic lines in the source as Cu-K_β. In this sense, the ratio of the reflectivity of Cu-K_β/Cu-K_α was determined at $\sim 5\times 10^{-4}$ with which almost background-free measurements can be performed ([175, 195]).

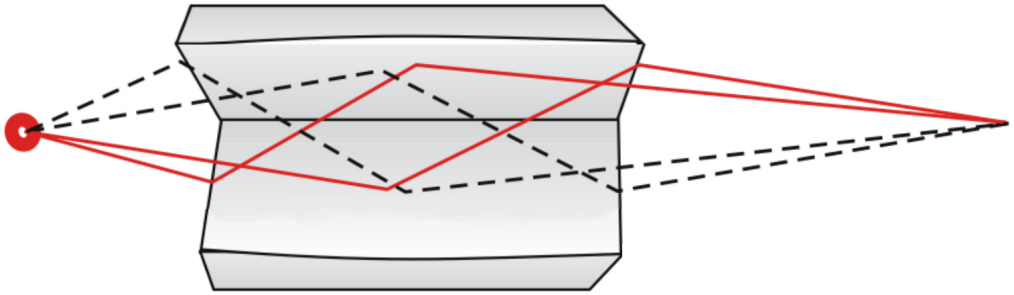

Figure 4.8: Depiction of the mirrors of the Montel Multilayer Optics in the Kirkpatrick-Baez Scheme. Photons are collected from the left side and are focused on the right side by double-reflection in the perpendicularly-disposed elliptic multi-layer mirrors.

Taking into account that the point-like emitter at the source generates $\sim 4\times 10^{10}$ X-Ray photons/s in 4π solid angle, where the Montel optics has a coefficient of 20% of transmission of all the photons collected with its 10^{-3} sr solid angle ([175]), and the transmission through air causes an absorption of 50% of the X-rays, it can be concluded that the experimental set-up is able to procure $\sim 4\times 10^{6}$ photons/s on the sample ([156]).

Time Delay Zero

The determination of the *time delay zero*, i.e., the instant in which the optical pump and X-Ray probe pulses overlap temporally on the sample, is crucially important since it sets the starting point for the dynamics in the photoexcited ferroelectric ammonium sulphate. Time delay zero is also used as time reference when stacking together the collected data from different experiment days, given the necessity to do so, to compensate for the low flux in the X-Ray source and, hence, achieve a sufficiently high Signal-to-Noise ratio (the SNR concept is fully described in Sec. 4.4).

To establish the time delay zero in the pump-probe experiment described here, a routine is followed at the beginning of every experiment ([126]). The process can be summarized in the following steps:

- First, the optical pump beam and the 800nm beam that generates the X-Ray probe are aligned through a 200µm-diameter pinhole located at the powder sample position to ensure geometrical overlap. Subsequently, to obtain the temporal overlap in a first approximation, a type I BBO crystal is placed at the powder sample position. By scanning along a certain time range with the help of a high-precision delay stage, the temporal reference, i.e., time delay zero, at which the 400nm-optical pump and the 800nm pulsed beam interact simultaneously is measured with the help of a BBO crystal in an all-optical cross-correlation ([197–199]). However, even if this methodology gives a good approximation, the time delay zero calculated in this fashion corresponds to the 400nm pump and the 800nm beam that generates the X-Ray, but not to the X-Ray probe itself.

- Secondly, to determine the pump-probe time delay zero with the actual optical pump and X-Ray probe, a sample of epitaxially-grown 40nm-thick single-crystal bismuth must be used, given that this element undergoes an strong ultrafast structural change when optically excited with a 400nm-pump ([200–203]. The interaction is then scanned along the time range obtained as first approximation in the previous cross-correlation of 400nm and 800nm, and the variation of intensity in the Bragg reflection (111) is measured, given that this produces the strongest reaction of them all ([126]). At a certain time point, a quasi-instantaneous strong step-like decrease of intensity is observed in (111), which defines the time delay zero (Fig. 4.9) with a high time resolution of ∼100fs ([25]). As a last step, once identified the time delay zero, the spatial overlap can be improved by slightly varying the location of the pump over the bismuth sample and looking for the highest variation of signal over and over again.

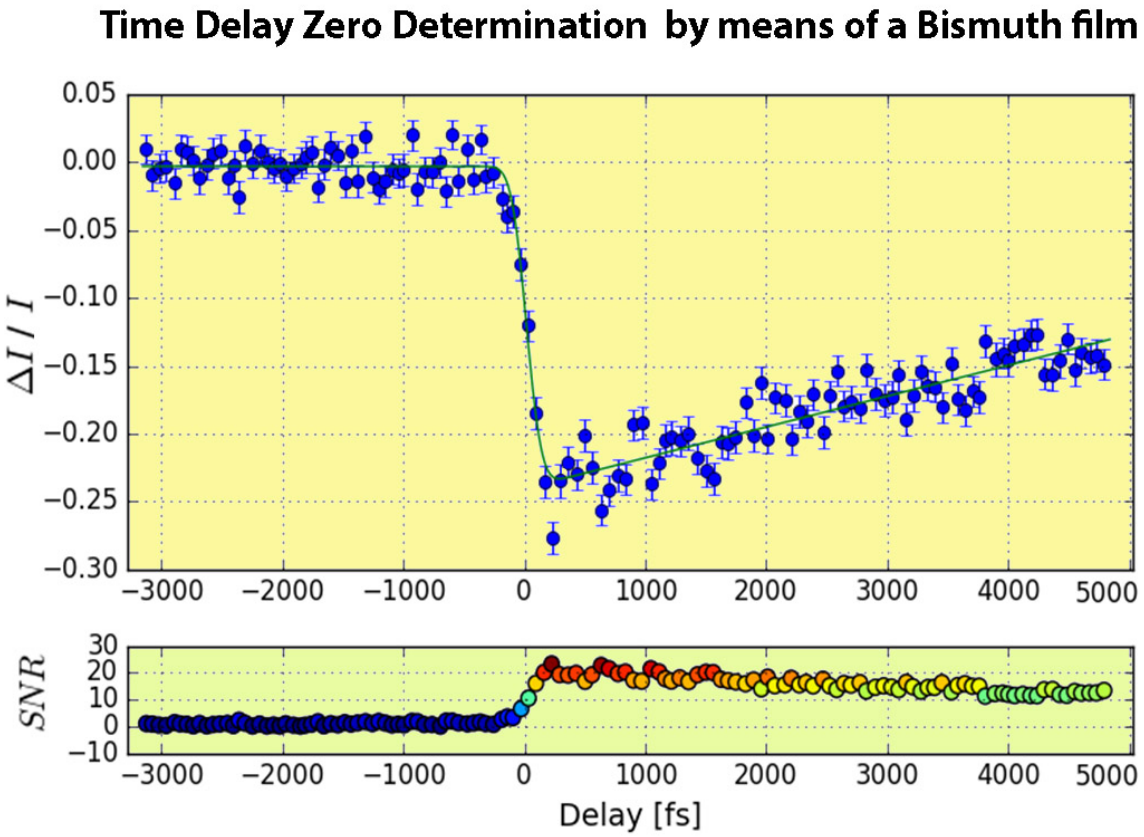

Figure 4.9: Transient measurement of photoexcited bismuth upon photoexcitation for the variation of intensity in the (111) Bragg reflection. The strong signal variation identifies the instant in which the pump and probe pulses overlap, i.e., the time delay zero. In the figure, the time range has been re-scaled to make it coincide time delay zero with t = 0. The binning method used to derive the graph corresponds to 133 points with error bars of ∼1.1% and time width between binned data points of ∼60fs, while the signal-to-noise ratio reaches a high enough value (≈20).

4.2 Sample Preparation and Low Temperature Configuration

Tightly-pressed pellet samples of ammonium sulphate were prepared every experiment day afresh from commercially available ammonium sulphate powder (Alfa Aesar, purity of 99.999%). The starting material used in the pellets, was grinded down beforehand with the help of mortar and pestle for approximately fifteen minutes resulting in an average of crystallites in size of sub-10 microns. Subsequently, the powder was compressed with an hydraulic press into pellets of $\sim$40-μm thickness, which were thereafter placed in a PVC holder between a 100μm-thick Lithium Fluoride (LiF) entrance window, and a polycrystalline 20μm-thick diamond exit window as shown in Fig. 4.10. The details of the estimated pump and probe sizes, i.e., full width half maximum (FWHM), are also given, with a depiction of the concentrical region where the pump and probe overlap during the experiment.

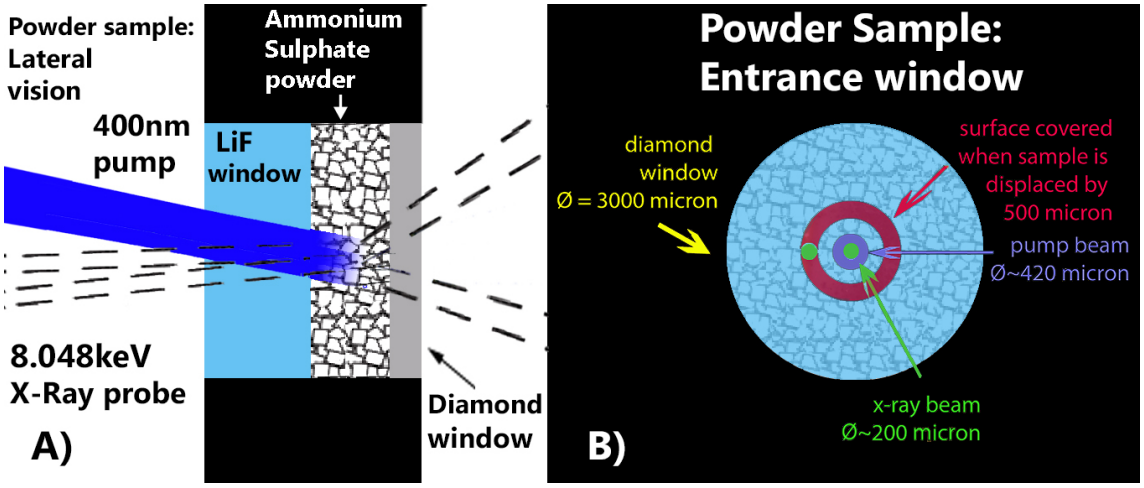

Figure 4.10: Schematic of the powder sample. The figure shows the lateral (A) and frontal (B) vision of the configuration of the powder pellets compressed between the LiF window and the diamond window. The relative sizes of the pump and probe beams are shown as well.

At the beginning of each experiment, the sample under optical excitation was slowly cooled down by using a nitrogen gas flow (Oxford Instruments CryojetHT) until the phase transition was reached. When ammonium sulphate experiments the para- to ferroelectric change of phase, an abrupt variation of the unit cell volume takes place caused by the sudden variation of lattice parameters, in special of the a-parameter (Fig. 4.11).

Hence, the change of phase can be easily identified given that certain Bragg peaks, particularly those where the Miller indices are dominated by the lattice parameter 'a', exhibit a shift in the diffraction angle, e.g., the (200) Bragg peak. The sudden changes occur in a range of approximately 10K in the vicinity of the Curie temperature, i.e., $T_C = 223$K ([7, 104]).

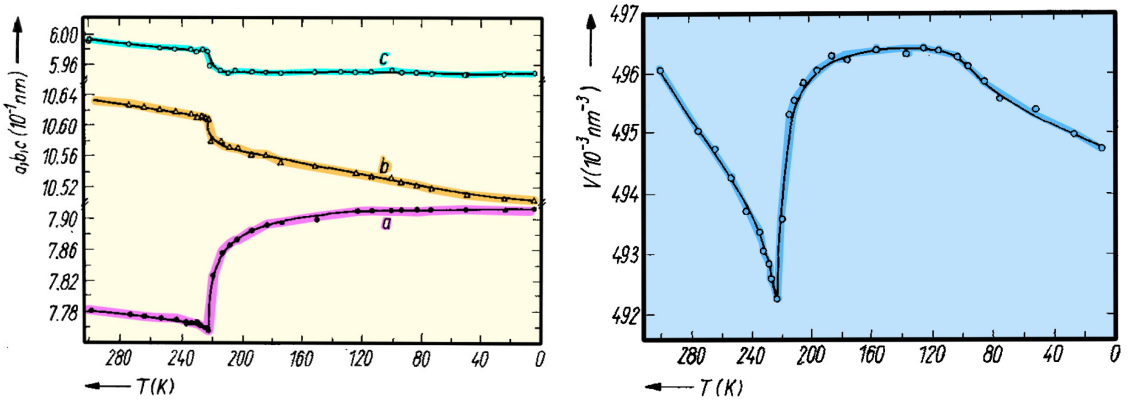

(a) (b)

Figure 4.11: Variation of lattice lengths and volume of the unit cell of $(NH_4)_2SO_4$ as a consequence of the temperature-dependent structural para- to ferroelectric phase transition ([69]). Sub-Fig. 4.11(a): Temperature dependence of lattice constants a, b and c. Sub-Fig. 4.11(b): Temperature dependence of the volume of the unit cell.

Fig. 4.12(a) permits to appreciate the differences between the diffraction patterns for unexcited ammonium sulphate in the paraelectric state (room temperature, T $\sim$ 280K) and ferroelectric state (T $\sim$ 200K). To better illustrate the subtle changes, Fig. 4.12(b) shows the differential intensity diffraction patterns for unexcited ferro- and paraelectric ammonium sulphate. The figure shows that the most recognisable feature that permits to recognise that the change of phase has taken place, is the shift at diffraction angle $2\Theta \sim 29^{\circ}$ accompanied by a strong variation of diffracted intensity. Once the change of phase has been accomplished, the sample is still cooled down by 20K more reaching T = 200$\pm$5K, i.e., well below the transition temperature, T_C = 223K. By doing so it, is ensured that, even under pump excitation conditions, the para- to ferroelectric phase transition is not crossed over and the ammonium sulphate sample remains in the ferroelectric phase throughout all the experiment time ([5, 35, 64, 69, 97]).

To conduct a successful experiment, it is crucial that the surfaces of the ammonium sulphate pellet in the sample are in good contact with the entrance and exit windows. This is due to the fact that these act as a heat sink which avoids a premature degradation of the sample that would otherwise scramble the signal. In this same sense, one shall avoid to hit the sample permanently on the same spot with the optical pump beam. This is accomplished with the help of a small electric motor with which the holder is rotated around the axis of the incoming X-Ray probe beam. Given that the sample consists not of a single crystal, but of regions of randomly-orientated compressed crystallites, this situation also ensures an average homogeneous photoexcitation during all experiment time. Moreover, the sample holder is located on top of a three-dimensional linear translation stage that allows for a precise alignment of the ferroelectric ammonium sulphate pellet with both the optical pump and X-Ray probe beams. As one last crucial step, a Kapton tape housing is placed surrounding the whole set-up to avoid the appearance of icing on the sample that would disrupt both the pump photoexcitation and the probe X-Ray diffraction. In addition, analogous experimental measurements of the variation of diffracted intensity were taken at the substantially lower temperature of 110K with results significantly different from those obtained at 200K. This suggests the existence of radically different temperature-dependent charge density dynamics, even within the same ferroelectric phase (discussed in Chapter 5).

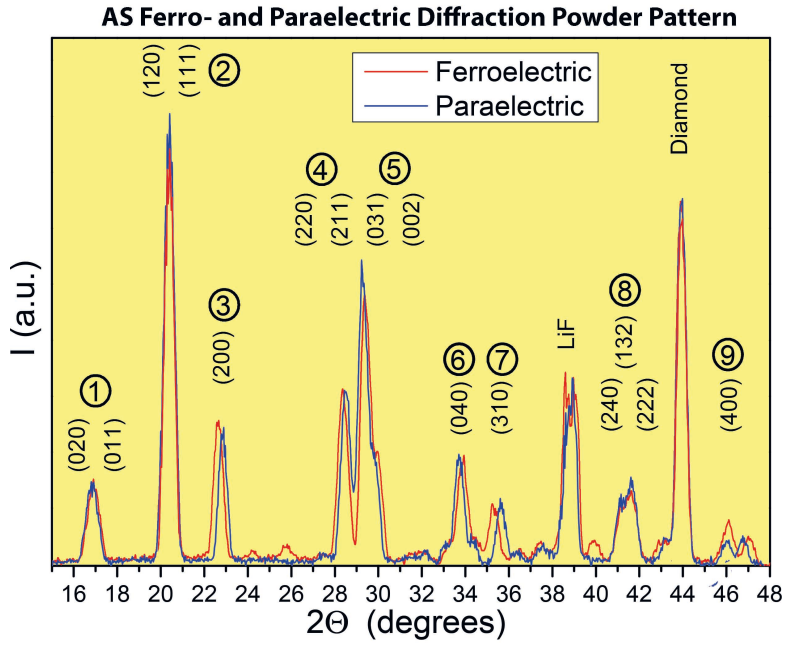

(a)

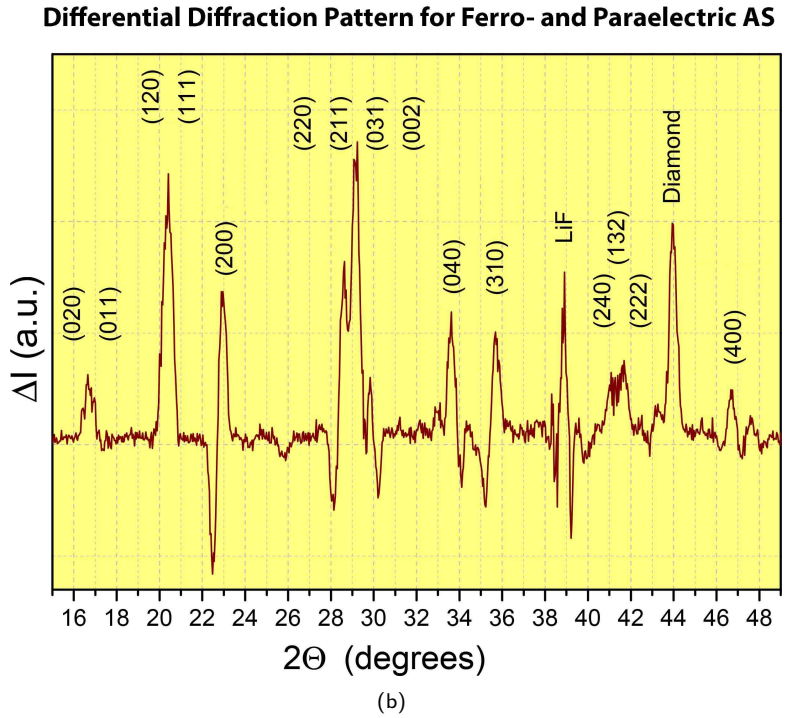

(b)

Figure 4.12: **(a)**: Diffraction pattern for ammonium sulphate in the paraelectric state (room temperature, T∼280K) and ferroelectric state (T∼200K), as a function of the scattering angle.
(b): Differential intensity in the diffraction powder pattern for the para- and ferroelectric states of ammonium sulphate as a function of the scattering angle. The figure shows that the most recognisable feature that permits to recognise that the change of phase has taken place, is the shift at diffraction angle $2\Theta \sim 29^{\circ}$ accompanied by a strong variation of diffracted intensity. In the figures can be seen the Miller indexes assigned to the diffraction peaks for para- and ferroelectric ammonium sulphate, and also the diamond and lithium fluoride windows diffraction peaks.

4.3 Identification of the Bragg's Peaks for ferroelectric ammonium sulphate

Figure 4.13 shows the static diffraction pattern and the transient variation of diffracted intensity as a function of the diffraction angle 2θ and the pump-probe time delay.

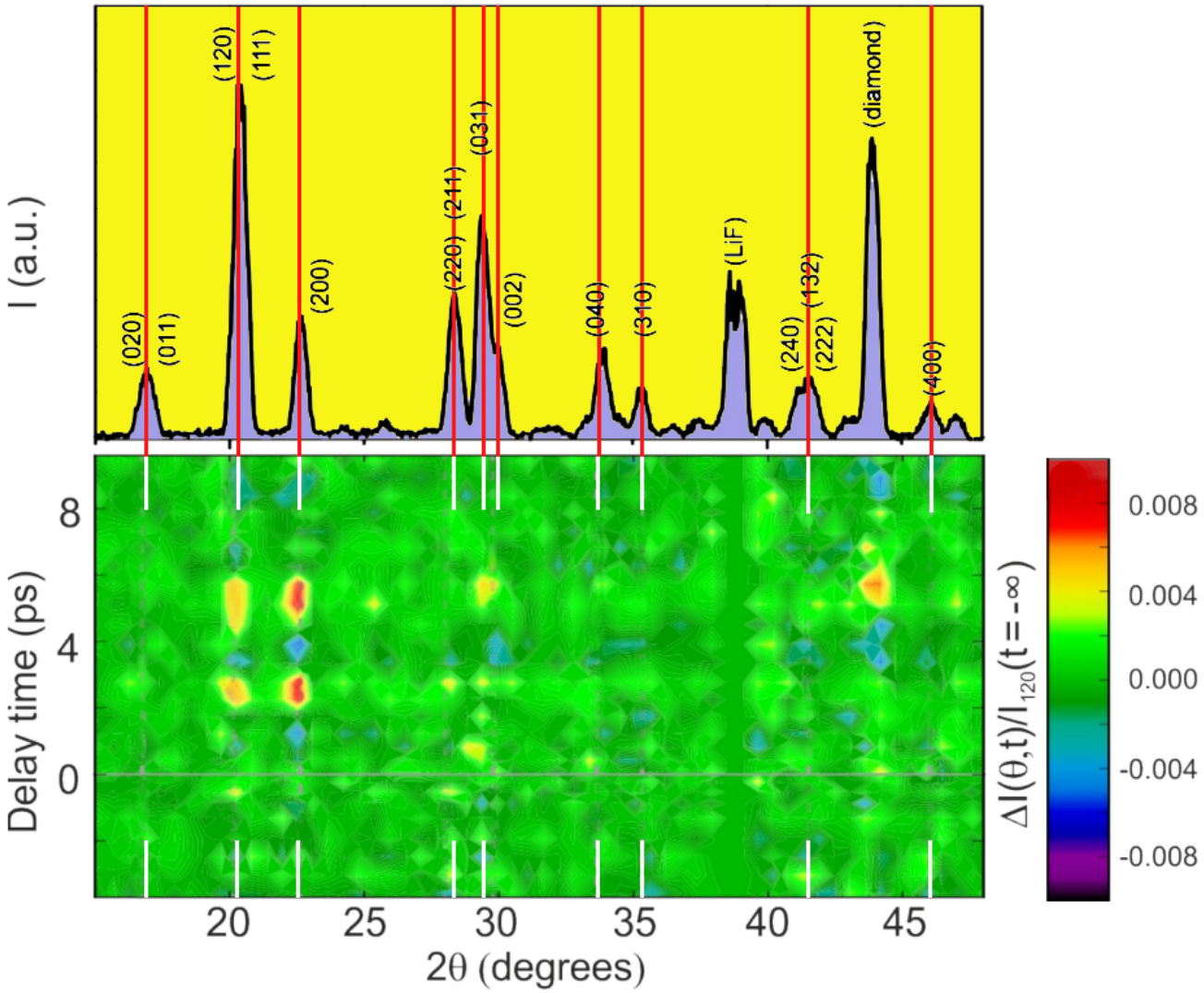

Figure 4.13: **Upper panel**: representation of the static integrated X-Ray Debye-Scherrer rings along the diffraction angle 2θ. It has been accumulated in a period of 140s, and the Bragg peaks are normalized to the highest diffraction peak, which in the case of ferroelectric ammonium sulphate corresponds to (120). **Lower panel**: normalized diffracted X-Ray variation of intensity, $\Delta I_{Ihkl}(t)/I^0_{hkl}$, plotted as a function of the scattering angle 2θ and the pump-probe time delay. As can be seen, some of the Bragg peaks are virtually unaffected by the photo-excitation of the ferroelectric ammonium sulphate (green zones), while others exhibit significant transient variations of intensity (yellow, blue and red zones). This graphical representation allows for the straightforward identification of the Miller indices for the Bragg peaks corresponding to the transient variation of diffracted intensities $\Delta I_{hkl}(t)/I^0_{hkl}$.

By presenting the experimental results in this fashion, and with the knowledge of the unit cell dimensions from the literature ([104]), the Bragg peaks corresponding to the transient variation of diffracted intensities $\Delta I_{Ihkl}(t)/I^0_{hkl}$ can be easily identified.

The possibility of a modification in the structure of ferroelectric ammonium sulphate during the photoexcitation period was considered. However, given the fact that, within experimental accuracy, there is no variation in the angular position of the diffraction peaks, and no new additional Bragg peaks forbidden by space group symmetry are observed, it was concluded that the ferroelectric lattice geometry is conserved throughout all the experiment time.

4.4 Improvement of the Signal-To-Noise Ratio in measurements

The experimental set-up characteristic *photon statistics* and *noise* sources have been described previously elsewhere ([25, 172, 173]). In general, noise can be defined as the random signal fluctuations that are not correlated in any fashion with the physical quantity that is being measured. At the base of noise sources in this experimental set-up lie different fluctuations on several time scales, e.g., mechanical instabilities in the X-Ray source, efficiency of the X-Ray detection, temporal fluctuations of the driver laser with a shot-to-shot peak energy fluctuation of ∼0.3%, etc ([169, 170]).

Even if some of these noise sources can be somewhat mitigated, there exists a fundamental limit to the precision with which a signal can be measured: the so-called *shot or Poisson noise*. It is associated to the electronic detection of X-Ray photons in the Dectris X-Ray camera ([190–192]). Shot noise is defined as the statistical error of a Poisson distribution, that characterizes the occurrence of random events independent of each other, and describes the process of photon counting by the detector (Sec.4.1.3 and Fig. 4.5). In this sense, it is shot noise which ultimately limits the sensitivity of the experiment, i.e., it determines the smallest variation of diffracted intensity that can be measured ([25]):

$$\Delta I/I_0 \quad = \quad (I - I_0)/I_0 \quad = \quad 1/\sqrt{< N >}$$

where I and I_0 correspond to the diffracted intensity with and without photoexcitation, respectively, and <N> corresponds to the average number of detected photons. The Poisson distribution is characterized by having a signal-to-noise ratio of:

$$SNR^{PoissonDistribution} \quad = \quad \sqrt{< N >},$$

Given the low flux that the X-Ray source procures, it is necessary to accumulate experimental data over a number of days to improve the statistics of the system and achieve a significant Signal-to-Noise ratio, i.e., make the system sensitive to small variations in the Bragg peaks diffracted intensity.

As previously introduced, an efficient averaging methodology has been developed to to reduce the statistical error and mitigate the influence of most of the temporal fluctuations ([172]). This concept is described in Figure 4.1 and, essentially, consists of the pump beam being mechanically chopped at a 12.5Hz-readout rate in the Dectris camera while the pump-unpump cycle is monitored with the help of a photodiode reading from a leakage in the 400nm optical pump. With this knowledge, the variation of diffracted intensity accumulated in subsequent 40ms-time blocks from the pump/unpumped sample can be directly derived. This method succesfully improves the signal-to-noise ratio where, under optimal conditions, the system reaches the shot noise precision limit mentioned beforehand ([26]). This allows for the determination of the absolute variations of X-Ray diffracted intensity with a sensitivity in the order of $\Delta I/I \sim 10^{-3}$ ($\sim 1\%$) for the usual accumulated experiment times, as presented in the exemplary transients in Figure 4.14.

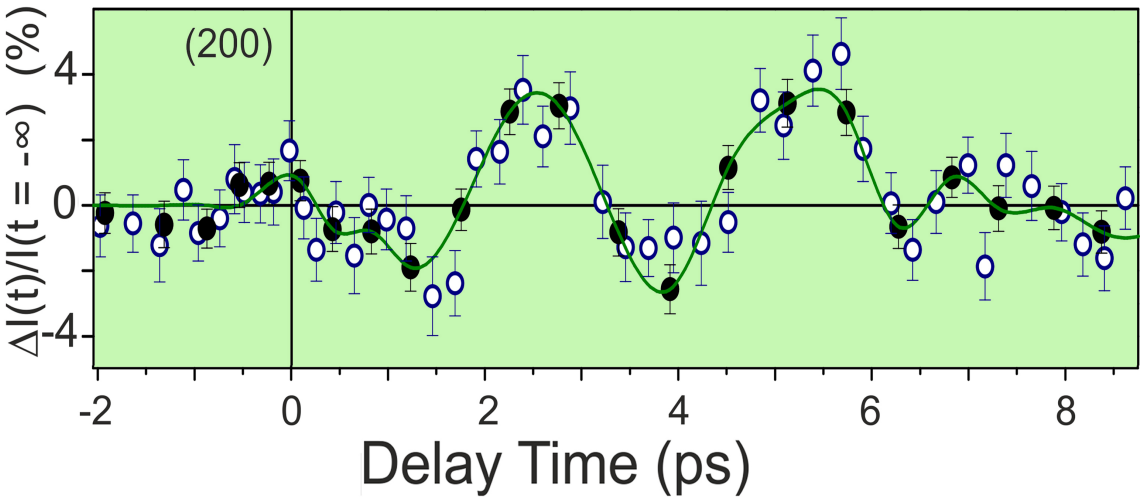

Figure 4.14: The black-symbol curve is obtained by averaging 40-neighbouring points together, and it is characterized by a time resolution of ∼400 fs and Error Bars of ∼ 1.4%. The white-symbol curve is obtained by averaging 20-neighbouring points together which yields a comparatively better time resolution of ∼ 200 fs but larger Error Bars ∼2%.

Averaging the raw data with a reduced bin size, resulting in twice the number of averaged data points, nicely retains the oscillatory signal as indicated by the light gray points in Fig. 2(c). There are no significant additional high frequency components in the transients with a reduced bin size.

The next step consists in deciding what is the most appropriate time binning for the raw data points that yields a faithful reconstruction of the transient variation of diffracted intensity. The entire experimental data set analysed in this work was gathered in over 10 days of experiments. It consists of approximately 1000 *time-delay measurements* collected within a 12ps-time interval at random ∼10 fs of in-between time spacing. To extract meaningful physical insight from the data, it is necessary to obtain transients with an acceptable signal-to-noise ratio, i.e., transients with statistical error bars which are reasonably small in comparison to the observed intensity variations. In general, a trade-off between the size of the error bars and the experimental time resolution is necessary. In this sense, the best solution

of compromise is obtained when, firstly, all collected individual data points are sorted according to their time delay and, subsequently, sets of 40 neighbouring points are averaged together, thereby yielding a time resolution of ∼400 fs and Error Bars ∼1.4%. All final experimental transient measurements accomplished in this work have been averaged in this fashion and are presented in the figures Fig. 5.2, Fig. 5.3, and Fig. 5.4.

To better illustrate this situation, a comparison of two different averaging possibilities for the same reference transient measurement in the diffraction peak (200) are represented in Figure 4.14. The black-symbols curve corresponds to the aforementioned 40-points averaging method, which yields a time resolution ∼400 fs and Error Bars of ∼1.4%, and the white-symbols curve corresponds to a 20-points averaging, which yields a time resolution of ∼200 fs and Error Bars of ∼2%. The graph shows how the white-symbols curve presents less averaging and, correspondingly, larger error bars than the black-symbols curve. Both curves match quite well which suggests that the transient does not contain oscillations with higher frequencies, being this a trend that has also been observed in all of the other measured transients.

4.5 Maximum Entropy Method

In this thesis, the electron density is reconstructed in an iterative manner by a recursive formalism called Maximum Entropy Method (MEM) ([150, 152, 153]). It was originally designed as an *information–theory-based technique* to improve noisy data in the field of radioastronomy, but since then it has become a powerful tool, which is fruitfully used for image reconstruction in many fields of science, e.g., reconstruction of electron-density maps based on X-Ray diffraction or nuclear-density maps based on neutron diffraction. The methodology used to apply the Maximum Entropy Method and generate electron density maps from the collected data in this experiment is discussed in detail in the following section.

4.5.1 Spatial Resolution Correction in the reconstruction of the transient electron density $\rho(\mathbf{r},t)$

The number of accessible diffraction peaks in the experimental set-up is constrained by the surface of the large-area Dectris Pilatus 1M X-Ray camera, which imposes an upper limit to the scattering angle that can be measured, $2\Theta_{max}$, and corresponds to a maximum scattering vector of $q_{max} = \sin(\Theta_{max})/\lambda_{X-Ray}^{Cu-K_\alpha}$. For the particular geometry of the experiment, the numerical value for the maximum scattering vector is $q_{max} = 0.2543\text{nm}^{-1}$ and, henceforth, according to the definition provided in Eq. 3.5, only the structure factors, $\mathbf{F}_{hkl}$, associated to scattering vectors, $\mathbf{q}_{hkl}$, that comply with the condition $|\mathbf{q}_{hkl}| < q_{max} = 0.2543\text{nm}^{-1}$ are accessible.

The Maximum Entropy Method (MEM) directly allows for the reconstruction of the transient charge density maps from the experimentally observed structure factors, $\mathbf{F}_{hkl}^{OBS}(t)$, without involving a particular pre-determined model. Another advantage is that, in contrast to the widely extended least-squares methods, MEM permits to fix an arbitrarily small difference between the estimated structure factors, $\mathbf{F}_{hkl}^{MEM}(t)$ $|\mathbf{q}_{hkl}| > q_{max} = 0.2543 nm^{-1}$, i.e., between the added unknown information and the experimentally observed Structure Factors: $|\mathbf{F}_{hkl}^{OBS}(t) - \mathbf{F}_{hkl}^{MEM}(t)| \ll |\mathbf{F}_{hkl}^{OBS}(t)|$.

In the past, there has been some controversy about the correct application of the MEM approximation due to claims of spatial *super-resolution* ([204]), or on how the the calculation of non-nuclear maxima of $\rho(\mathbf{r})$ in silicon was accomplished ([205]). However, these and other problems have been circumvented here with the development of the methodology described in the reference [25].

When applying MEM, the quantity of unknown estimated data that needs to be added to complete the missing information that cannot be accessed due to the limitations in the set-up (i.e., $\mathbf{F_{hkl}}$ with $|\mathbf{q}_{hkl}| > q_{max}$) has to be much smaller than the collected data from the experiment in order to obtain a reconstruction of the charge density maps that is physically coherent. However, if the MEM is directly applied to the experimental transient structure factors ($\mathbf{F}_{hkl}^{OBS}$, $|\mathbf{q}_{hkl}| < q_{max}$), it would generate an unreliable charge density reconstruction because in this case, the amount of forecast information estimated by the MEM ($\mathbf{F}_{hkl}^{MEM}$) shall be larger than the actual data collected in the experiment ([25]).

The methodology followed to solve this problem, consists in artificially reducing the spatial resolution of the initial ground state density via multiplying its associated structure factors ($\mathbf{F}_{hkl}^{0}$) by the gaussian profile as described in the formula:

$$F_{\mathbf{hkl}}^{0\,RED} = F_{\mathbf{hkl}}^{0} \cdot exp\{-ln(2) \cdot (\mathbf{q}_{hkl}/q_{max})^2\} \tag{4.1}$$

where $F_{hkl}^{0\,RED}$ is defined as the *static or ground state reduced structure factor*.

Once the spatial resolution corresponding to the observed structure factors is reduced, The application of MEM is possible, given that the possibility of an artificial enhancement of the charge density maps is canceled. Therefore, this curtails the appearance of spurious artifacts due to the so-called *Gibbs phenomenon* that otherwise would surge if the direct Fourier transform was applied instead of the MEM methodology ([206]). In this sense, the Gibbs phenomenon consists of the appearance of ring-like structures surrounding the atoms in the charge density maps when using the direct Fourier transform owing to the so-called *series truncation error* that is caused by the abrupt end of the Fourier series whose terms are cut-off at q_{max} given the impossibility to access the structure factors beyond the range $|\mathbf{q}_{hkl}| < q_{max}$.

Notwithstanding, if it was attempted to further reduce the spatial resolution, for example, by using a higher spatial-resolution reducing factor such as in the expression:

$$F_{\mathbf{hkl}}^{0\,RED*} = F_{\mathbf{hkl}}^{OBS} \cdot exp\{-ln(2) \cdot (2\mathbf{q}_{hkl}/q_{max})^2\}$$

then, the MEM calculations would present an almost vanishing difference from the direct Fourier transform in the truncated reciprocal space, i.e., $\mathbf{F}_{hkl} \approx 0$ for $|\mathbf{q}_{hkl}| > q_{max}$, thus, rending the MEM unusable. The expression in Eq. 4.1 has been proven to be an acceptable compromise solution to this problem ([25]).

In Figure 4.15, the amplitude of the static structure factors for ferroelectric ammonium sulphate ($|F_{hkl}^0|$), the gaussian spatial-resolution reduction factor ($exp\{-ln(2) \cdot (\mathbf{q}_{hkl}/q_{max})^2\}$), and the reduced static structure factors ($F_{hkl}^{0\,RED}$) are plotted as a function of the amplitude of the scattering vector ($|\mathbf{q}| = \sin(\Theta)/\lambda_{X-Ray}$). The maximum scattering vector $q_{max} = \sin(\Theta_{max})/\lambda_{X-Ray} = 0.2543 nm^{-1}$ indicates the upper limit for the accessible Bragg peaks in the experimental set-up.

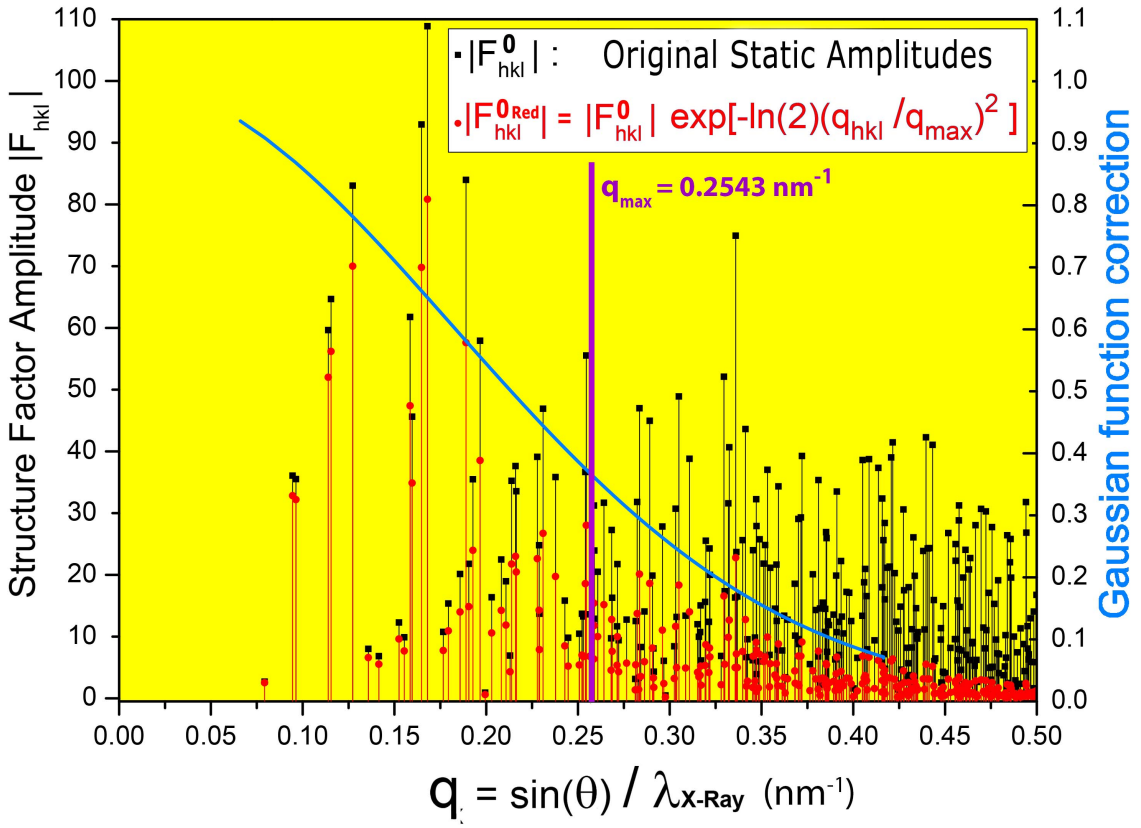

Figure 4.15: Illustrative representation for the original and reduced static structure factors for ferroelectric ammonium sulphate. Here are shown the amplitude of the original static structure factors (black dots), the Gaussian function with which the original amplitudes are corrected (in blue, with scale on the right), and the reduced static structure factors (red dots). In purple, it is marked the modulus of the maximum scattering vector ($q_{max} = 0.2543 nm^{-1}$) that can be accessed in the experimental set-up.

In conclusion, the MEM permits the reconstruction of transient charge density maps from an incomplete data set of structure factors indirectly derived from the experimental transient variation of

diffracted intensity in the different Bragg peaks, $\Delta I_{Ihkl}(t)/I^0_{hkl}$. As mentioned, this methodology avoids the appearance of artefacts, permits a proper assessment of the MEM results, and has already been successfully applied in the reconstruction of the transient charge density maps of $NaBH_4$, LiH, and $LiBH_4$ ([26, 151]). In the following, a description of the mathematical framework behind the Maximum Entropy Method is given.

4.5.2 The Mathematics of Entropy Maximization

The theory is formally based on the same equations at the foundation of statistical physics, where a mathematical quantity named *information entropy*, is defined in analogy to the statistical entropy. In statistical physics, the most *probable distribution* in a system exists in the particle and momentum spaces, while in the information theory, the most probable distribution deals in numerical quantities that spread over the ensemble of a set of elements (usually surface elements called *pixels* or volumetric elements called *voxels*). In this sense, the most probable distribution is derived by maximizing the information entropy.

This discussion of the mathematics of the Maximum Entropy Method follows closely the analysis of P. Coppens in Ref.[207]. Coppens starts by defining the entropy of a system of N identical particles separated over m different boxes, each of which is populated by n_i particles, where the probability of obtaining a certain distribution of N identical particles is given by:

$$P = \frac{N!}{n_1!\, n_2! \cdot .... \cdot n_m!} \tag{4.2}$$

It bears mentioning that this is a simplified case, since typically the most general definition includes the sum of population probabilities for any system, not only for a system with N identical particles over m boxes. Taking into account Eq. 4.2, and by basing on the fact that both statistical and information entropies are defined as:

$$S = ln\, P$$

with which the entropy, apart from a constant, can be expressed as:

$$S = -\sum_i n_i \cdot ln\, n_i \tag{4.3}$$

It was E. T. Jaynes who in his remarkable scientific paper from 1957, *Information theory and statistical mechanics entropy* ([208]), introduced the concept of *maximum entropy estimate* as being a type of statistical inference based on an information theory that provides a criterion for constructing probability distributions on the basis of an initial partial knowledge, i.e., an initial solution that he called *prior*

information. Later in 1968, Jaynes would expand his theory, and define accurately the information entropy with an a-priori distribution ([209]).

If the initial distribution solution for the system is known, i.e., *prior probability*, then Eq. 4.2 converts to:

$$P = \frac{N!}{n_1!\, n_2! \cdot .... \cdot n_m!} \cdot q_1^{n_1} \cdot q_2^{n_2} \cdot ... q_m^{n_m} \tag{4.4}$$

where q_i is the prior probability for the box number i to contain n_i particles. In this situation, the expression for the information entropy becomes:

$$S = -\sum_i n_i \cdot ln\, n_i + \sum_i n_i \cdot ln\, q_i = -\sum_{i=1}^{m} n_i \cdot ln\, \frac{n_i}{q_i} \tag{4.5}$$

Jaynes himself described the estimation of the probability distributions as *'the least biased possible'*, presenting the MEM methodology as the best that provided an estimation that is *'maximally non-committal with regard to missing information'* ([208]). Later on, it was Collins who introduced the Maximum Entropy Method (MEM) for the first time in the field of crystallography in 1982 ([204]) by expressing the information entropy of the electronic distribution ($S[\rho(\mathbf{r})]$) as a sum over N_{VOX} grid points or subdivisions in the unit cell, called *voxels*. This concept shall be discussed further in Section 4.6.

$$S[\rho(\mathbf{r})] = -\sum_{j=1}^{N_{VOX}} p(r_j) \cdot ln\, \frac{p(r_j)}{m(r_j)} \tag{4.6}$$

where $p(r_j)$ and $m(r_j)$ are fractional quantities defined as:

$$p_j = p(r_j) = \frac{\rho(r_j)}{\sum_{j=1}^{N_{VOX}} \rho(r_j)} \tag{4.7}$$

and

$$m_j = m(r_j) = \frac{\rho_0(r_j)}{\sum_{j=1}^{N_{VOX}} \rho_0(r_j)} \tag{4.8}$$

and where the subscript zero refers to the prior density. It also bears mentioning that $p(r_j)$ and $m(r_j)$ are proportional, respectively, to the probability and to the prior probability of finding an electron at position r_j.

Once arrived at this point, the procedure specifies that the entropy, S[$\rho(\mathbf{r})$] (Eq. 4.6), must be maximized iteratively until a pre-defined convergence value (i.e., allowed error) is reached while subject to a certain constraint that is associated to the prior distribution:

$$C[\rho(\mathbf{r})] = \chi^2 = \sum_{k=1}^{N} \left| \frac{F_k^{OBS}(H) - F_k^{MEM}(H)}{\sigma(F_k^{OBS}(H))} \right|^2 = N \tag{4.9}$$

where N corresponds to the number of experimentally observed structure factors, F_k^{OBS}(H) corresponds to the observed structure factors, F_k^{MEM}(H) corresponds to the structure factors calculated by MEM for the current estimated charge density, ρ, and $\sigma(F_k^{OBS}(\mathrm{H}))$ is the standard error of F_k^{OBS}(H). F_k^{MEM}(H) is obtained by summation over the N_{VOX} voxels (or grid points) in the following fashion:

$$F_k^{MEM}(H) = \frac{\Omega_{UC}}{N_{VOX}} \sum_{j=1}^{N_{VOX}} \rho(r_j) exp\{2\pi i H_k \cdot r_j\} \tag{4.10}$$

while a suitable scaling must be applied to F_k^{OBS}(H).

Without the constraint from Eq. 4.9 maximizing the entropy, MEM would simply produce an uniform distribution all over the space, which is also known in the context of MEM as *flat distribution*.

The maximization of entropy, under that previously mentioned constraint, is enforced with the help of a Lagrange multiplier λ introduced in the minimization function:

$$L(\lambda) = S[\rho(\mathbf{r})] - \lambda\chi^2 \tag{4.11}$$

This implies that once the convergence is reached, the gradient of the minimization function will be equal to zero:

$$\nabla_\rho L(\lambda) = \nabla_\rho (S[\rho(\mathbf{r})]) - \lambda \nabla_\rho (\chi^2) = 0 \tag{4.12}$$

which for each voxel (or grid point) j, corresponds to:

$$\frac{\partial S[\rho(\mathbf{r})]}{\partial \rho_j} = \lambda \frac{\partial \chi^2}{\rho_j} \tag{4.13}$$

An essential issue to be taken into account here is that, the entropy-maximization algorithm is non-linear and, therefore, it must be re-calculated iteratively. Finally, by following the procedures described in the references [210] and [207], it is obtained that $\rho(r_j, n+1)$, i.e., the density distribution at r_j for the iteration $(n+1)^{th}$, is given by the expression:

$$\rho(r_j, n+1) = \\ = exp\left\{ ln \sum_j p_j \, ln \, \rho_j(n) + \lambda \cdot F(0) \cdot \sum_H \frac{2}{\sigma(H)^2} exp\{2\pi i H \cdot r_j\} \cdot \left| F_k^{OBS}(H) - F_k^{MEM}(H) \right| \right\} \quad (4.14)$$

where:

$$F(0) = \frac{\Omega_{UC}}{N_{VOX}} \sum_{j=1}^{N_{VOX}} \rho(r_j) \quad (4.15)$$

It can be seen that, by starting from the values of $\lambda(n)$ and $\rho_j(n)$, one can solve $\lambda(n+1)$ and $\rho_j(n+1)$ at each n-iteration. The initial values for the iterative process, if these exist, are $\lambda(0) \approx 0$ and $\rho_j(0)$, which correspond to the prior distribution. The procedure to reach convergence involves a two-step process in which, firstly, the constraint $\chi^2 = N$ is satisfied, and secondly, the entropy S is maximized.

Summary of the MEM procedure

A practical summary for the the MEM procedure is given in Fig. 4.16. It can be said that the Maximum Entropy Method estimates the charge density maps, i.e., the most probable electronic density distributions from the experimentally obtained instantaneous structure factors, $F^{OBS}(H)(t)$, by maximizing the information entropy associated to a volume that is discretized in a certain number of voxels N_{VOX}, each of which has associated a certain charge density distribution ρ_i.

In particular, the expression for the information entropy is given by $S = -\sum_{i=1}^{N_{VOX}} \rho_i(t) \cdot \ln[\rho_i(\mathbf{r}, t)/\rho_{0i}(\mathbf{r})]$, where ρ_{0i} corresponds to the electronic density distribution associated to the i-voxel in the unexcited sample, $\rho_i(t)$ corresponds to the electronic density distribution associated to the i-voxel in the photo-excited sample, and the summation runs over the N_{VOX} voxels.

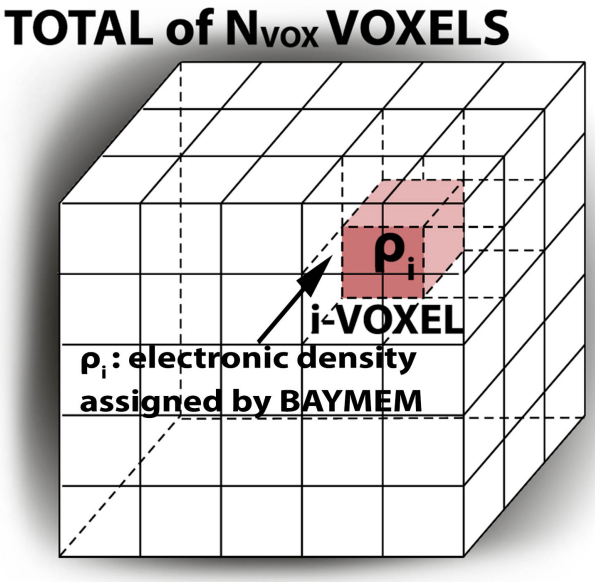

MAXIMIZE INFORMATION ENTROPY

$$S = - \sum_{j=1}^{N_{vox}} \rho_i(t) \cdot \ln[\rho_i(\mathbf{r}, t)/\rho_{0i}(\mathbf{r})]$$

MINIMIZE CONSTRAINT

$$C[\rho(\mathbf{r})] = \chi^2 = \sum_{k=1}^{N} \left| \frac{F_k^{OBS}(H) - F_k^{MEM}(H)}{\sigma(F_k^{OBS}(H))} \right|^2 = N$$

Figure 4.16: Schematic summary for the MEM procedure. The electronic density distribution is calculated by maximizing the information entropy, S, where ρ_{0i} corresponds to the electronic density distribution associated to the i-voxel in the unexcited sample, ρ_i(t) corresponds to the electronic density distribution associated to the i-voxel in the photo-excited sample, and the summation runs over the N_{VOX} voxels. At the same time, the constraint must be fulfilled, where *N* corresponds to the number of experimentally observed structure factors, F_k^{OBS}(H) corresponds to the observed k-structure factor, F_k^{MEM}(H) corresponds to the k-structure factor calculated by MEM for the current estimated charge density, ρ, and $\sigma(F_k^{OBS}(H))$ is the standard error for the structure factor F_k^{OBS}(H)

The MEM must equally fulfill certain constraints that are related to the ground state structure factors and to the experimentally obtained instantaneous structure factors. The more relevant constraint is:

$$C[\rho(\mathbf{r})] = \chi^2 = \sum_{k=1}^{N} \left| \frac{F_k^{OBS}(H) - F_k^{MEM}(H)}{\sigma(F_k^{OBS}(H))} \right|^2 = N \tag{4.16}$$

where *N* corresponds to the number of experimentally observed structure factors, F_k^{OBS}(H) corresponds to the k-observed structure factor, F_k^{MEM}(H) corresponds to the k-structure factor calculated by MEM for the current estimated charge density, ρ, and $\sigma(F_k^{OBS}(H))$ is the standard error for the k-structure factor F_k^{OBS}(H).

The crystallographic software application that actually implements the Maximum Entropy Method is called BayMEM, and shall be described with detail in the following section.

4.6 BayMEM Software

The methodology used to derive the transient charge density by means of the BayMEM software is summarized here, while a full description is given in the Appendix 5.6. BayMEM is a suite of programs for academic research that was developed in the Laboratory of Crystallography of Prof. Dr. Sander van Smaalent in 2005 ([211]). In particular, BayMEM implements the algorithm developped by Sakata and Sato ([205]). It is based on the approximations of Collins ([204]), while the λ-parameter is permanently kept fixed at a small value that makes it suitable to ensure convergence.

Figure 4.17 summarizes how the BayMEM software generates transient electronic density maps from two sets of data inputs. One of them is the measured variation of diffracted intensity, and the other one is the resolution-reduced *prior distribution* (in this sense, prior distribution is conceptually equivalent to initial solution). The reason for the necessity of reduction of resolution, as previously commented in Section 4.5.1, is to avoid the appearance of artifacts due to Gibbs phenomenon ([206]).

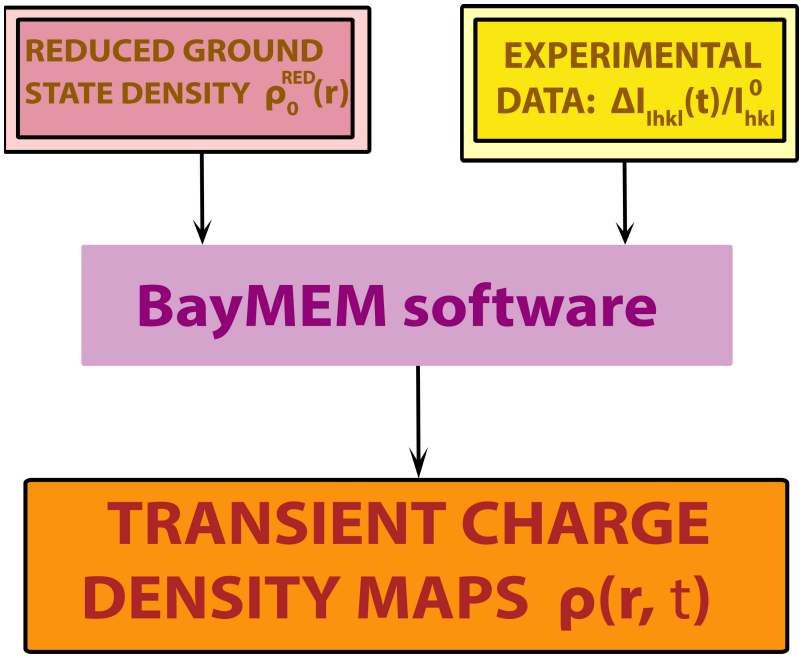

Figure 4.17: The schematic describes, in a general fashion, the process of deriving the transient charge density, $\rho(\mathbf{r}, t)$, from the resolution-reduced ground state density, $\rho_0^{RED}(\mathbf{r})$, and the measured variations of diffracted intensity in the different Bragg peaks, $\Delta I_{Ihkl}(t)/I^0_{hkl}$.

Here, the general features of BayMEM are introduced, whereas its actual operational algorithm is detailed in Section 3.6.

One of the crucial features of the MEM theory indicates the necessity of a proper subdivision of the unit cell in smaller polyhedra to facilitate the calculations of the BayMEM software. The key concept is the so-called *voxel* that consists of an element in a three-dimensional grid with an integer

numerical value associated for its electronic charge density, and with which its volumetric display can be represented. The number of voxels is given by the expression $N_{voxel} = N_a \times N_b \times N_c$ where N_a, N_b and N_c, correspond to the number of divisions for the x-, y- and z-axes, respectively. The main rules that set the number of voxels are presented here briefly, while a full description has been given in the Appendix (App.Sec. 5.6, and [212]).

These rules can be conceptually divided into two different groups: certain rules are compulsory, and certain others are recommendations which, if not followed, will increase the computing time or directly make the calculation impossible for time-consuming reasons. One of the compulsory rules states that the division into voxels must obey the symmetry of the unit cell, i.e., a center of any voxel must be mapped by the symmetry operators onto itself or onto the center of some other voxel. This means that, for example, if for a certain crystal, one of the directions has the screw axis set of symmetries 2_1, 3_1, 4_1, 6_1 or 6_2, then the number of voxels along that direction must be a multiple of 2, 3, 4, 6 or 3, respectively. In the case of ferroelectric ammonium sulphate, which corresponds to the space group $Pna2_1$, the number of N_C divisions along the c-direction must be a multiple of 2.

In the following, the group of non-compulsory rules are mentioned. The first one states that numbers with small prime factors are preferred, since this permits to take full advantage of the speed of the fast Fourier transform. A second and third non-compulsory rule state that, combinations of powers of the numbers two or three are especially favourable, and that the largest prime factor of all the divisions must be smaller than 23.

There is one last condition to be met, i.e., the number of voxels must be large enough, that the resolution attained in the experimental set-up is not artificially degraded due to a too coarse division of the unit cell. This imposes the constraint that the ratio of the number of sub-division along the different axes in the unit cell, must be equal to the ratio of the different lattice factors, which ultimately results in cuboid voxels. For the case of ferroelectric ammonium sulphate the side length of the cuboids are ideally around $\sim 0.1\mathring{A}$.

Since all these diverse rules have to be accounted for to avoid large computation times when deriving transient charge distributions with BayMEM, in general, a solution of compromise for the number of subdivisions in the unit cell is set. E.g., for the case of the ferroelectric ammonium sulphate, the optimal division number is: $N_{voxel} = N_a \times N_b \times N_c = 72 \times 108 \times 64 = 528.768$ voxels.

BayMEM Methodology

It bears reminding that, as previously introduced, since the X-ray photons mostly interact only with the electrons, it is the electronic charge dynamics that shall be derived from the experimentally measured transient variations of diffracted X-ray intensity. The methodology to derive transient charge density maps by means of the BayMEM software is briefly introduced here (Fig. 4.18), whereas a full description is given in the Appendix 5.6. Generally speaking, the methodology consists of two differentiated stages:

- **Stage one**: derivation of the resolution-reduced static prior distribution, $\rho_0^{RED}(\mathbf{r})$.
  The BAYMEM software generates the resolution-reduced static (or ground state) charge density (i.e., initial solution or prior distribution), ρ_0^{RED}, by taking as inputs the so-called *flat prior distribution* (initial distribution with highest possible entropy) and the resolution-reduced static structure factors (previously described in detail in Section 4.6).

- **Stage two**: derivation of the resolution-reduced transient electronic charge density, $\rho_0^{RED}(\mathbf{r}, t)$.
  The BayMEM software generates the resolution-reduced transient electronic charge density by taking as inputs the resolution-reduced static prior distribution, ρ_0^{RED}, and the resolution-reduced transient structure factors, $F_{\mathbf{hkl}}^{RED}(t)$ ([152, 211], and described in detail in Section 4.5.1).

Stage One: Derivation of resolution-reduced static prior charge density, ρ_0^{RED}

In the first stage, the BayMEM software derives the resolution-reduced static charge density from $F_{\mathbf{hkl}}^{0\,RED}$ and the so-called flat prior distribution.

STEP 1:

The starting point is the *CIF file* of the studied crystalline material. A CIF file consists of a particular research-dedicated standard text file that contains the relevant crystallographic information for the unexcited material. In the case described in this work, the CIF file for the ferroelectric ammonium sulphate is loaded in the crystallographic JANA software (2006) which, in turn, generates the list of calculated static structure factors, $F_{\mathbf{hkl}}^{0}$, along with other crystallographic information. Subsequently, the list of structure factors is selected and the structure factors are resolution-reduced as described in Section 4.5.1, according to expression:

$$F_{\mathbf{hkl}}^{0\,RED} = F_{\mathbf{hkl}}^{0} \cdot exp\{-ln(2) \cdot (\mathbf{q_{hkl}}/q_{max})^2\} \tag{4.17}$$

STEP 2:

BayMEM software calculates the static charge density, $\rho_0^{RED}(\mathbf{r})$, from two inputs: the previously obtained list of reduced static structure factors, $F_{\mathbf{hkl}}^{0\,RED}$ (Eq. 4.17), and the so-called *'flat prior distribution'*, $\rho_0^{FLAT}(\mathbf{r})$. The name flat prior distribution comes from the fact that it corresponds to a homogeneous distribution over all of the space, i.e., a distribution characterized by having the highest possible entropy. The flat prior distribution shall be constructed artificially by dividing the number of electrons in the unit cell by its associated number of voxels, with which every voxel will be populated with the according fraction of electrons/voxel.

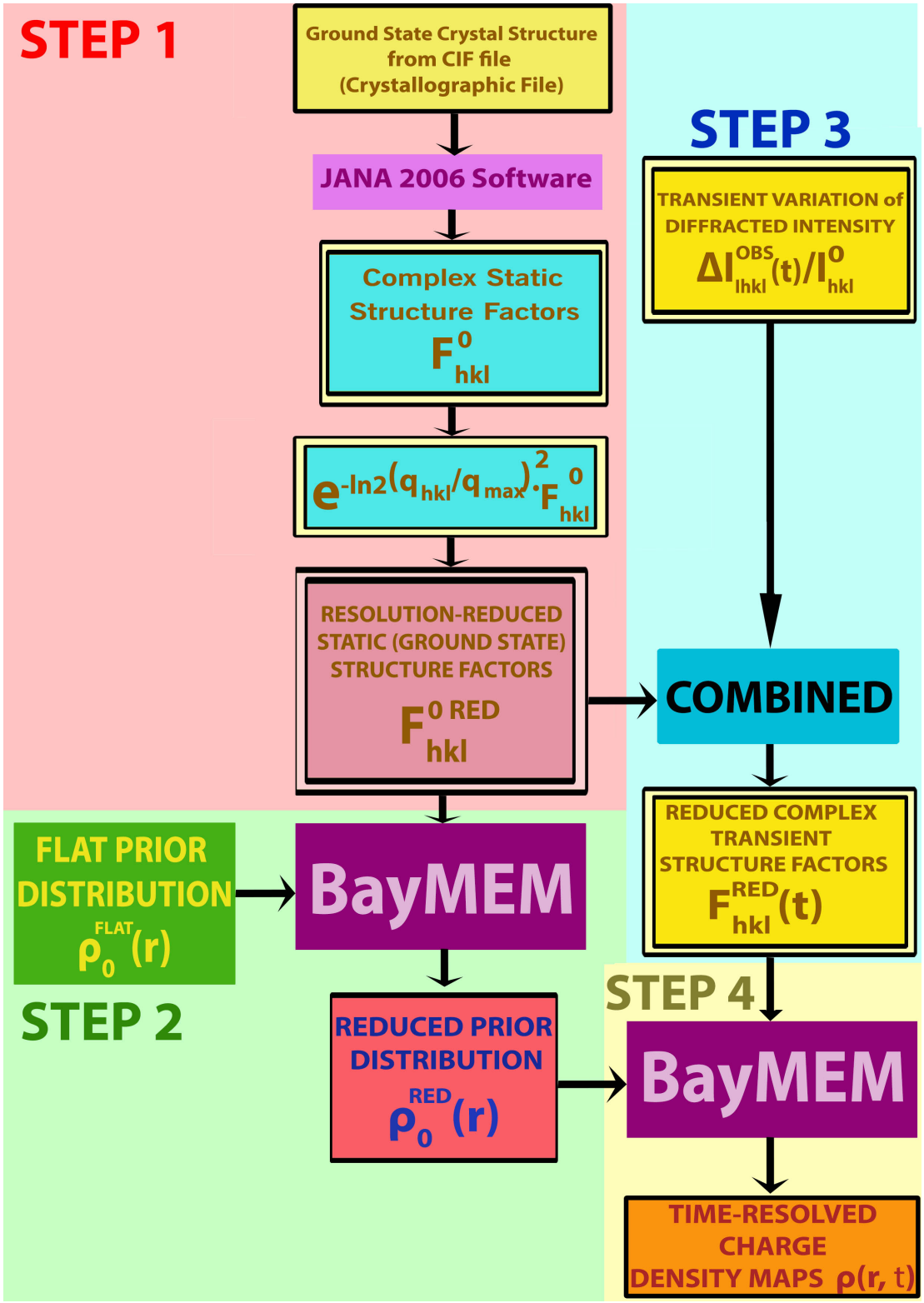

Figure 4.18: Algorithm for the derivation of the electronic charge dynamics with BAYMEM. Fundamentally, it consists, of two stages. In the first stage (steps 1 and 2), BAYMEM generates the resolution-reduced static charge density, $\rho_0^{RED}(\mathbf{r})$, by taking the *flat prior distribution* and the resolution-reduced static structure factors as inputs. In the second stage (steps 3 and 4), BayMEM generates the resolution-reduced transient electronic charge density, $\rho(\mathbf{r}, t)$, by taking the resolution-reduced static prior distribution, $\rho_0^{RED}(\mathbf{r})$, and the resolution-reduced transient structure factors, $F^{RED}_{\mathbf{hkl}}(t)$, as inputs.

Stage Two: Derivation of the transient electronic charge density, ρ(r, t)

STEP 3:

Once obtained the $\rho_0^{RED}(\mathbf{r})$, follows the calculation of the transient reduced structure factors, $F_{\mathbf{hkl}}^{RED}(t)$, from the measured transient variation of diffracted intensity in the Bragg peaks.

For this, the transient structure factors have to be derived from the measured variations of diffracted intensity (already explained in Section 3.6), where the spatial resolution of the transient structure factors must be previously reduced (explained in Sec. 4.5.1):

$$F_{\mathbf{hkl}}^{RED}(t) = F_{\mathbf{hkl}}(t) \cdot exp\{-ln(2) \cdot (\mathbf{q_{hkl}}/q_{max})^2\} \tag{4.18}$$

STEP 4:

In the last step, the BayMEM program is executed again, although this time taking as input the resolution-reduced static charge density, $\rho_0^{RED}(\mathbf{r})$, and the resolution-reduced structure factors at a certain instant t', $F_{\mathbf{hkl}}^{RED}(t')$, to generate the electronic charge density map $\rho^{RED}(\mathbf{r}, t')$, according to Eq. 4.18.

By repeating this process iteratively for the different instants t' in the experimental time range, the final transient electronic charge density is derived, $\rho(\mathbf{r}, t)$,

The methodology described here, allows for the derivation, in general, of the electronic charge dynamics in any photo-excited crystalline material. For the particular case of this work, it was applied to study ferroelectric ammonium sulphate and the results shall be discussed in the following chapter.

Chapter 5

Soft-mode driven polarity reversal in ferroelectric Ammonium Sulphate mapped by ultrafast X-Ray Diffraction

In this chapter, the experimental measurements for the variation of X-Ray diffracted intensity in the different Bragg peaks for photoexcited ferroelectric ammonium sulphate are presented along with the derivation of its transient charge density maps. Subsequently, the structural, charge density and polarization dynamics extracted from the charge density maps are analysed. Finally, the physical insight and conclusions for the newly-discovered charge modulation with soft mode character is discussed.

5.1 Experimental Results

The diffraction pattern of unexcited ferroelectric ammonium sulphate is shown in Fig. 5.1 as it helps clarifying the experimental transient variation of X-Ray diffracted intensity in the different Bragg peaks, $\Delta I_{Ihkl}(t)/I^0_{hkl}$, presented in Figures: 5.2, 5.3, and 5.4.

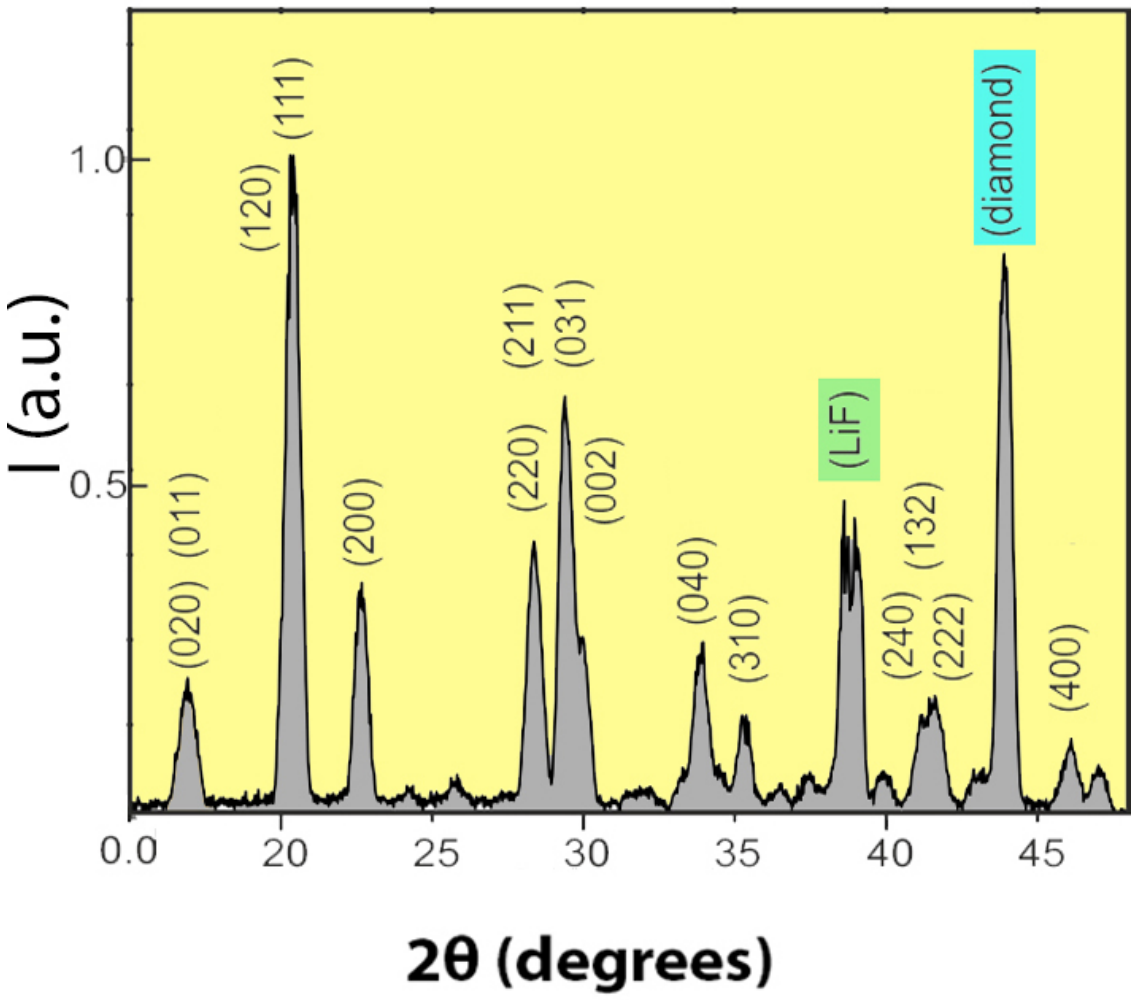

Figure 5.1: 2-Dimensional diffraction pattern integrated along the scattering angle 2Θ for ferroelectric ammonium sulphate at T = 200K. The figure shows the Miller indexes identified for the Bragg peaks in the ferroelectric ammonium sulphate, and in the diamond and lithium fluoride windows.

Figure 5.2 shows a set of selected transients that portray the variation of X-Ray diffracted intensity, $\Delta I_{Ihkl}(t)/I^0_{hkl}$, against the pump-probe time delay upon 400nm excitation for the Bragg peaks (200), (310) and the overlapping (120)+(111).

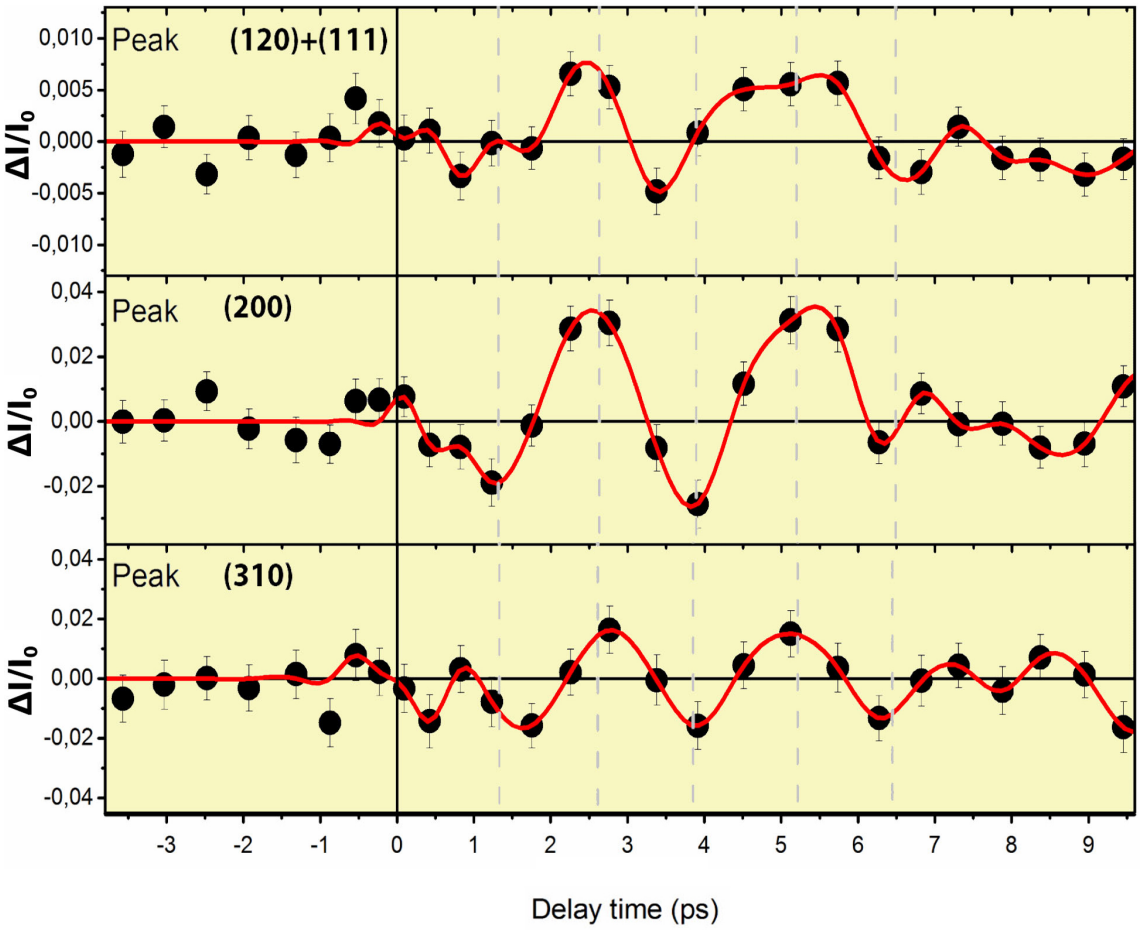

Figure 5.2: Selected set of transients portraying the variation of X-Ray diffracted intensity, $\Delta I_{Ihkl}(t)/I^0_{hkl}$, against the time delay upon 400nm pump excitation for the Bragg peaks (200) and (310), and the overlapping (120)+(111). The solid lines connecting the dots are guides to the eye.

Another selected set of experimental transients, this time with no significant changes in the variation of diffracted intensity, are given in Figure 5.3. As can be seen, not all the Bragg peaks have to necessarily undergo a change in the variation of diffracted intensity under the influence of the excitation pulse or, if they do, it can be so small that it may not be detected with the statistical significance achievable in this experiment's usual accumulated measuring times. In this context, the usual experiment time corresponds to the accumulation of approximately 1000 total transients, which yields a detection threshold of $\sim 1\%$ of the total diffracted signal. It bears mentioning that, even in this case, the results obtained are valuable information that contribute in the derivation of the transient charge density maps.

Analogous measurements of the variation of diffracted intensity were also conducted at the substantially lower temperature of 110K. An illustrative example comparing the experimental results at T = 200K and T = 110K for selected peaks is given in Figure 5.4.

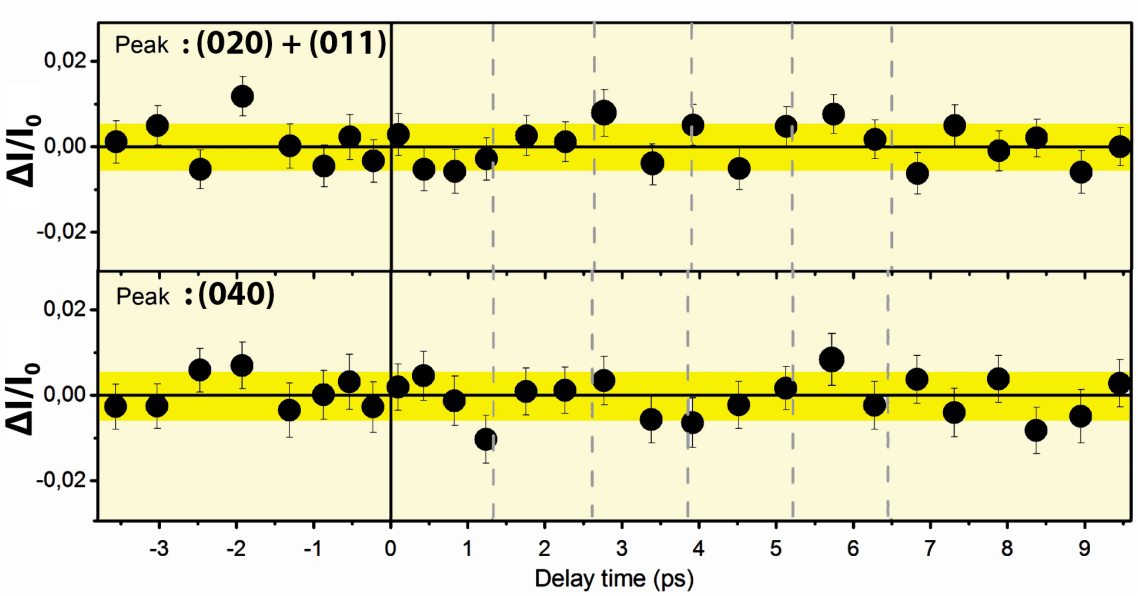

Figure 5.3: Selected set of transients portraying the variation of X-Ray diffracted intensity, $\Delta I_{Ihkl}(t)/I^0_{hkl}$, against the time delay upon 400nm pump excitation for the Bragg peaks (040) and the overlapping (020)+(011). The yellow region indicates the limit of the sensibility of this experimental set-up to variations of diffracted intensity for the experiment's usual measuring times, i.e., $\sim 1\%$. In this context, there is no statistically significant transient variation of X-Ray diffracted intensity for these Bragg peaks although this is valuable information that shall contribute to the derivation of the transient charge dynamics.

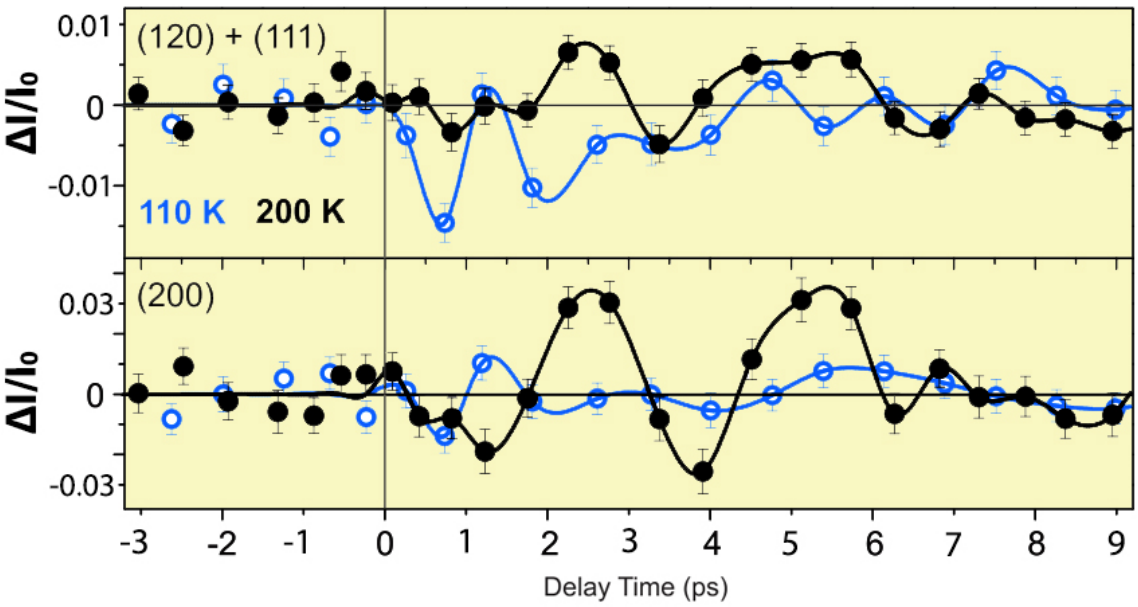

Figure 5.4: Selected set of transients portraying the variation of X-Ray diffracted intensity, $\Delta I_{Ihkl}(t)/I^0_{hkl}$, against the pump-probe time delay upon 400nm optical pump for the Bragg peaks (200) and the overlapping (120)+(111) at temperatures of T = 200K (black solid symbols) and T = 110K (blue open symbols). The solid lines connecting the dots are only guides to the eye.

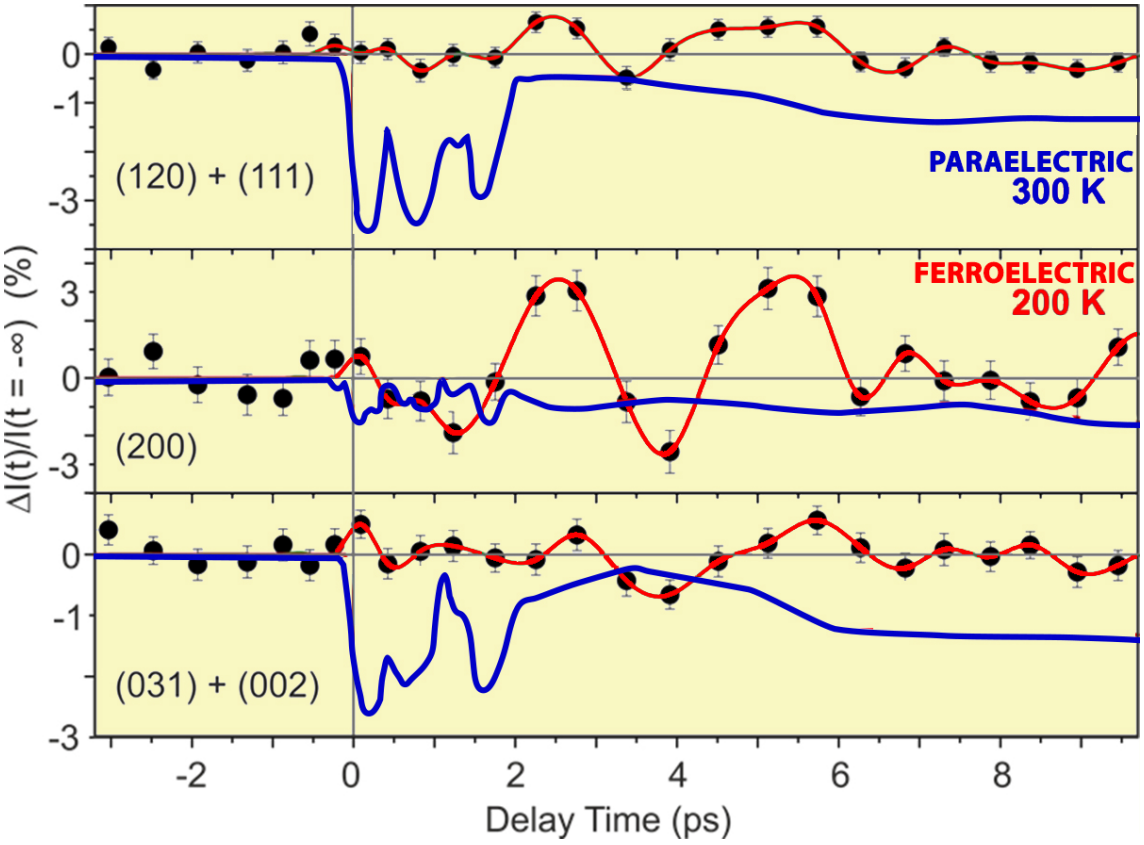

Figure 5.5: Selected set of transients portraying the variation of X-Ray diffracted intensity, $\Delta I_{Ihkl}(t)/I^0_{hkl}$, against the time delay upon 400nm pump excitation for para- and ferroelectric ammonium sulphate. Here are shown (200), and the overlapping (120)+(111) and (031)+(002) at T = 300K (room temperature) and T = 200K. The transients for ferroelectric ammonium sulphate are presented in black symbols with a red solid line as guide to the eye, while the transients for paraelectric ammonium sulphate from a previous experiment ([7]), are presented uniquely with a blue solid line to simplify the graphical comparison.

The results at 110K are significantly different from those accomplished at 200K. At T = 200K, the transients exhibit strong oscillations with a period of ∼3ps and a a somewhat delayed onset for the oscillations of ∼2-3ps, while at T = 110K, the transients present a fundamentally different behaviour with much more rapidly damped oscillations. This outcome suggests the existence of completely different lattice and charge dynamics that depend on the temperature even within the same ferroelectric crystallographic structure.

Finally, the Fig. 5.5 shows a set of selected transients where paraelectric ammonium sulphate at room temperature from a previous experiment ([7]) and the ferroelectric ammonium sulphate at 200K from the present experiment are compared. As can be seen, the transients of the paraelectric ammonium sulphate present a much faster and much sooner damped variations in X-Ray diffracted intensity compared with those of ferroelectric ammonium sulphate, which last for much larger time intervals. The lattice and charge dynamics, consequently, shall present a radically different behaviour, as can be expected for two different phases as para- and ferroelectric ammonium sulphate. For illustrative purposes, an actual comparison of the differences in charge and lattice dynamics for the photoexcited para- and ferroelectric state shall be presented in Section 5.2 .

5.2 Transient Charge Charge Density Maps for ferroelectric Ammonium Sulphate.

Equilibrium Structure and Static Charge Density Map for ferroelectric Ammonium Sulphate

Figure 5.6 shows the 3-dimensional representation of the ferroelectric ammonium sulphate unit cell. This structure is composed of two crystallographically different ammonium tetrahedra (NH_4^+) and sulphate tetrahedra (SO_4^{2-}), which are stacked in layers disposed perpendicularly to the crystallographic c-axis. The a-b lattice plane is highlighted at z = c/2, because it provides the best representation to study the charge dynamics. On top, its analysis can be reduced to the central region of that plane due to symmetry reasons, which is why the different contour maps in the following shall be represented as such. In this same sense, the four oxygen atoms compounding the sulphate anion are differentiated since these will present differentiated behaviours as shall be later discussed (e.g., Fig. 5.8).

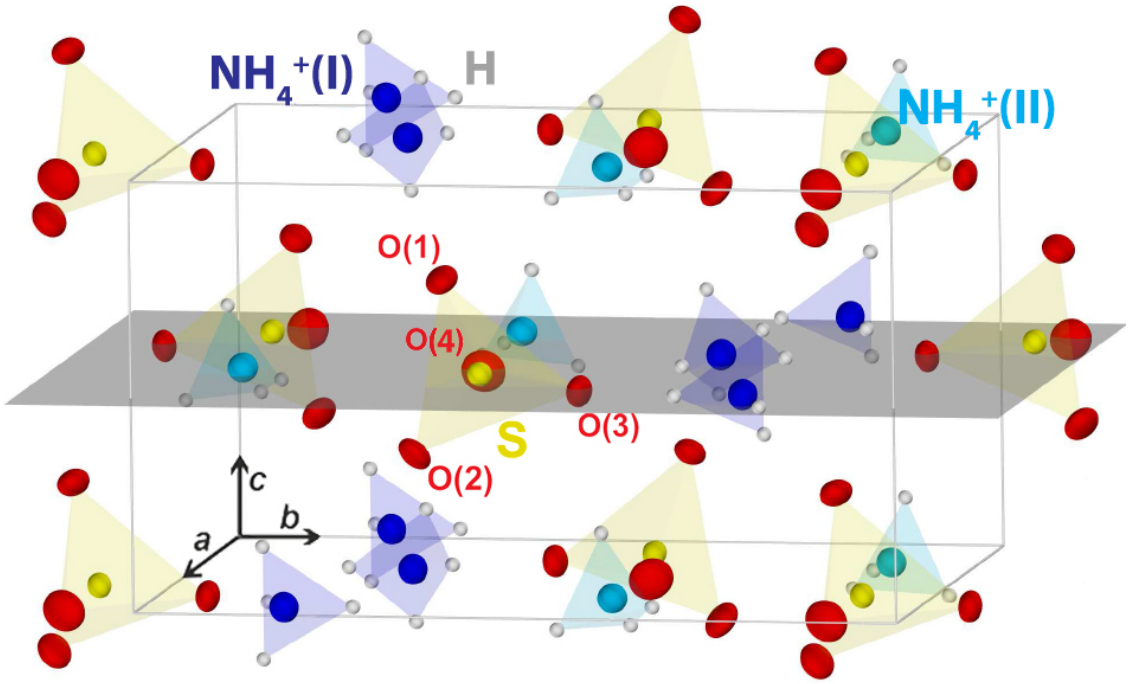

Figure 5.6: Equilibrium (i.e., unexcitated, static or ground state) crystal structure for ferroelectric ammonium sulphate as composed of two crystallographically different ammonium tetrahedra, NH_4^+, (light and dark blue) and sulphate tetrahedra, SO_4^{2-}, (yellow). The z = c/2 plane is highlighted in gray to help visualize the equilibrium charge density map presented in Fig. 5.7 and photophotoexcited charge density maps in Fig. 5.8. The four oxygen atoms in the sulphate anion are differentiated to help analyze the charge dynamics, since these present a distinct behaviour as shall be discussed in Fig. 5.8).

Fig. 5.7 shows the charge density map for unexcited ferroelectric ammonium sulphate, $\rho_0(\mathbf{r})$, that corresponds to the central section of the a-b lattice plane at z = c/2. For clarity, the locations of the two crystallographically different ammonium tetrahedra, NH_4^+(I) and NH_4^+(II), and of the sulphate tetrahedra, SO_4^{2-}, for the equilibrium crystal structure are displayed. The unexcited charge density contour map was derived with the help of BayMEM from the previous knowledge of the structure of ammonium sulphate (Sec. 4.6). As shall be seen later, the crystal structure of the ferroelectric ammonium sulphate does not change when excited upon 400nm optical pump with which the transient charge density maps can be interpreted as translocations of charge density with relation to the original unexcited ferrelectric ammonium sulphate.

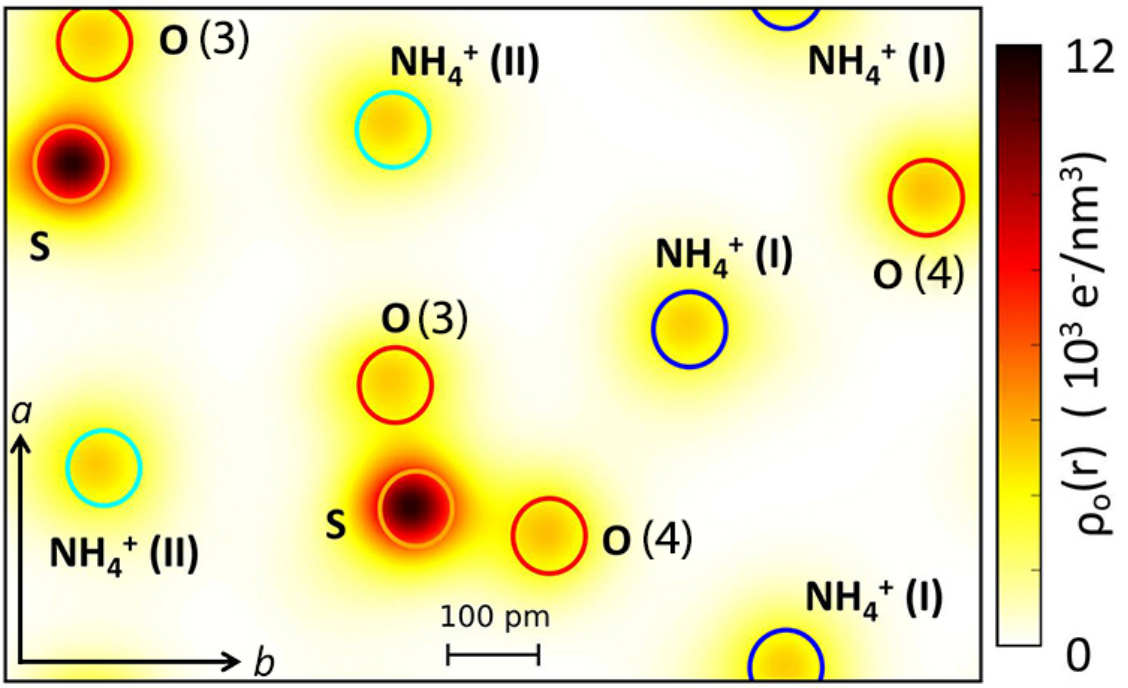

Figure 5.7: Electronic charge density contour map of the ground state of ferroelectric ammonium sulphate, $\rho_0(\mathbf{r})$, in the central region of the unit cell (a-b plane) and z = c/2. The positions of the atoms are indicated in the figure by the coloured circles.

Experimental transient charge density maps for ferroelectric ammonium sulphate upon 400nm photoexcitation

Here, the ground state charge density map and experimental transient charge density maps for ferroelectric ammonium sulphate upon 400nm photoexcitation are presented. The transient charge density maps were previously derived from the measurements of the variation of X-Ray diffracted intensity $\Delta I_{hkl}(t)/I^0_{hkl}$ by means of the BayMEM approximation, already fully discussed in Section 4.6.

The charge density maps for photoexcited ferroelectric ammonium sulphate, $\Delta\rho$ (**r**,t), are shown in Fig. 5.8 at different pump-probe time delays (a-b plane at z = c/2).

The parameter $\eta = 0.06 \pm 0.03$ is the fraction of excited unit cells by the pump pulse in the ammonium sulphate powder sample, and is estimated from the absorbed pump fluence ([7, 25]) as:

$$\Delta\rho(\mathbf{r},t) = \eta(\rho_{ex}(\mathbf{r},t) - \rho_0(\mathbf{r}))$$

where ρ_{ex}(**r**, t) and ρ_0(**r**) correspond, respectively, to the transient excited and equilibrium electronic charge densities. The locations of the atoms in the unexcited unit cell are marked with coloured circles to facilitate the comparison among the different contour maps.

The analysis of the static charge density map (Fig.5.7), and the transient charge density maps (Fig. 5.8) reveal the following features:

- There is a noticeable variation in the electronic charge densities, where the most relevant displacements in the electronic cloud, $\Delta\rho(\mathbf{r},t)$, occur in the vicinity of the ground state atomic positions (i.e., original locations of the atoms in the unexcited unit cell).

- No electronic charge density is displaced to previously unoccupied unit cell regions. This behaviour confirms the conservation of the ferroelectric lattice structure upon excitation.

- The transient charge shift modulation within the sulphate anion, SO_4^{2-}, behaves in a strongly anisotropic way: in the atom of sulphur and three of its four oxygen atom, the electronic charge shows a joint remarkable increase/decrease while in the fourth atom of oxygen (marked in the figures as atom O(4)), it behaves in an opposite way.

- The results demonstrate a completely different behaviour from that of paraelectric ammonium sulphate at room temperature ([7]). In that case, a concerted spatial relocation of electrons and protons into a channel-like geometry along the c-axis was observed.

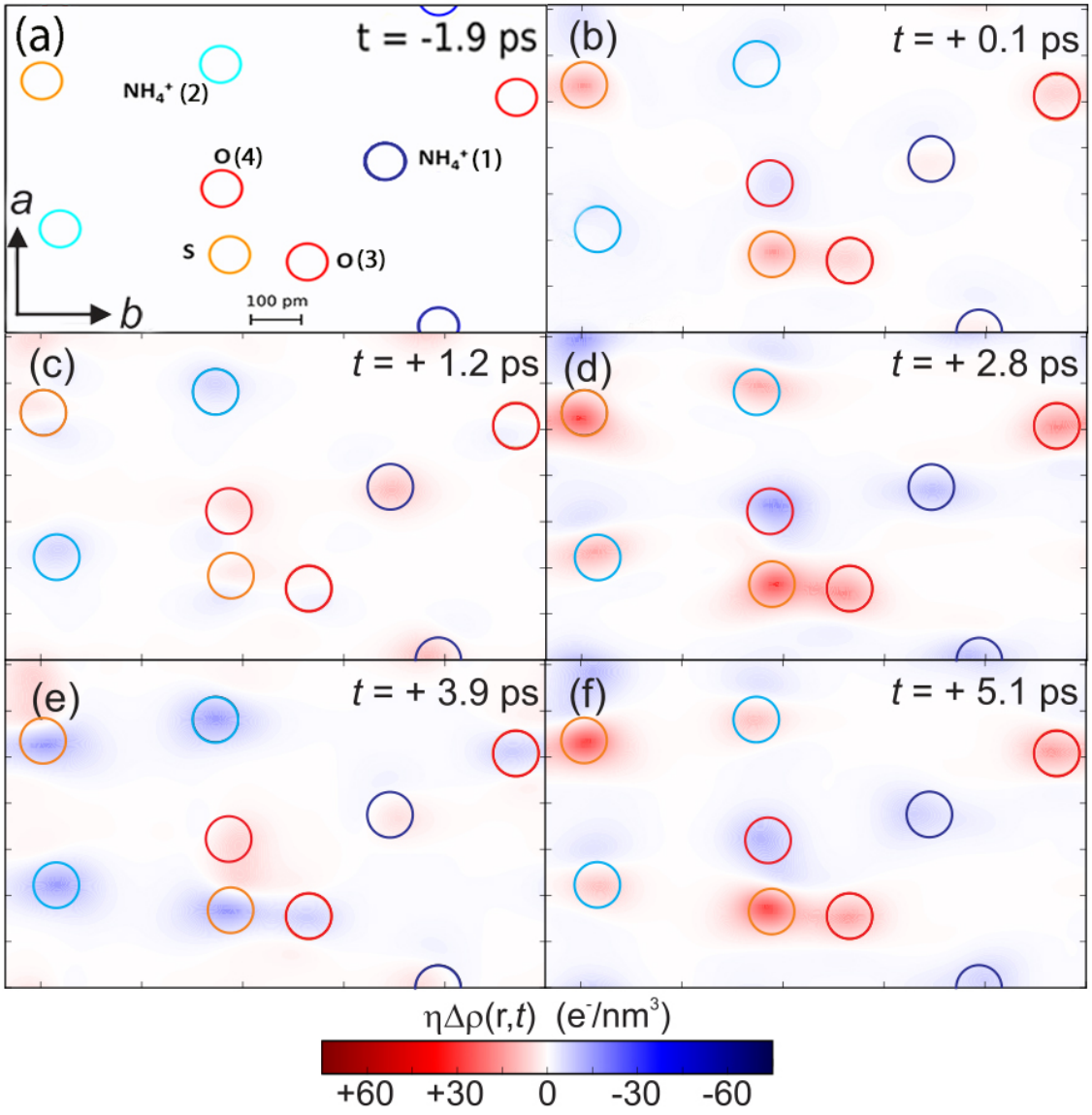

Figure 5.8: Contour map for the equilibrium and excited transient variations of the charge density, $\eta\Delta\rho$ (**r**,t) in the central region of the unit cell on the plane a-b at z = c/2 at time delays t = -1.9ps, +0.1ps, +1.2ps, +2.8ps, +3.9ps and +5.1ps. The locations of the atoms in the unexcited unit cell are indicated by the coloured circles.

For illustrative purposes, the Fig. 5.9 displays the behaviour of the electronic cloud at time delay = 2.8ps where the maximum amplitude of the charge modulations takes place. Two isosurface representations of $\Delta\rho$ (**r**,t) = $\pm$ 8 e/nm^3 are shown where the red and blue colouring correspond respectively to the charge increase and decrease. This representation corresponds to panel d in Fig. 5.8.

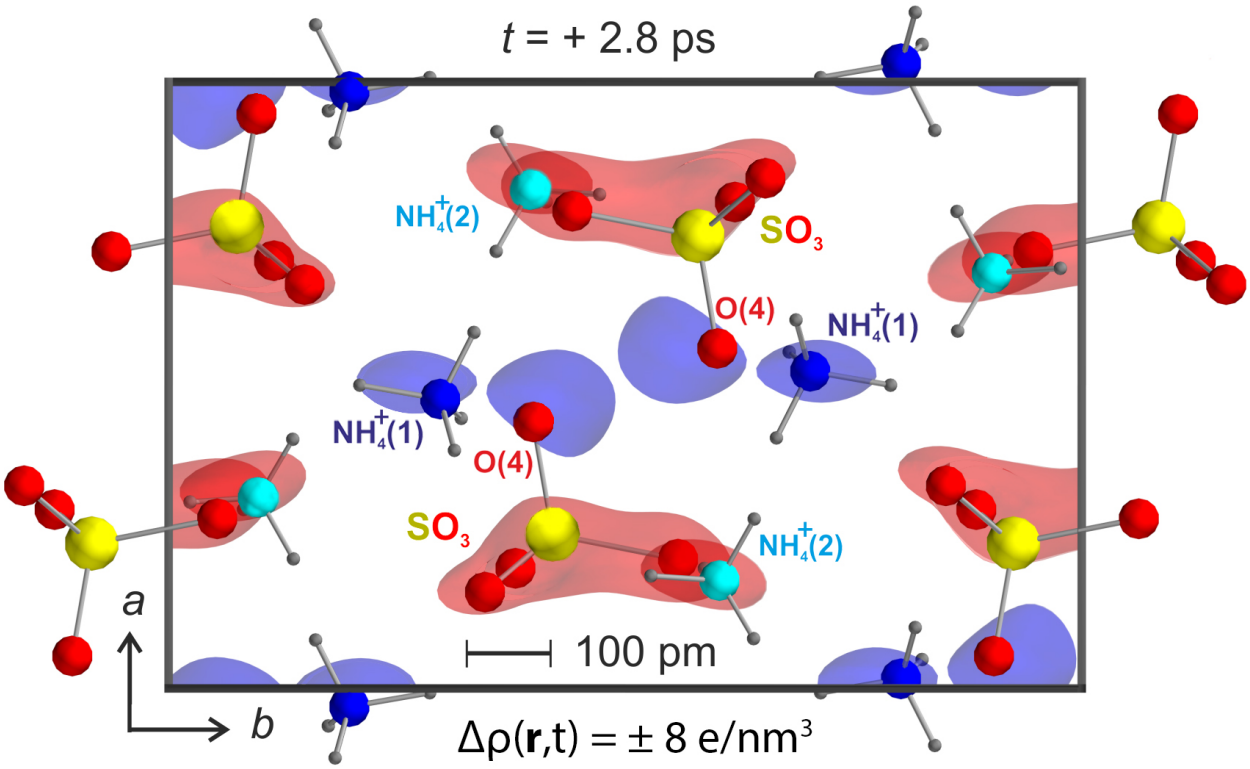

Figure 5.9: Representation of the maximum differential charge density, $\Delta\rho(\mathbf{r},t)$, along the crystallographic c-axis at time delay = 2.8ps with an isosurface value of $\pm$ 8 e/nm^3 in red (increase) and blue (decrease). The positions of the atoms in the unexcited ground state unit cell are indicated by coloured solid spheres). This situation corresponds to the panel d in Fig. 5.8.

5.3 Quantitative analysis of the transient charge density maps for photoexcited ferroelectric ammonium sulphate

The physical insight relative to the transient charge density maps is extracted and analysed in this section. Firstly, the methodology used to derive the different transient charge relocations in the unit cell is described and, secondly, the actual transient charge relocations are presented and discussed.

Procedure to calculate the transient electronic group charge translocations

The transient charge density maps have revealed that all variations in the electronic charge density in the unit cell take place in the vicinity of the atomic locations of the unexcited ferroelectric ammonium sulphate, and that there is no charge transfer to interstitial spaces in previously unoccupied regions (Sec. 5.2). Given this fact, a partitioning of the unit cell into different sub-volumes is established by taking the unexcited equilibrium crystal structure as basis to be able to derive the transient electronic charge relocations, $\eta\Delta Q(t)$. In this sense, the final transient charge relocations are obtained by integrating the charge density distribution over the artificially created sub-volumes, and the charge in each of them is assigned to its closest atom (as exemplified in the Fig. 5.10). The only exception to this

procedure is the case of the two crystallographically different ammonium cations, NH_4^+, where the entire charge from nitrogen and hydrogen atoms is considered together, given the impossibility to spatially resolve them by means of X-Ray diffraction.

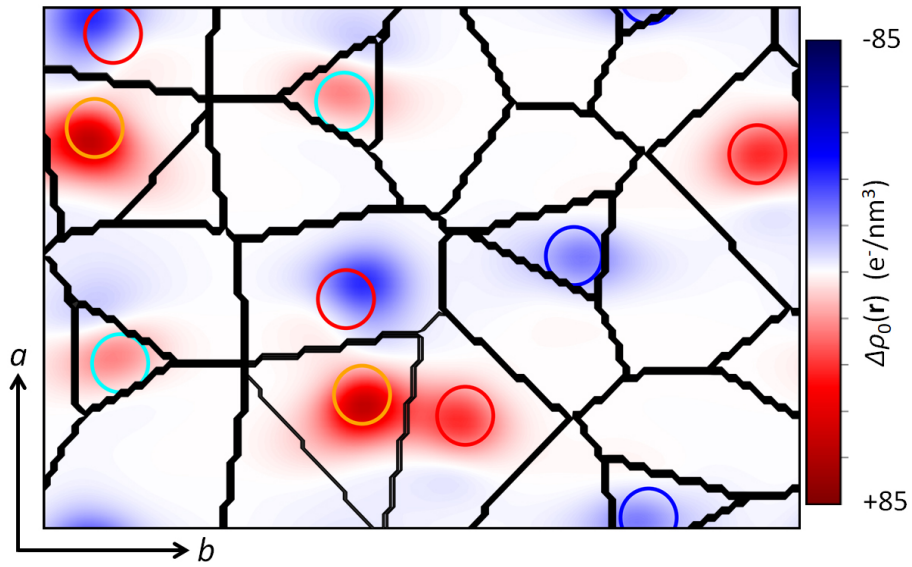

(a) Volume sub-divisions are artificially established in the unexcited unit cell of ferroelectric ammonium sulphate to derive the transient charge relocations.

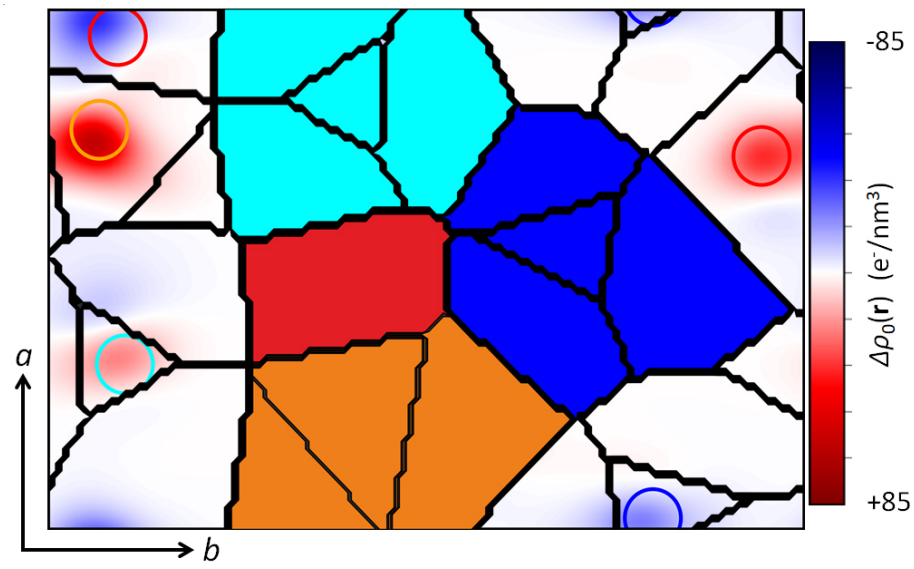

(b) The charge density in the differently coloured space regions is integrated, and the transient electronic charge relocations, $\eta\Delta Q(t)$ are assigned to the its closest atom.

Figure 5.10: In Fig. 5.10(a), the unexcited unit cell is depicted with the different artificial regions established to rationally assign the electronic charge translocations within the unit cell. In Fig. 5.10(b), the different colours indicate to which atom the whole of the electronic density in the region is ascribed. The circles in color red correspond to oxygen, in orange to sulphur, and in dark and light blue correspond respectively to the two crystallographically different nitrogen nuclei N(I) and N(II) in the NH_4^+ cations.

Analysis of the transient electronic group charge translocations

The transient charge translocations within the unit cell obtained from the previously explained methodology are presented and analysed here.

- The obtained transient electronic charge modulations in the photoexcited unit cell are:
  - the oxygen atom O(4) in the sulphate ion, SO_4^{2-}, Figure 5.12.
  - the SO_3 group in the sulphate ion, SO_4^{2-}, Figure 5.11.
  - the first crystallographically different ammonium cation, NH_4^+(I) Figure 5.13.
  - the second crystallographically different ammonium cation, NH_4^+(II) Figure 5.14.

The study of the transient electronic translocations reveals one of the most important results of this thesis, which is the existence of a significant concomitant charge modulation with a period of ∼3ps that corresponds to a frequency of 0.36±0.07THz (12±2 cm^{-1}). It is specifically linked to rearrangements of electronic charge between the atom of sulphur with three of the four oxygen atoms in the sulphate anion SO_4^{2-} (from now on referred to as the SO_3 group, Fig. 5.11), and the oxygen atom O(4) in the SO_4^{2-} anion (Fig. 5.12) combined with the first of the two crystallographically different ammonium cations, NH_4^+(I) (Fig. 5.13). In this sense, the maximum amplitude of the oscillation of the charge transfer for the SO_3 group is close to the sum of the maximum amplitude of the charge decrease on the NH_4^+(I) unit and the O(4) atom. The variation of charge in the second of the two crystallographically different ammonium cations, NH_4^+(II) comparatively presents much more limited variations (Fig. 5.14). It bears mentioning, that the frequency of the oscillation is much lower than the librational vibrations that affect the orientation of the SO_4^{2-} and NH_4^+ units ([71, 72, 101, 112]).

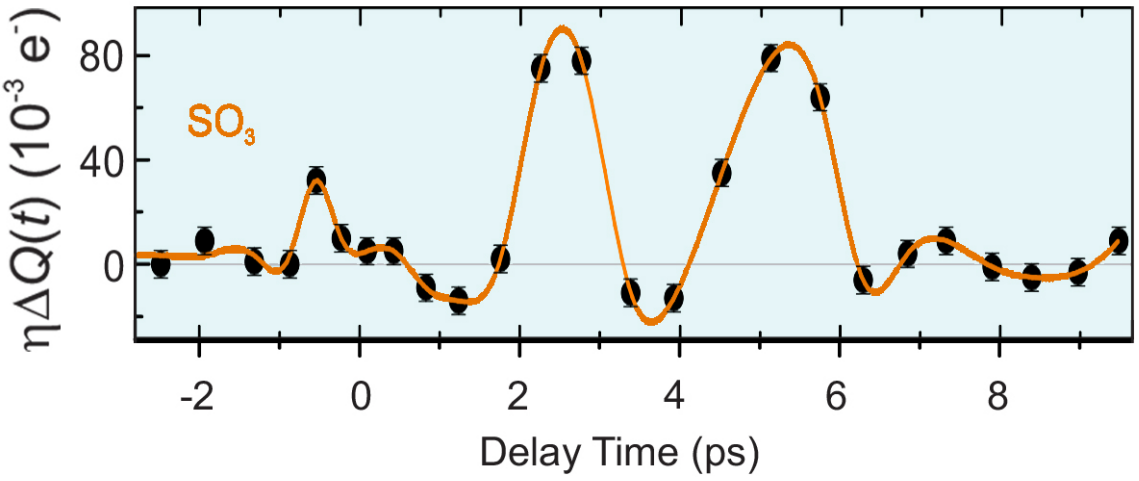

Figure 5.11: Transient charge modulation for the SO_3 group in the SO_4^{2-} anion, $\eta\Delta Q_{SO_3}(t)$, represented against the pump-probe time delay (black symbols). The orange solid line connecting the dots is a guide to the eye.

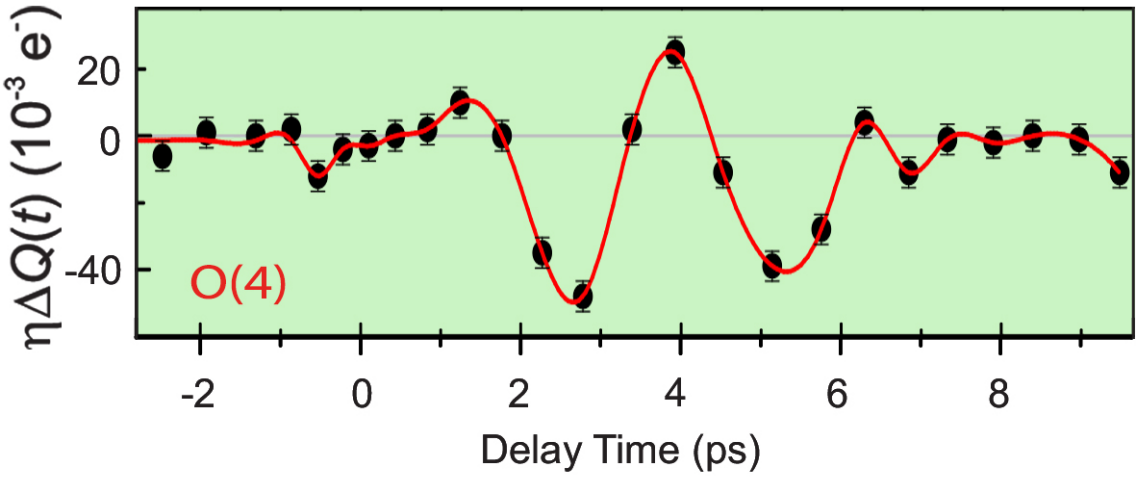

Figure 5.12: Transient charge modulation for the oxygen atom O(4) in the SO_4^{2-} anion, $\eta\Delta Q_{O(4)}(t)$, represented against the pump-probe time delay (black symbols). The red solid line connecting the dots is a guide to the eye.

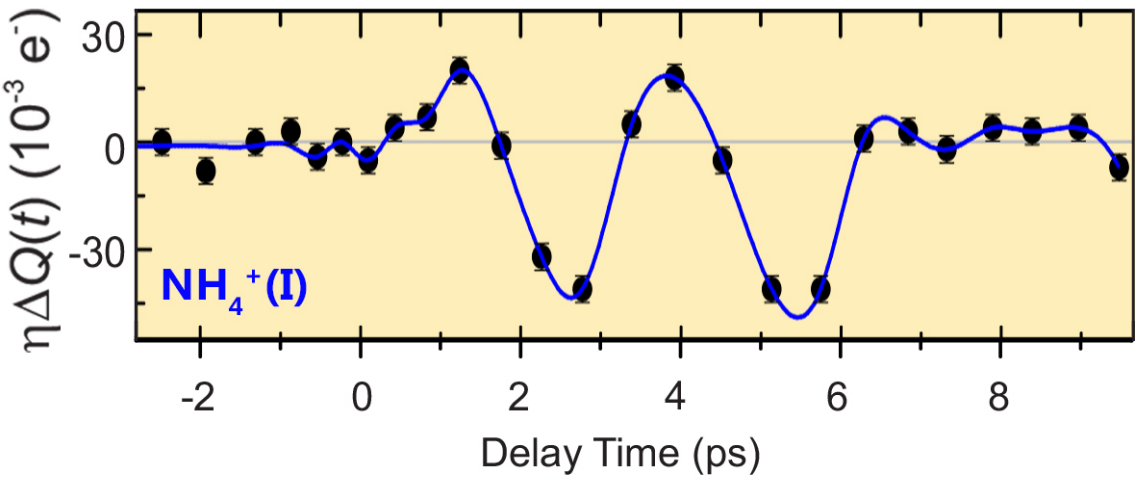

Figure 5.13: Transient charge modulation for the first of the two crystallographically different NH_4^+ cations, $\eta\Delta Q_{NH_4^+(I)}(t)$, represented against the pump-probe time delay (black symbols). The dark blue solid line connecting the dots is a guide to the eye.

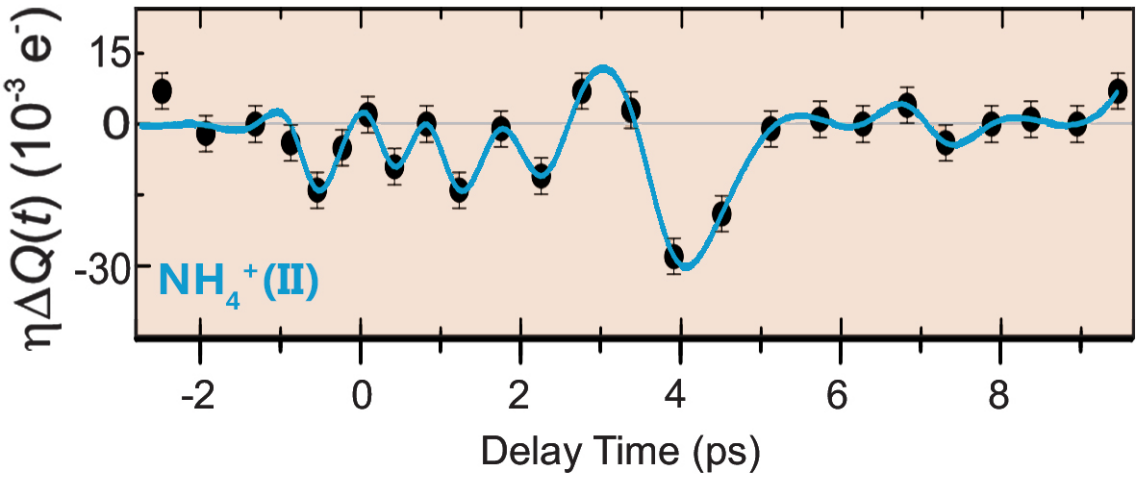

Figure 5.14: Transient charge modulation for the second of the two crystallographically different NH_4^+ cations, $\eta\Delta Q_{NH_4^+(II)}(t)$, represented against the pump-probe time delay (black symbols). The light blue solid line connecting the dots is a guide to the eye.

In conclusion, these results demonstrate a concomitant local net charge modulation with a period of $\sim$ 3ps (i.e., frequency of 0.36THz) from the SO_3 group to the O(4) atom and NH_4^+(I) cation over distances of around 100pm, which corresponds approximately to the distance of a chemical bond lengtht (Fig. 5.22). The other NH_4^+(II) unit shows much more limited variations in its associated charge transfer.

In the next section shall be explained how this concomitant charge modulation corresponds to a low-frequency lattice vibration.

Transient Nuclear Displacements

In general terms, X-ray photons mostly interact only with the electronic charge. Therefore, under the presents conditions, the behaviour of the nuclei cannot be probed. However, a methodology has been developed to estimate with good precision the position of the nuclei and calculate the transient nuclear lattice displacements. This methodology is described in this section and, subsequently, the obtained results are presented and discussed.

Procedure to calculate Transient Nuclear Displacements

The methodology consists of deriving the time-resolved atomic positions of the oxygen, nitrogen and sulphur atoms by fitting a 3D-gaussian distribution to the high core electron densities in the different atomic positions in the charge density maps.

The atomic core electrons, in contrast to valence electrons, are strongly bound around the nucleus and follow its movement readily without significant deformations of the electronic clouds. By combining this fact with the knowledge of the set-up limited experimental resolution, an upper boundary for the magnitude of the nuclear displacements can be estimated. Following this procedure, the time-resolved atomic locations and interatomic separations for the oxygen, sulphur, and the two crystalographically-different nitrogen atoms have been calculated. The accuracy of $\Delta d/d$ is on the order of a few femtometers, and the different exemplary error bars were derived by an analysis of the standard deviation before time delay zero. It bears mentioning that these values are much smaller than the size of a voxel, which is about 9pm long in the c direction. This is due to the fact, that the the estimation of the position of the nuclei is obtained by the 3-D gaussian fitting, which takes into account the information of the variation of electron density from many different voxels.

Magnitude of Transient Nuclear Displacements

The time-resolved atomic nuclei locations and interatomic separations in the unit cell are calculated by following the methodology explained in the previous sectionk and the results are presented here. These results reveal that the 0.36THz electronic charge oscillations are linked to very small sub-pm displacements of virtually all the heavy atoms in the unit cell. This demonstrates a strongly delocalized character for this oscillation in the lattice, with minute shiftings along the crystallographic a-, b-, and c-axes.

The obtained estimation for the transient nuclei relocations along the c-axis is shown in the following graphs (original atomic positions in Fig. 5.6 and Fig. 5.7):

- The sulphur nucleus, $\Delta r_c^S(t)$, (Fig. 5.15),
- The nitrogen nucleus N(1), $\Delta r_c^{N(1)}(t)$, (Fig. 5.16),
- The nitrogen nucleus N(2), $\Delta\ r_c^{N(2)}(t)$, (Fig. 5.17),
- The oxygen nucleus O(1) in the SO_4^{2-} anion, $\Delta\ r_c^{O(1)}(t)$, (Fig. 5.18),
- The oxygen nucleus O(4) in the SO_4^{2-} anion, $\Delta\ r_c^{O(4)}(t)$, (Fig. 5.19).
- The oxygen nuclei O(2) and O(3) in the SO_4^{2-} anion, $\Delta\ r_c^{O(2)}(t)$ and $\Delta\ r_c^{O(3)}(t)$, (Fig. 5.20).

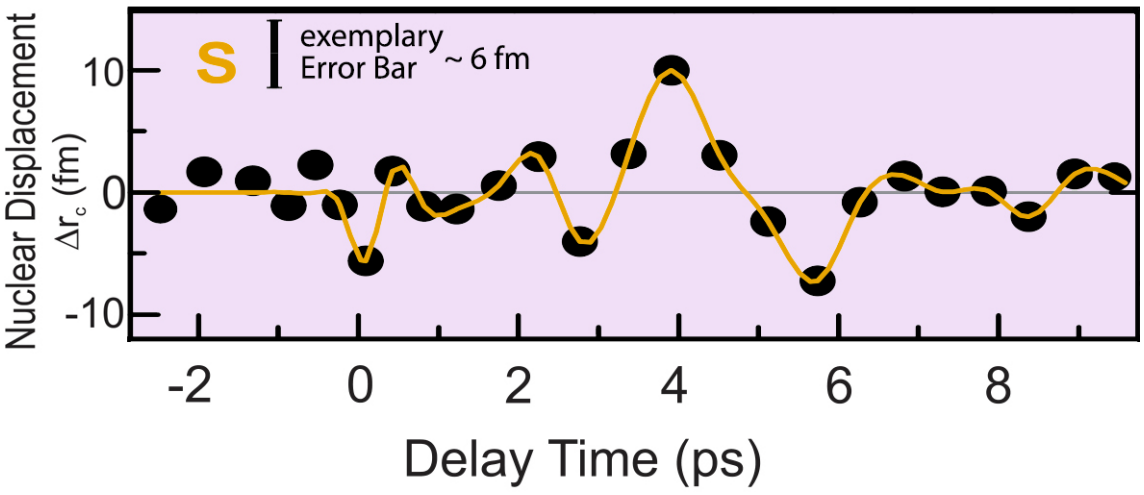

Figure 5.15: Time-resolved sulphur nucleus oscillation along the c-axis in the unit cell, $\Delta r_c^S(t)$. The exact location of the S atom in the sulphate ion, SO_4^{2-}, is specified in Fig. 5.6, Fig. 5.25, and Fig. 5.31. The coloured orange line is a guide to the eye.

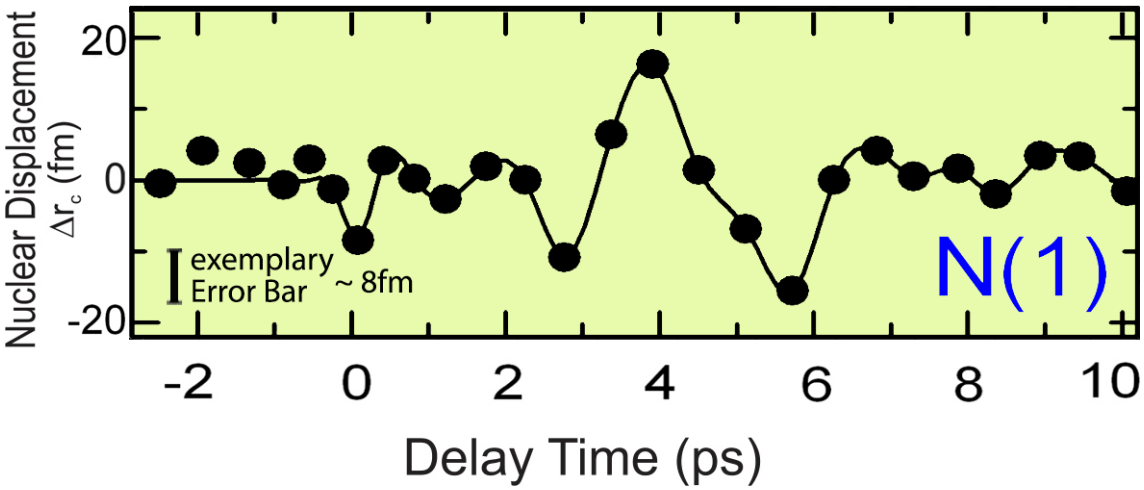

Figure 5.16: Time-resolved nitrogen nucleus N(1) vibration along the c-axis in the unit cell, $\Delta r_c^{N(1)}(t)$. N(1) corresponds to the first of the two crystallographically different ammonium cations, $NH_4^+(1)$, and its exact location is specified in Fig. 5.6 and Fig. 5.25. The coloured black line is a guide to the eye.

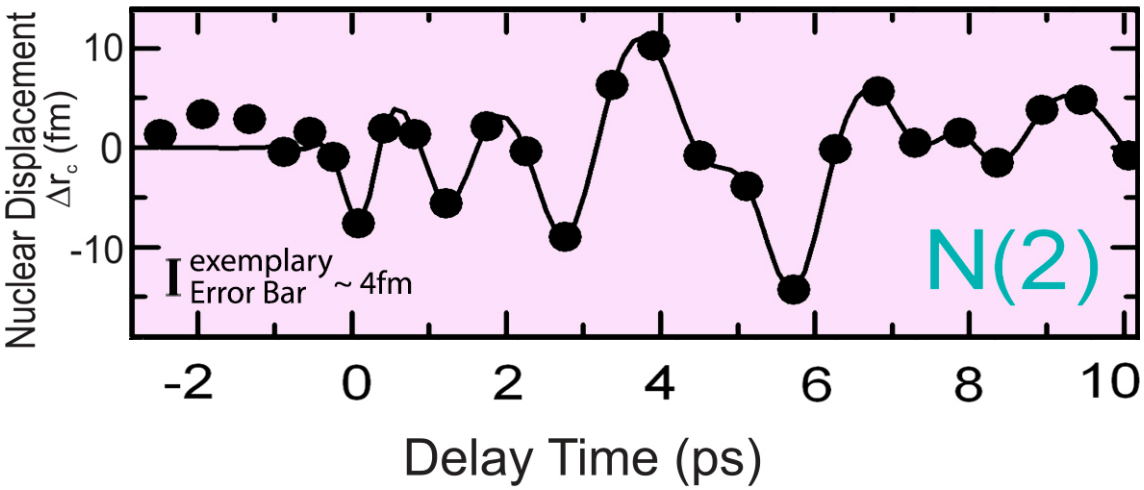

Figure 5.17: Time-resolved nitrogen nucleus N(2) vibration along the c-axis in the unit cell, $\Delta r_c^{N(2)}(t)$. N(2) corresponds to the nitrogen nucleus in the second of the two crystallographically different ammonium cations, $NH_4^+(2)$), and its exact location is specified in Fig. 5.6 and Fig. 5.25. The coloured black line is a guide to the eye.

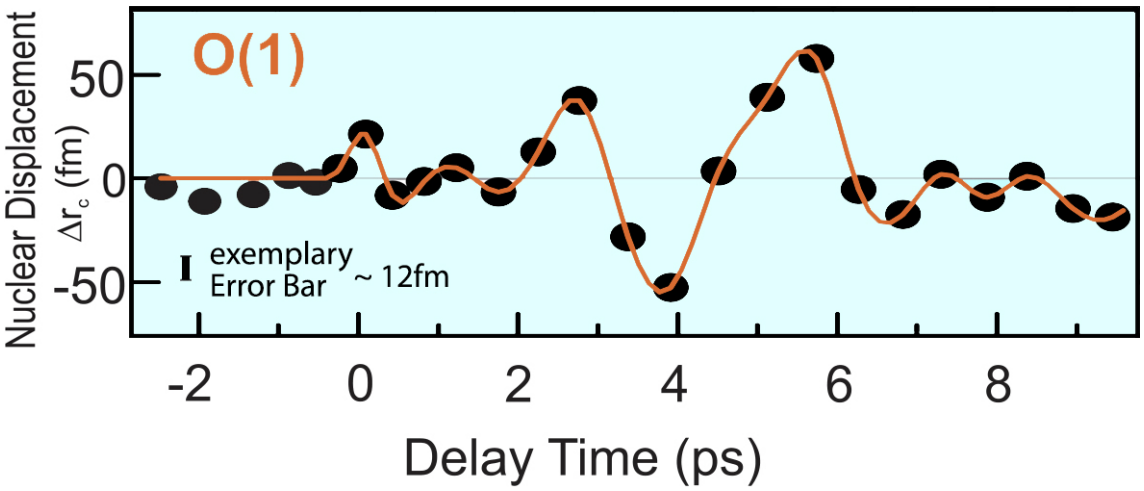

Figure 5.18: Time-resolved oxygen nucleus O(1) oscillation along the c-axis in the unit cell, $\Delta r_c^{O(1)}$(t). The exact location of the O(1) atom in the sulphate ion, SO_4^{2-}, is specified in Fig. 5.25, Fig. 5.6 and Fig. 5.31. The coloured orange line is a guide to the eye.

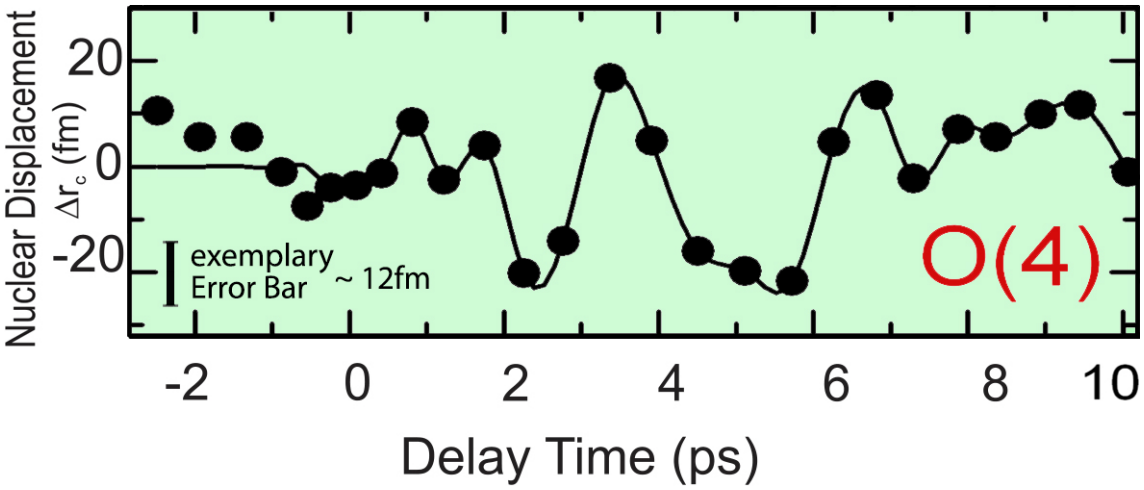

Figure 5.19: Time-resolved oxygen nucleus O(4) oscillation along the c-axis, $\Delta r_c^{O(4)}(t)$. The exact location of the O(4) atom in the sulphate ion, SO_4^{2-}, is specified in Fig. 5.25, Fig. 5.6 and Fig. 5.31. The coloured black line is a guide to the eye.

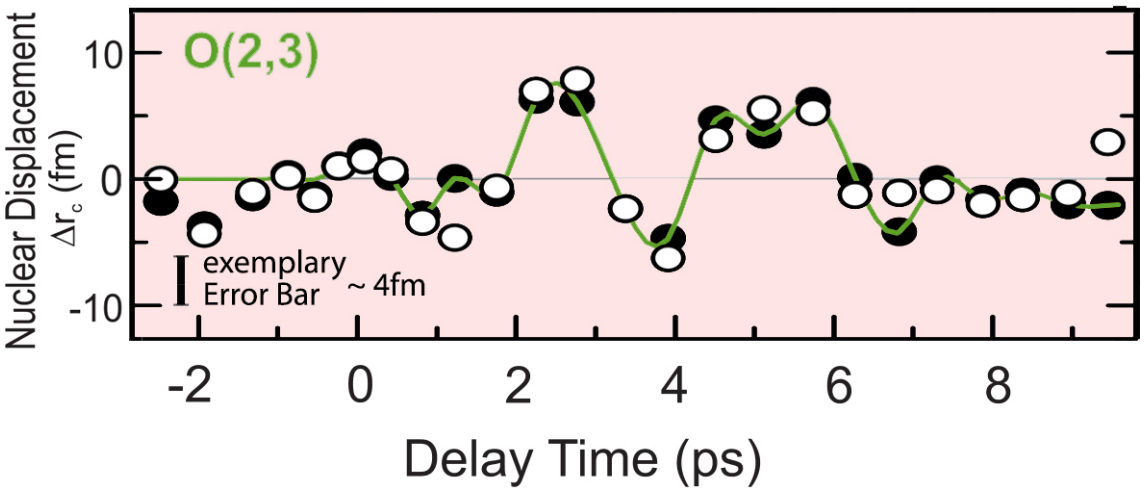

Figure 5.20: Time-resolved movement of the oxygen nuclei O(2) and O(3) along the c-axis of the unit cell, $\Delta r_c^{O(2)}(t)$ and $\Delta r_c^{O(3)}(t)$. White circles correspond to the nucleus O(2) and black circles to O(3). The exact location of the O(2) and O(3) atoms in the sulphate ion, SO_4^{2-}, are specified in Fig. 5.25, Fig. 5.6 and Fig. 5.31. The coloured green line is a guide to the eye.

The main conclusion obtained from the analysis of these figures is that the displacements of the nuclei along the the c-axis of the unit cell, which is the polar direction for ferroelectric ammonium sulphate, are in the sub-picometer vibration regime (Fig. 5.15 to Fig. 5.19).

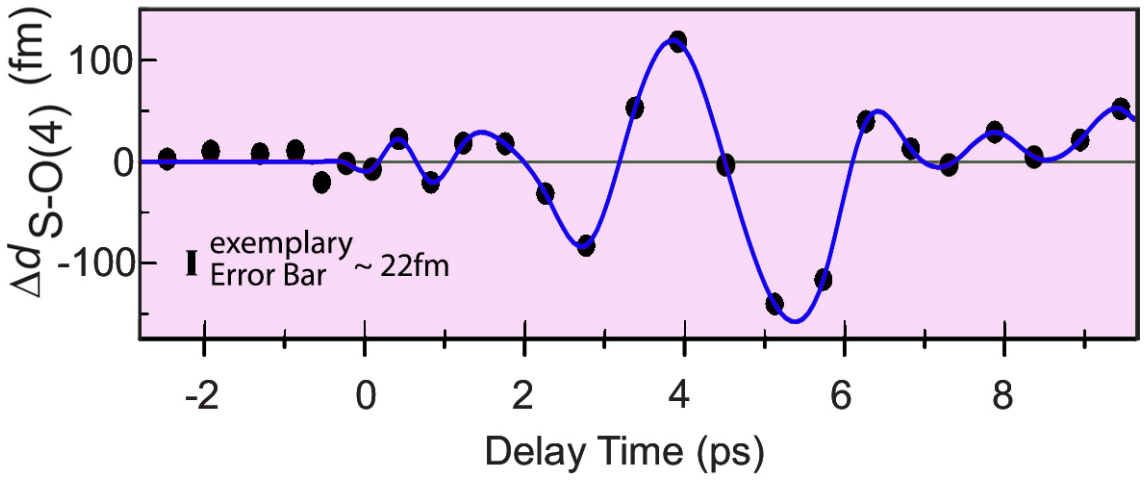

Figure 5.21: Transient modulation of the total bond length between the sulphur atom and the oxygen atom O(4), $\Delta d_{S-O(4)}$. The location in the ground state for the S and O(4) atom in the sulphate ion, SO_4^{2-}, is specified in Fig. 5.6, Fig. 5.25, and Fig. 5.31. The coloured blue line is a guide to the eye.

Also, the bond length modulation with observed largest amplitude, $\Delta d_{S-O(4)}$, is presented in Fig. 5.21 to illustrate further this general behaviour. It corresponds to the modulation of the distance of the sulphur atom and the oxygen O(4) on the a-b plane in the unit cell. The detail of the direction in the unit cell in which the transient modulation of the bond length between the sulphur and the oxygen atom O(4) takes place is shown in Figure 5.22. Its analysis discloses variations of length in the order of ∼100fm, i.e., approximately 1000 times smaller than the range of the electronic charge modulation of roundabout 100pm between the SO_3 group and the O(4) atom previously observed in Fig. 5.8.

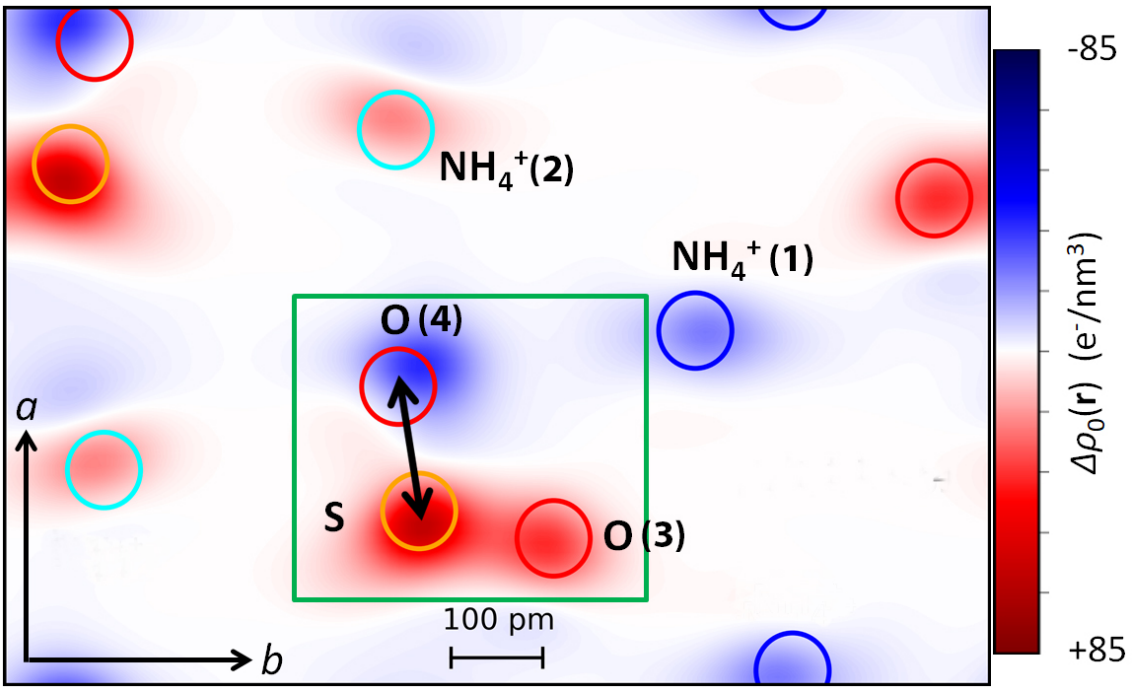

Figure 5.22: Detail of the direction (along the black arrow) in which the transient modulation of the total bond length between the sulphur atom and the oxygen atom O(4), $\Delta d_{S-O(4)}$, takes place (unit cell plane z = c/2) as presented in the Figure 5.21. The green square delimits the anion SO_4^{2-}. The transient charge density map is represented at time delay T = 2.8ps, which corresponds to the maximum amplitude of the charge transfer modulation.

Finally, it bears mentioning that the hydrogen charge obviously contributes to the total charge density but, it cannot be simply determined with the same methodology used with the other heavier atoms. Given the limited spatial resolution of the experimental set-up, it is not possible to discern the electron density maxima in the hydrogen atoms and, henceforth, the transient proton (H^+) locations within the ammonium cations, NH_4^+, cannot be determined accurately. Due to this reason, it is not possible to directly derive neither their contribution to the charge transfer, nor the estimation for the displacements of their nuclei. However, the hydrogen charge is not excluded from the calculations of the electronic, charge and polarization dynamics and, in the following, it is assumed that the four hydrogen atoms in a NH_4^+ cation have a constant time-independent separation to the nitrogen nucleus and follow its movement.

This is strongly supported by a series of facts:

- Experiments comparing the dielectric properties of protonated vs. deuterated ammonium sulphate ([35, 69]) present almost identical transition temperatures (T_C), entropy variations (ΔS), and maximal spontaneous polarizations (P_S) in the phase transition.

- This evidence backs the fact that proton/deuterium translocations with respect to their respective nitrogen nucleus have a minor influence in the transient macroscopic polarization. Furthermore, the frequencies of the vibrational modes for the hydrogen motions in the ammonium cations (NH_4^+) are approximately 100 times higher than the frequency of the newly discovered 0.36THz (12 cm^{-1}) oscillation mode with which the hydrogen motions are averaged out and become negligible over the lattice vibrational period, e.g., stretching and bending motions are in the range of $\sim$1100cm^{-1} to about $\sim$3200cm^{-1} ([72]).

Low-frequency coherent charge modulation with soft mode character

There are important conclusions that can already be obtained from the analysis of the transient charge density maps. There exists a newly-discovered charge modulation with frequency of 0.36THz that has a soft mode character, as it presents the hallmarks a soft mode as described in Sec. 2.2.2.

In this sense, firstly, the analysis of the electronic charge dynamics reveals that part of the electronic charge density experiences relocations during the coherent lattice motions in the order of a typical bond length, i.e., roundabout 100pm. These electronic charge oscillations are linked to minute nuclear displacements of a few dozens of femtometers in the practical totality of the heavy atoms in the unit cell, i.e., the lattice oscillations are three orders of magnitude smaller than the length of the electronic charge relocation (Fig. 5.12 to Fig. 5.14).

Secondly, the variation of diffracted intensity for photoexcited ferroelectric ammonium sulphate at 200K and at 110K (Figure 5.4) are significantly different, which suggests the existence of charge dynamics whose frequency depends on the temperature.

5.4 Phonon Excitation Mechanisms in Crystalline Materials

As previously mentioned, one of the most important results presented in this work is the newly-discovered 0.36THz coherent oscillation with soft mode character in the lattice of ferroelectric ammonium sulphate. The process to induce this oscillation starts with the optical excitation of electrons from the ground state to excited states. This electronic excitation results in a transient variation of the electronic charge distribution, that will subsequently activate the oscillation modes.

This phenomenon can basically happen by means of two different mechanisms, or a combination thereof: the direct and indirect displacive excitation. These two mechanisms are discussed in the following.

Indirect Displacive Phonon Excitation via Anharmonic Phonon-Phonon Interaction

The mechanism *indirect displacive excitation via anharmonic phonon-phonon interaction* (or likewise, *incoherent phonon excitation*), explains how a low-frequency oscillation mode can be induced impulsively by incoherent carrier relaxation that is on a time scale faster than or, at least comparable to, the oscillation period.

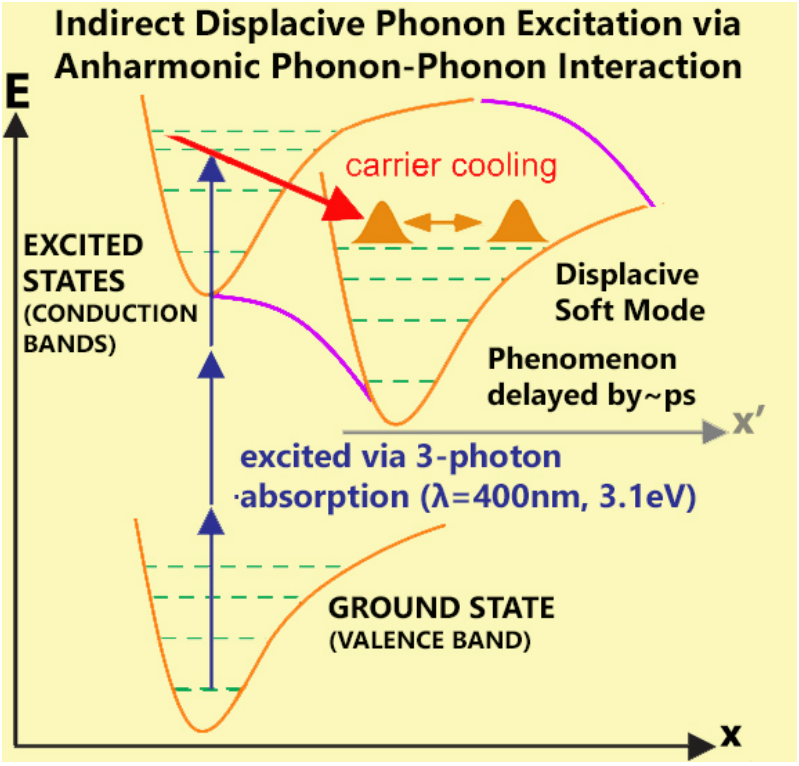

Figure 5.23: The figure shows that the fast incoherent carrier relaxation within the multidimensional potential of the electronic excited states (red arrow) can generate a displaced soft mode oscillation along the x' coordinate. In contrast to the direct displacive excitation mechanism, the onset of the phonon generation does not kick off instantaneously, since it is governed by relaxation kinetics that typically induce a delay in the order of a few picoseconds. The optical excitation for the ferroelectric ammonium sulphate, given its energy bandgap, would have to consist of a 3-photon absorption phenomenon.

The process is summarized in the Figure 5.23. The promotion of electrons from the valence to the conduction band, via multi-photon absorption, results in a non-equilibrium state where the conduction band is populated with hot, non-thermalized electrons ([24, 213, 214]). Subsequently, those hot electrons are redistributed by means of electron-electron scattering in the conduction band within ∼100fs. The statistical model for this situation corresponds to a thermal population with probability distribution corresponding to the finite temperature Fermi-Dirac distribution ([214, 215]). Finally, if the hot electron gas cooling has a duration shorter or, in the order of, the oscillation period, a quick dephasing of the coherent wavepackets due to anharmonic phonon-phonon scatering can follow and a rapid heating of the crystal lattice is induced. This non-equilibrium state, in general, produces an impulsive stress, that induces coherent acoustic phonons ([23, 24]).

In addition to the variation of the structure factors produced by the generation of those coherent oscillations, the heating of the crystal lattice also typically produces a disorder increase in the the unit cell, given that atoms undergo stronger thermal vibrations at their lattice locations. This effect induces a further reduction in the structure factors in all observable Bragg peaks in concordance to an attenuationg of the X-Ray scattering as indicated by the temperature-dependent Debye-Waller factor[122]).

Finally, it also bears mentioning that anharmonic phonon-phonon scattering can only be understood (along with other scattering effects, such as the *electron-phonon scattering* and the *phonon defect scattering*) within the framework of anharmonic interactions and asymmetric potentials. These are also responsible for other phenomena in condensed matter such as *temperature-dependent thermal conductivity* or *volume-dependent elastic constants* ([213, 216]).

Direct Displacive Phonon Excitation via Electronic Deformation Potential

The *direct displacive phonon excitation via deformation potential* (or *electron-phonon coupling through deformation potential*) is illustrated in Fig. 5.24 ([7, 23]). This phenomenon is related to the existence of a shift in the origin of the electronic excited state potential with respect to the origin of the electronic ground state potential, that is located along the axis where the lattice vibration takes place, i.e., in this case, along the axis where the low-frequency soft mode takes place. Under such condition, the photoexcitation of a crystal by a femtosecond pump pulse induces a coherent non-stationary superposition of vibrational quantum states that generate the phonon. This superposition of vibrational quantum states can be mathematically modeled as a cosine-like oscillation along the vibrational coordinate x with respect to the minimum of the excited state potential. The phase of the cosine-like oscillation depends on the excitation mechanism, and in the case of a displacive excitation, it must start with the maximum amplitude, i.e., $x(t) = x_0 \cos(\omega t)$, where x_0 is the maximal vibration amplitude and ω is the vibration frequency of the wavepacket. One of the crucial features of the direct displacive excitation mechanism, is that it takes place in a quasi-instantaneous way, i.e., an immediate onset of the phonon generation is expected, with which typically the time delay is t ∼0ps.

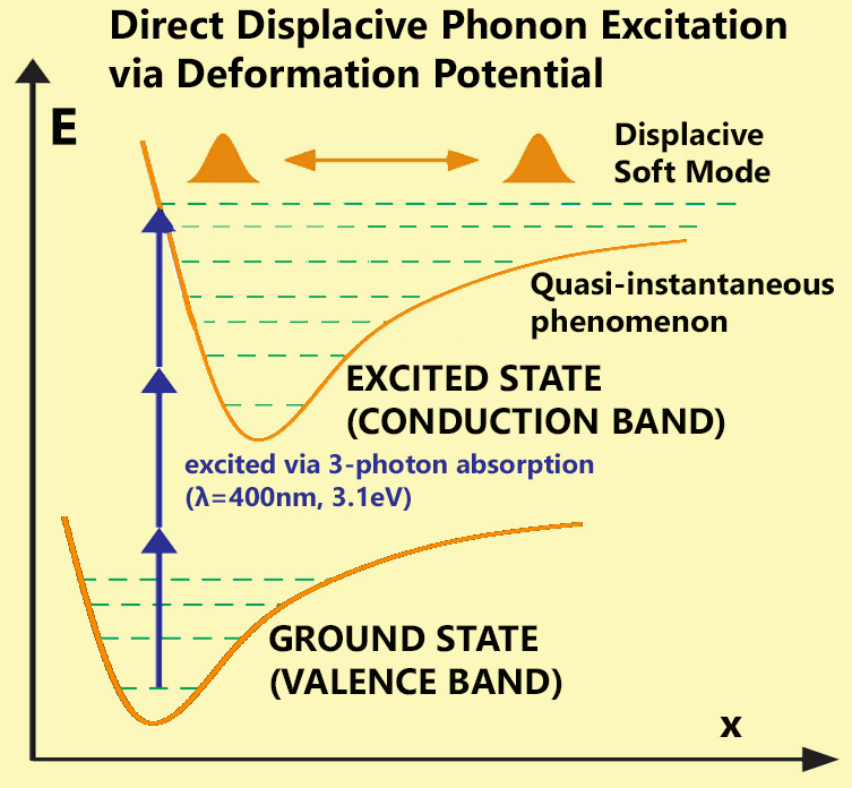

Figure 5.24: Scheme for Direct Displacive Phonon Excitation mechanism. The figure shows schematically the electronic ground state potential (Valence Band) and the electronic excited state (Conduction Band) along the lattice vibration axis for the low-frequency soft mode. In the direct displacive excitation mechanism, the optical pump excitation produces a displaced wave packet in the electronic excited state which ultimately kicks off the quasi instantaneous generation of the soft mode oscillation. The optical excitation for the ferroelectric ammonium sulphate, given its energy bandgap, would have to consist of a 3-photon absorption phenomenon.

Phonon Generation Mechanism in Photoexcited Ferroelectric Ammonium Sulphate

For ammonium sulphate, in contrast to other ferroelectrics, e.g., lithium niobate, there is almost no theoretical or experimental research on eventual phenomena of deformation potentials or anharmonic phonon-phonon couplings.

From the analysis of the experimental results in the previous figures (Fig 5.4 to Fig. 5.14), it can be appreciated that the cosine-like oscillations present in the optically excited ferroelectric ammonium sulphate do not start immediately at time delay zero, but rather display a somewhat delayed onset for the oscillations of ≈2-3 ps, which suggests a predominance of the *indirect phonon excitation via anharmonic phonon-phonon interaction* mechanism under the present experimental conditions.

5.5 Derivation of the macroscopic polarization dynamics from the transient charge density maps

The derivation of the macroscopic polarization dynamics in ferroelectric ammonium sulphate upon excitation of the 0.36THz modulation with soft mode character is addressed now.

The analysis of the transient electronic charge density maps (Fig. 5.7 and Fig. 5.8) has revealed that the unexcited and photoexcited ferroelectric ammonium sulphate remain in the same original crystal structure. In this sense, the electronic charge density on the a-b plane maintains the inversion symmetry throughout the photoexcitation and the components of the polarization on the a-b plane remain null. Contrarily, there exists a net electric dipole moment along the c-axis produced by the tilting of the $NH_4^+(2)$ and SO_4^{2-} ions (Fig. 5.25, and Sec. 2.3.1),

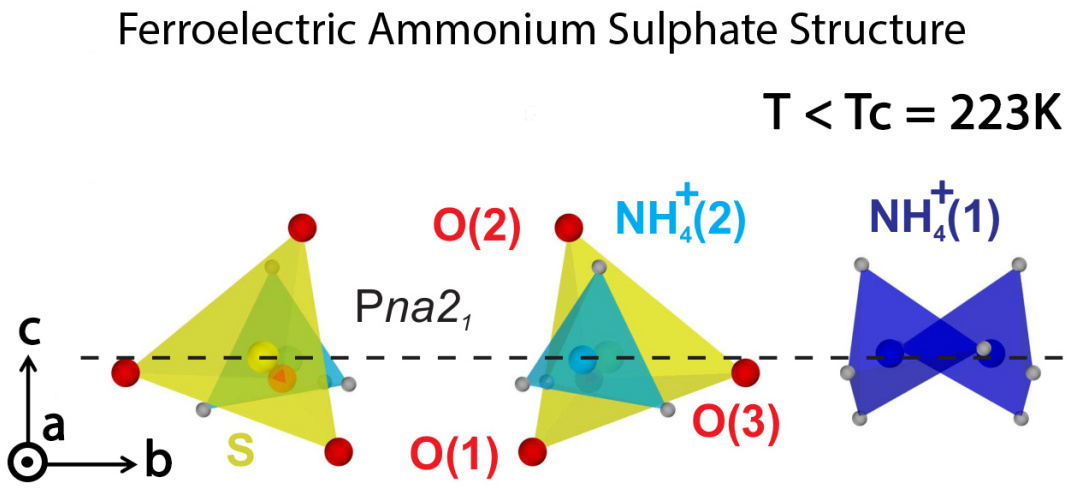

Figure 5.25: Detail of the orientation of NH_4^+ and SO_4^{2-} ions along the c-axis both for the unexcited and photoexcited ferroelectric phase of ammonium sulphate ($Pna2_1$ space group). The position of the atoms in the ferroelectric ammonium sulphate are indicated by coloured spheres, i.e., red is oxygen, grey is hydrogen, yellow is sulphur, whereas the crystallographically non-equivalent ammonium ions are given in light blue and dark blue.

Ferroelectric ammonium sulphate is conformed by a neutral molecular distribution in layers parallel to the a-b plane, which are separated by zones of negligible electron density (as seen in Fig. 5.26). This situation is very close to what in the language of Resta is called the Clausius-Mossotti case, which corresponds to crystals where the electronic charge is entirely localized around individual ions, i.e., the charge is strongly bound to its ionic entities ([11]) . By studying the transient charge densities derived in Section 5.3, it can be concluded that, even during the soft mode oscillation, any microscopic currents flowing between one molecular layer and its adjacent layers are very low and can be neglected in good approximation. Under this circumstances, the variation of polarization can be calculated from

the classic electromagnetic definition by dividing the unit cell with unevenly interfaces that follow the lowest electronic charge density along the c-direction ([10]).

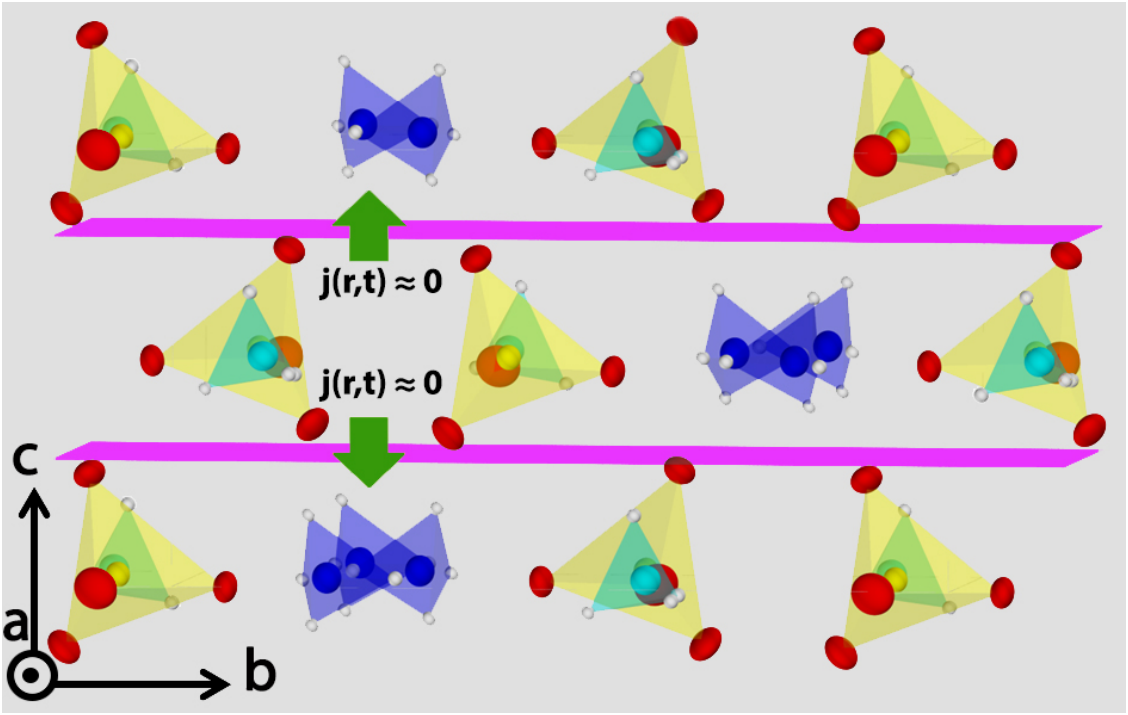

Figure 5.26: By analysing the charge density maps, it can be concluded that, in a first order approximation, the electronic density, $\rho(\mathbf{r}, t)$, can be decomposed into localized neutral sub-units which are organized in layers. The microscopic currents through the boundaries of these layers are negligible even during the soft mode oscillation.

The average electric field and polarization terms vanish in the a-b plane for symmetry reasons and, therefore, the average electric field and variation of polarization have to appear parallel to the c-axis (Fig. 5.25). Also, since the analysis of the transient charge density maps permits to decouple the movement of the nuclei and the electronic charge, the expression for the transient variation of polarization, $\Delta\mathbf{P}(t)$, can be separated into two differentiated terms:

$$\Delta\mathbf{P}(t) = \Delta\mathbf{P}_{c-axis}(t) = \Delta\mathbf{P}^{electron}_{c-axis}(t) + \Delta\mathbf{P}^{nuclei}_{c-axis}(t) \tag{5.1}$$

where $\Delta\mathbf{P}^{electron}_{c-axis}(t)$ and $\Delta\mathbf{P}^{nuclei}_{c-axis}(t)$ correspond to the electronic and nuclear contributions to the variation of macroscopic polarization, respectively.

In the following, the contribution of the nuclei and of the electronic density to the variation of macroscopic polarization are studied independently. In the last section, both effects are summed to obtain the total variation of macroscopic polarization.

5.5.1 Electronic contribution to the variation of macroscopic polarization

The practical way to tackle this problem is to solve the instantaneous Poisson equation:

$$\Delta\phi(\mathbf{r},t) = -\rho(\mathbf{r},t)/\varepsilon_0$$

from where the microscopic electric field can be derived:

$$\mathbf{E}(\mathbf{r},t) = -\nabla\phi(\mathbf{r},t)$$

The average electric field in the unit cell can be calculated with the help of the expression:

$$\mathbf{E}_{UC}(t) = \Omega_{UC}^{-1}\int_{\Omega_{UC}}\mathbf{E}(\mathbf{r},t)\cdot d\Omega$$

where the integration over the entire unit cell is performed in regions separated by the low-electronic density boundaries. Finally, once known the average electric field, the electronic contribution to the variation of the macroscopic polarization $\Delta P_{c-axis}^{electron}(t)$ is given by:

$$\Delta P_{c-axis}^{electron}(t) \;=\; -\varepsilon_0\{E_{UC}^{c-axis}(t) \;-\; E_{UC}^{c-axis}(t=-\infty)\}$$

.

where $E_{UC}^{c-axis}(t)$ and $E_{UC}^{c-axis}(t=-\infty)$ correspond to the transient and unexcited average electric field in the unit cell, respectively. The electronic contribution to the transient variation of polarization parallel to the c-axis has been calculated following this methodology and the result is presented in Figure 5.27.

It is important to point out that the method used here to derive the variation of macroscopic polarization is only applicable to a minority of materials that, as ferroelectric ammonium sulphate, can be understood with a good approximation in the context of Clausius-Mossotti case. For the the more general case where the electronic wave functions are delocalized within the unit cell due to the character of a bond which is more covalent than ionic (e.g., $KNbO_3$, [12]), the method to derive the macroscopic variation of polarization $\Delta\mathbf{P}(t)$ from the transient electronic charge density is more complicated ([16]).

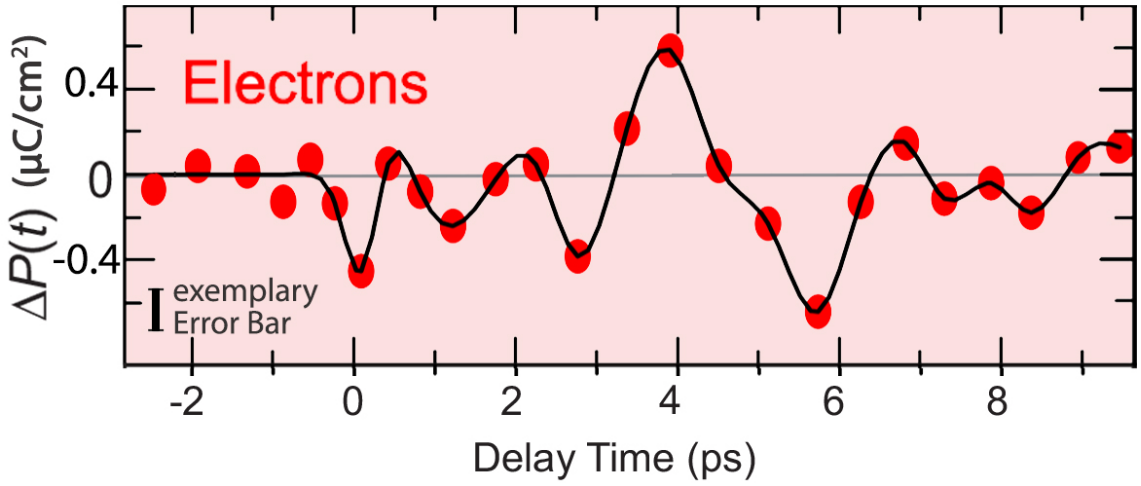

Figure 5.27: Transient electronic contribution to the variation of macroscopic electric polarization as derived from the experimental data. The calculated points correspond to the red symbols and the solid line is a guide to the eye. The typical uncertainty value is indicated as an exemplary error bar on the left side of the graph.

5.5.2 Contribution of the nuclei to the variation of macroscopic polarization

The contribution of the nuclei to the variation of macroscopic polarization, $\Delta\mathbf{P}^{nuclei}_{c-axis}(\mathrm{t})$, is defined as the sum of all the individual contributions associated to each nucleus in the unit cell:

$$\begin{aligned}\Delta P_c^{\mathrm{nuclei}}(t) &= \frac{4e_0}{abc}\Big\{16\,\Delta R_c^{\mathrm{S}}(t)+(7+4)\left[\Delta R_c^{\mathrm{N}(1)}(t)+\Delta R_c^{\mathrm{N}(2)}(t)\right] \\ &\quad +8\left[\Delta R_c^{\mathrm{O}(1)}(t)+\Delta R_c^{\mathrm{O}(2)}(t)+\Delta R_c^{\mathrm{O}(3)}(t)+\Delta R_c^{\mathrm{O}(4)}(t)\right]\Big\}. \qquad (5.2)\end{aligned}$$

where ΔR_c^A is the sum of nuclear displacements of all atoms of type A in the unit cell along the c-axis. The pre-factors in the equation correspond to the the nuclear charges, including the proton charges in the second term of the equation.

By applying Eq.5.2, the time-dependent nuclear charge contribution to the total variation of macroscopic polarization is calculated and presented in the Figure 5.28.

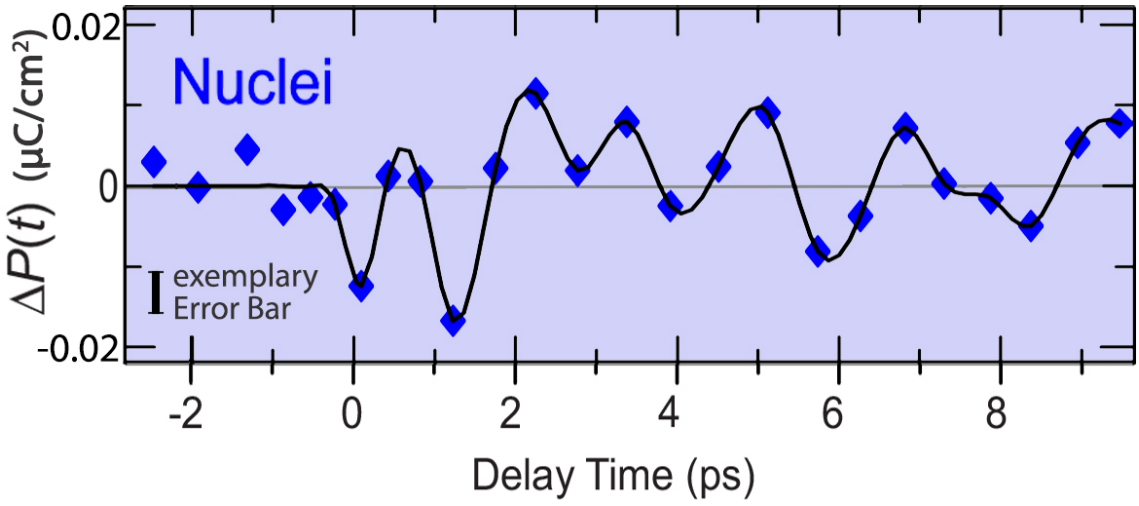

Figure 5.28: Time-dependent nuclear contribution to the total variation of macroscopic polarization as derived from the experimental data. The blue symbols correspond to the calculated points, and the black solid line is a guide to the eye. The typical uncertainty value is indicated as an exemplary error bar on the left side of the graph.

As can be seen, by comparing Fig. 5.20 and Fig. 5.21, the transient nuclear vibrations associated to the soft mode oscillation display an analogous evolution to that of the electronic charge density, although the nuclear vibrations correspond to minute displacements in the order of some tens of femtometers.

5.5.3 Transient total variation of macroscopic polarization

Finally, once obtained the variation of macroscopic polarization associated to electronic charge density oscillations ($\Delta\mathbf{P}^{electron}_{c-axis}$(t), Sec. 5.5.1), and associated to nuclei oscillations ($\Delta\mathbf{P}^{nuclei}_{c-axis}$(t), Section 5.5.2), the next step consists in summing both magnitudes to obtain the total variation of macroscopic polarization.

In a first analysis of both contributions, it can be appreciated that the nuclei contribution is approximately 30 times smaller than the electronic contribution. This is a logical outcome since the nuclei oscillations are approximately 3 orders of magnitude smaller than the typical amplitude for the oscillations of the electronic charge displacements that are in the order of 100pm. It can be concluded, then, that the nuclei contribution to the variation of polarization is minimal, and can be neglected according to the approximation:

$$\Delta\mathbf{P}(t) = \Delta P_{c-axis}(t) = \Delta P^{electron}_{c-axis}(t) + \Delta P^{nuclei}_{c-axis}(t) \approx \Delta P^{electron}_{c-axis}(t) \tag{5.3}$$

Figure 5.29 shows the total resulting transient variation of macroscopic polarization. As can be seen, it consists of a modulation that in its maxima reaches the value $|\Delta\mathbf{P}(t)| \simeq 0.6\mu\text{Ccm}^{-2}$. For comparison reasons, in the graph with dashed lines it is also presented the spontaneous ground state ferroelectric polarization $P_S^{ground}(T = 200K) \simeq 0.45\mu\text{Ccm}^{-2}$ ([69], and Fig. 2.12).

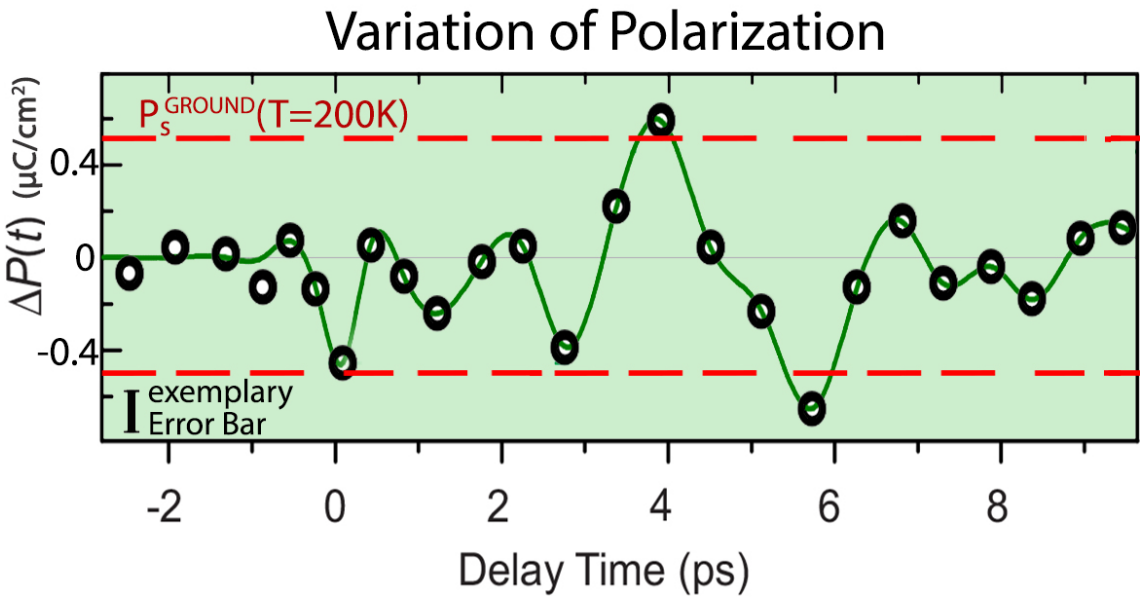

Figure 5.29: Total transient variation of macroscopic electric polarization as derived from the experimental transient charge density data in photoexcited ferroelectric ammonium sulphate at temperature T = 200K. The green solid line is a guide to the eye. The dashed green lines mark the amplitude of the spontaneous polarization for the unexcited ferroelectric Ammonium Sulphate at T = 200K. On the left side of the graph, an exemplary typical error bar is given ($\sim 0.09\ \mu\text{Ccm}^{-2}$), which has roughly the size of the round symbols.

While the sign of the variation of polarization, $\Delta\mathbf{P}(t)$, relative to the crystal structure has remained unknown ([69]), these results demonstrate that the maximum amplitude of the variation of polarization in photoexcited ferroelectric ammonium sulphate at temperature T = 200K is close in value to the full spontaneous polarization for unexcited ferroelectric ammonium at that same temperature:

$$\mathbf{P}_S^{GROUND}\ (T = 200K) \approx |\Delta\mathbf{P}^{EXCITED}\ (T = 200K)|$$

The direct calculation of the uncertainty for the variation of macroscopic polarization, $\Delta\mathbf{P}(t)$, is not directly feasible, but it can be estimated from the average scatter of the data points before time delay zero at $\sim 0.09\ \mu\text{Ccm}^{-2}$.

5.6 Discussion of Experimental Results

The main conclusions of the analysis of the experimental results are discussed now. These include: charge density dynamics, the soft mode character of the newly discovered 0.36THz coherent oscillation, the transient variation of polarization, the low-frequency phonon excitation mechanism, and the reasons for the fast dephasing of the observed low-frequency coherent oscillation with soft mode character.

Charge Density Dynamics

One the most important results in this thesis is the discovery of a local charge coherent oscillation with a period of ∼3ps, that corresponds to a characteristic frequency of 0.36THz. It is specifically associated to rearrangements of electronic charge between the atom of sulphur with three of the four oxygen atoms in the sulphate anion SO_4^{2-} (i.e., the SO_3 group, Fig. 5.11), and the oxygen atom O(4) in the SO_4^{2-} anion (Fig. 5.12) combined with the first of the two crystallographically different ammonium cations, NH_4^+(I) (Fig. 5.13). The variation of charge in the second of the two crystallographically different ammonium cations, NH_4^+(II) is comparatively much more limited (Fig. 5.14).

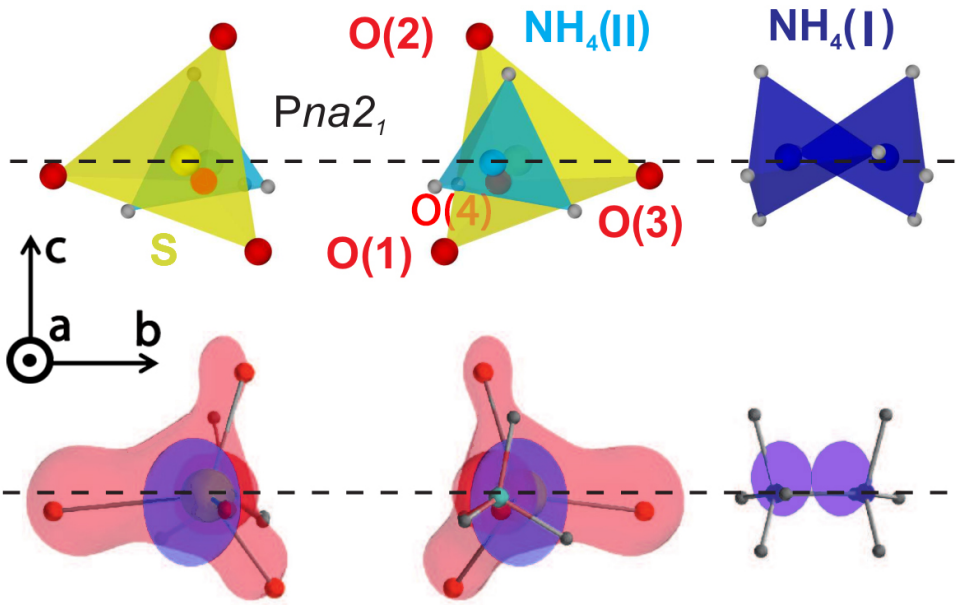

Figure 5.30: **Upper panel**: Detail of the NH_4^+ and SO_4^{2-} ions along the c-axis in ferroelectric ammonium sulphate. The position of the atoms in the unexcited unit cell are indicated by coloured spheres (red is oxygen, grey is hydrogen, yellow is sulphur, and light blue and dark blue correspond to the nitrogen atoms of the crystallographically non-equivalente ammonium cations).
Lower panel: Representation of isosurfaces of the variation of electronic charge density that correspond to $\eta\Delta\rho(\mathbf{r},t) = +14e/nm^3$ (increase in red) and $\eta\Delta\rho(\mathbf{r},t) = -14e/nm^3$ (decrease in blue) aat a time delay of 2.8ps (T = 200K). Note: The slightly darker red colouring on the isosurface associated with the SO_4^{2-} anion corresponds only to an overlap of the isosurfaces in this particular viewing direction.

To illustrate the dynamics of the electronic cloud, isosurfaces representing the variation of electronic charge density, $\eta\Delta\rho(\mathbf{r}, t)$, for ferroelectric ammonium sulphate (b-c plane at T = 200K) are given in Fig. 5.30 at the time delay 2.8ps which corresponds to the maximum amplitude of the charge oscillation. In the upper panel of the figure are represented as solid spheres the static positions of the ions NH_4^+ and SO_4^{2-} on the b-c plane. In the lower panel, the blue and red transparent colour contours show the different spatially resolved zones of the electronic cloud (where red represents charge increase, and blue represents charge decrease).

This depiction shows how the low-frequency coherent oscillation with soft mode character shifts electronic charge between the SO_4^{2-} and NH_4^+(I) ions in a highly anisotropic fashion. In the figure can be seen how the O(4) oxygen atom and the first of the two crystallographically different cations, NH_4^+(I), exhibit an modulation of the charge density in an exactly reversed fashion to that of the atom of sulphur and the other three oxygen atoms.

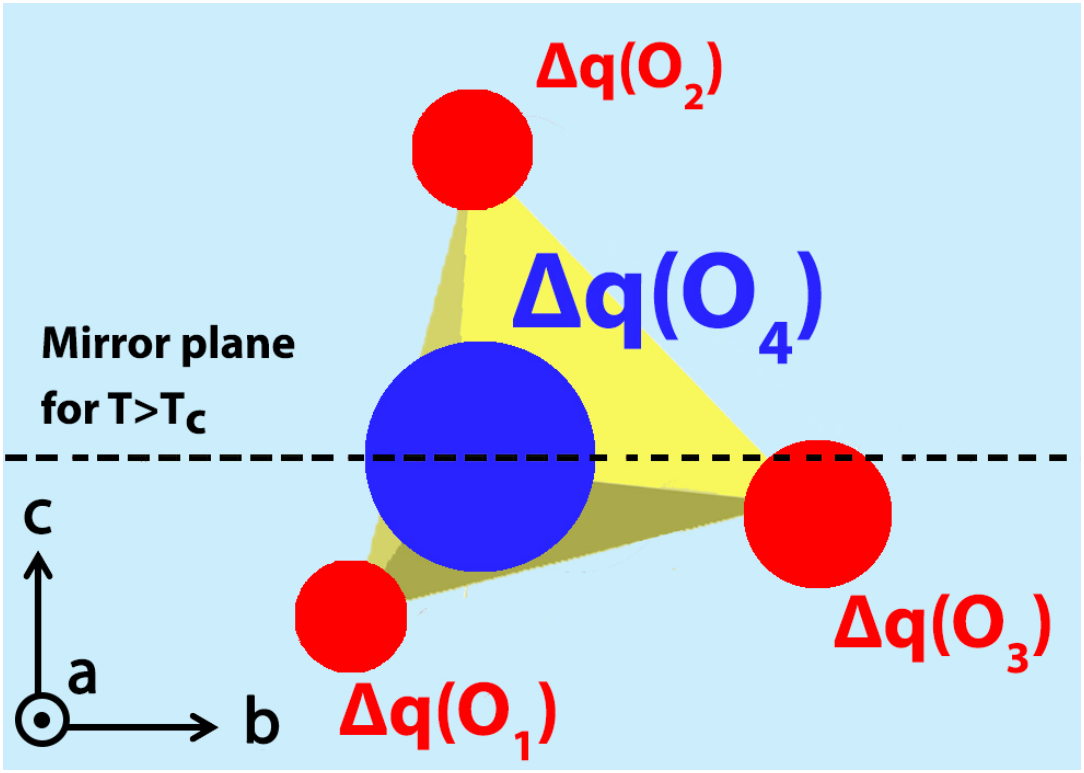

Figure 5.31: Detail of the charge modulation within the sulphate anion presented in Figure 5.30. It shows asymmetric charge translocations between the SO_3 group within the sulphate tetrahedra ($|\Delta q(O_1)| \neq |\Delta q(O_2)| < |\Delta q(O_3)|$) the O(4) atom, which in combination with the translocations observed in the $NH_4^+(I)$ cation, are the main responsible for the polarization dynamics.

This behaviour is described in a simplistic fashion for the sulphate anion, SO_4^{2-}, in the scheme in Figure. 5.31. In particular, the maximum amplitude of the oscillation of the charge transfer for the SO_3 groups (Fig. 5.11) is close to the sum of the maximum amplitude of the charge decrease on the $NH_4^+(I)$ cation and the O(4) atom. The other $NH_4^+(II)$ unit shows much more limited variations in its

associated charge transfer (Fig. 5.14).

Soft mode character of the low-frequency coherent oscillation

Another important question to be discussed is the soft mode character of the 0.36THz coherent oscillation. This behaviour is confirmed by certain features present in the oscillation corresponding to soft modes as previously discussed in Sec. 2.2.2:

- The analysis of the charge dynamics for photo-excited ferroelectric ammonium sulphate has revealed that part of the electronic charge density experiences relocations during the coherent lattice motions in the order of ≈100pm, which corresponds approximately to a chemical bond length, and are over 3 orders of magnitude larger than the displacements experimented by the nuclei (Fig. 5.12 to Fig. 5.14).

- The measurements of the variation of diffracted intensity for photoexcited ferroelectric ammonium sulphate conducted at 200K and at the substantially lower temperature of 110K (Figure 5.4) were significantly different. This suggests the existence of charge dynamics with frequency that is temperature-dependent as expected for a soft mode.

Polarization dynamics

The average electric field and polarization terms vanish on the a-b plane for symmetry reasons (Sec. 5.5, Fig. 5.25). This does not happen along the crystallographic c-axis, where there exists a permanent spontaneous electric field in the unexcited ferroelectric ammonium sulphate and where the polarization dynamics take place in the photoexcited crystal. The analysis of the transient charge density maps permits to decouple the total variation of polarization, $\Delta\mathbf{P}(t)$, into two terms: one corresponding to the vibration of the nuclei and the other to the electronic density displacements. When the two terms are compared it stands out that the contribution of the nuclei to the total variation of polarization is negligible in comparison to the contribution of the electronic displacements. This result confirms that the polarization dynamics in ferroelectric ammonium sulphate is dominated by the electronic charge translocations driven by the low-frequency 0.36THz soft mode-character modulation, which makes ammonium sulphate in this context, similar to displacive ferroelectric materials.

The derivation of the transient variation of polarization revealed an oscillation that in its maximum amplitude is close to the ground state spontaneous polarization at the experiment's temperature (T = 200K). The fact that the full reversal of polarity is absolutely dominated by the electronic currents gives evidence that the two phenomena are closely related.

It is important to remark that the work presented in this thesis focuses on the study of ultrafast fully-reversible charge dynamics for photoexcited ferroelectric ammonium sulphate in the vicinity of the phase transition, and does not explain the physics governing the para- to ferroelectric phase transition. The underlying phase transition processes are not fully understood, and most probably include other phenomena not considered here, e.g., tetrahedron tilting, ordering, entropy considerations regarding the thermal excitation of phonons, etc. An example, in this sense, is the fact that there exist differences in the ferroelectric transition between ammonium sulphate and deuterated ammonium sulphate ([69]). This indicates that the hydrogen atoms must play a role, even if a minor one, whereas in the model proposed in Section 5.3 it is assumed that the hydrogen atoms in a NH_4^+ cation are located at a constant separation of the nitrogen nucleus and will follow its movement readily. Also, it has already been proven that a description of the phase transition must necessarily take the anharmonicity of ammonium ions into account ([87]).

Low-frequency phonon excitation mechanism

With respect to the mechanisms that can potentially induce the 0.36THz coherent oscillation with soft mode character (Sec.5.4), the observed delay of ∼2-3ps in the outset of the variations of X-ray diffracted intensity, $\Delta I_{hkl}(t)/I^0_{hkl}$, (Fig. 5.2 and Fig 5.4) suggests a preponderance of the mechanism *indirect excitation via anharmonic phonon-phonon interaction* in contrast to the mechanism *direct displacive excitation*, which takes place almost instantaneously.

This mechanism corresponds to the intra-band relaxation of photoexcited carriers by means of electron-phonon scattering. The incoherent cooling takes place, while the temperature in the material increases, and it is this non-equilibrium state which, in general, produces an impulsive stress that generates the coherent acoustic phonon wave packets. Since it is governed by the relaxation kinetics, it takes place after a certain time delay that is, typically, in the order of a few picoseconds.

Fast dephasing of the observed 0.36THz coherent oscillation with soft mode character

The quick dephasing and dampening of the 0.36THz coherent oscillation with soft mode character is discussed now. As can be appreciated in the experimental transient measurements (Fig 5.4 to Fig. 5.14), these charge modulations are strongly damped on a time scale of a few picoseconds, and hardly reach two cycles before complete oscillation dampening. This phenomenon is related to the fact that the frequencies of infrared-active phonons in a disordered powder sample undergo inhomogeneous broadening compared to those measured in single crystals ([217], and Supplemental Material of [218]). For phonons with wavelengths much larger than the size of a crystallite (wavelengths in the $q \to 0$ limit), the phonon frequency depends on the relative orientation between the *phonon transition dipole* and the physical shape of the crystallite, i.e., the coupling to an external electric field depends on the orientation of the *phonon transition dipole* with respect to the applied field.

In the Figure 5.32, it is graphically indicated how the phonon frequency depends on the relative orientation of the soft mode dipole (black arrows) with respect to the symmetry axis of each crystal. The depolarization field, which is generated by the surface charges that appear during the phonon's oscillation period, furthermore influences the frequency of those phonons that are connected to a homogeneous polarization in the crystallite. For example, in the case of a soft mode polarization oriented in parallel to the symmetry-axis of a prolate-shaped crystal, the transverse optical (TO) version of that phonon is measured. Contrarily, in the case of a soft mode polarization that is oriented in parallel to the symmetry-axis of an oblate-shaped crystal, the measured frequency corresponds to the longitudinal optical (LO) version of that polar phonon. In this sense, a powder of compacted crystallites, corresponds to a random distribution of crystallite shapes (size is estimated at less than 10 microns), which gives rise to a continuous distribution of frequencies between the transversal and longitudinal optical infrared active phonons. In the particular case of soft modes, there exists a longitudinal and transversal optic splitting that is in the order of the longitudinal optic frequency which renders them very sensitive to this effect.

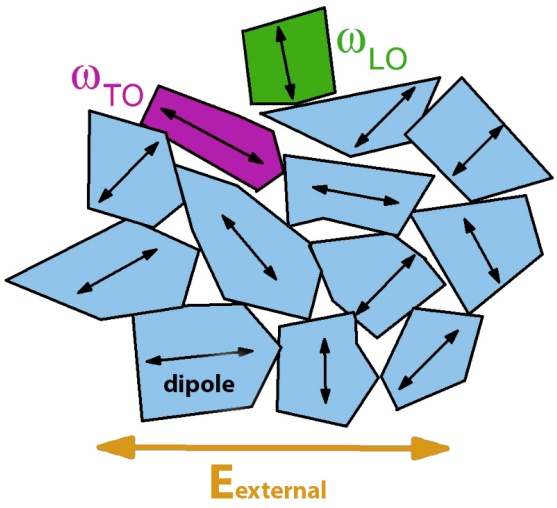

Figure 5.32: The strong dampening of the soft mode oscillations is an acknowledged circumstance for powder crystallite samples ([218]). The coupling depends on the relative orientation of the externally applied electric field with respect to the phonon transition dipole: for an oblate crystallite (green), the phonon appears at ω_{LO}, and for a prolate crystallite (magenta) it appears at ω_{TO}.

After an initial in-phase excitation of the phonon distribution, each phonon develops in time according to its particular frequency, and this results in a temporal spreading and dampening of the wavepacket on a few-picosecond time scale. Beyond this behaviour, there can also exist other different non-equilibrium mechanisms that induce an efficient de-phasing of coherent phonon oscillations. For example, carrier relaxation eventually generates excess incoherent low-frequency phonons. Part of such phonons populate states that contribute to the coherent oscillations which is why this effect destroys the phase of quantum coherences and dampens the oscillations. Furthermore, the redistribution of electronic charge density relates to an electronic friction (or current) term that reduces the amplitude of coherent lattice motions.

Summary

In this thesis, the ultrafast charge, lattice and polarization dynamics in photoexcited ferroelectric ammonium sulphate were studied with the help of femtosecond X-Ray powder diffraction. A newly prepared powder sample of the prototype material was electronically excited every experiment day via 3-photon absorption upon illumination of a 70fs-pump pulse with center wavelength of 400nm at a temperature of 200K. To study non-equilibrium dynamics, the transient variation of X-Ray diffracted intensity, $\Delta I_{hkl}(t)/I^0_{hkl}$, which results from the interaction of the photoexcited sample and the X-Ray probe was measured. Given the low flux that the X-Ray source generates in the experimental set-up, it is necessary to accumulate experimental data over a number of days to achieve measurements with sufficiently high signal-to-noise ratio. Subsequently, the maximum entropy method was applied to all the collected data to reconstruct the transient charge density, $\Delta\rho(\mathbf{r},t)$.

The analysis of the resulting charge density maps in the unit cell of photoexcited ferroelectric ammonium sulphate has revealed pronounced electronic charge density modulations. It was observed that all major charge translocations were centered on the original atomic positions and that there was no charge transfer to previously unoccupied regions in space, which confirms the preservation of the ferroelectric lattice structure under photoexcitation. The electronic charge density translocations were identified as a newly-discovered low-frequency coherent oscillation with a period of approximately $\sim$3ps (i.e., 0.36 THz). It is characterised by shifting electronic charge within the sulphate anions (SO_4^{2-}) in a remarkably anisotropic way: one oxygen atom shows an oscillatory increase/decrease of charge density, while the sulphur atom and the other three oxygen atoms react exactly in the opposite way. In addition, there is a net charge transfer between the SO_4^{2-} units and some ammonium ions, NH_4^+, which enhances the local polarization in the crystal lattice compared with the unexcited equilibrium structure. The outcome of the experiment on ferroelectric ammonium sulphate is in striking contrast to the behavior of the transient electronic density in paraelectric ammonium sulphate at room temperature, where a concerted electron and proton transfer into a channel-like geometry along the c-axis was discovered in a previous research ([7]).

The assessment of the charge density maps also revealed comparatively minute sub-picometer relocations of the nuclei which display an analogous evolution to that of the electronic charge density. The electronic charge displacements, however, reach much larger distances in the order of $\approx$100pm, i.e., approximately the typical length of a chemical bond. Also, additional measurements of the transient variation of the diffracted intensity, $\Delta I_{hkl}(t)/I^0_{hkl}$, where accomplished at a substantially lower temperature of 100K with significantly different results from those accomplished at 200K which suggests the existance of temperature-dependent charge dynamics. These features indicate a soft mode character in the newly-discovered low-frequency coherent oscillation, in agreement with the qualitative predictions of Cochran's theory ([20, 21]). The excitation of a coherent oscillation in a crystalline material can be induced by different mechanisms. Given the fact that the electron charge density translocations reach its maximum amplitude after 2-3ps upon excitation, it can be stated that the predominant mechanism for ferroelectric ammonium sulphate is the so-called *indirect displacement excitation*. This phenomenon is characterised by the fact that after the initial electronic excitation via 3-photon absorption, the ensuing electronic relaxation leads to a delayed onset of the phonon excitation, which typically is in the order of

up to a few picoseconds, in contrast to the other relevant mechanism, the so-called *direct displacement excitation*, that takes place almost instantaneously.

Comprehensive theoretical work by Resta and others has demonstrated that the classical macroscopic polarization in a crystal, **P**, is ill-defined and cannot be derived uniquely from the knowledge of static charge distributions ([9–11]). In this sense, the crucial magnitude is the *variation of polarization* between two different states of the crystal, $\Delta\mathbf{P}$. In the case of ferroelectric ammonium sulphate, out of lattice symmetry reasons, the variation of polarization is restricted to the c-axis. In addition, the analysis of the transient charge density maps permits to decouple the movement of the nuclei and the electronic charge in a good approximation to the Clausius-Mossoti model ([48, 49]) with which the expression for the transient variation of polarization can be separated into two terms, $\Delta\mathbf{P}(\mathrm{t}) = \Delta\mathbf{P}_{c-axis}(\mathrm{t}) = \Delta\mathbf{P}^{electron}_{c-axis}(\mathrm{t}) + \Delta\mathbf{P}^{nuclei}_{c-axis}(\mathrm{t})$, which correspond to the electronic and nuclear contributions, respectively.

By studying independently the terms $\Delta\mathbf{P}^{electron}_{c-axis}(\mathrm{t})$ and $\Delta\mathbf{P}^{nuclei}_{c-axis}(\mathrm{t})$, it was observed that the nuclear contribution is approximately 30 times smaller than the electronic contribution, which is in line with the experimental finding that the oscillation amplitudes of the nuclei are approximately 3 orders of magnitude smaller than the typical electronic charge displacements. In this context, the nuclear contribution can be neglected, and the transient variation of macroscopic polarization, $\Delta\mathbf{P}(\mathrm{t})$, was derived considering only the electronic contribution. The result is that $\Delta\mathbf{P}(\mathrm{t})$ displays a distinct oscillatory modulation in time. While the orientation of $\Delta\mathbf{P}(\mathrm{t})$ in the crystal structure has remained unknown (i.e., the sign of $\Delta\mathbf{P}(\mathrm{t})$ relative to the c-axis has remained uknown, [69]), the maximum amplitude of the transient variation of polarization slightly exceeds the magnitude of the full spontaneous polarization for the unexcited ferroelectric ammonium sulphate at $\mathrm{T} = 200\mathrm{K}$, $|\Delta\mathbf{P}(\mathrm{t})|\ (\mathrm{T} = 200\mathrm{K}) \approx \mathbf{P}_S^{unexcited}\ (\mathrm{T} = 200\mathrm{K})$. This behaviour ensures that the macroscopic polarization is fully reversed at some time during the photoexcitation of the ferroelectric ammonium sulphate.

In conclusion, the outcome of the experiment demonstrates the high potential of ultrafast X-Ray powder diffraction to derive time-resolved charge density maps for ferroelectrics upon photoexcitation, and permits establishing a direct link between transient microscopic charge density variations and the ultrafast dynamics of macroscopic polarization.

Future work will contemplate the determination of the transient variation of polarization in the general non-Claussius-Mossotti case within the proper theoretical framework by means of the experimentally derived charge density maps, and some steps have already been taken in that direction ([16]). Such findings will permit a benchmarking of the ab-initio quantum theory for ferroelectrics, that shall allow for the tailoring of ferroelectric solids for a wide range of devices, e.g., switching applications characterized by ultra-high processing speed.

On a different aspect, this type of experiment is very time-consuming due to the low-flux X-Ray produced by the sources. It is planned to solve this shortcoming in the near future with the design and development of new mid-infrared driver lasers ([219, 220]). Initial experiments and theoretical calculations predict that this will yield a flux larger by at least one order of magnitude, thus, reducing experimental time ([171, 179]).

Bibliography

[1] M. Lines and A. Glass. *Principles and applications of ferroelectrics and related materials.* Clarendon Press, Oxford, 1979.

[2] M. Dawber, K. M. Rabe, and J. F. Scott. *Rev. Mod. Phys., 77, 1083–1130, 2005.*

[3] J. F. Scott. *Science, 315, 954-959, 2007.*

[4] C. Chen, H. Deng, X. Li, H. Zhang, T. Huang, D. Lin, S. Wang, X. Zhao, Z. Hu, and H. Luo. *Appl. Phys. Lett., 105, 102909, 2014.*

[5] A. Sawada, Y. Takagi, and Y. Ishibashi. *J. Phys. Soc. Jpn., 34, 748–754. 1973.*

[6] A. Basu, R. Jana, G. Mandal, A. Chandra , and G. D. Mukherjee. *J. Appl. Phys., 117, 054102, 2015.*

[7] M. Woerner, F. Zamponi, Z. Ansari, J. Dreyer, B. Freyer, M. Premont-Schwarz, and T. Elsaesser. *J. Chem. Phys., 133, 064509, 2010.*

[8] C. Hauf, A.-A. Hernández, M. Holtz, M. Woerner, and T. Elsaesser. *Structural Dynamics, 5, 024501, 2018.*

[9] R. Resta. *Ferroelectrics, 151, 49-58, 1994.*

[10] R. M. Martin. *Phys. Rev. B, 9, 1998–1999, 1974.*

[11] R. Resta. *Rev. Mod. Phys., 66, 899–915, 1994.*

[12] R. Resta, M. Posternak, and A. Baldereschi. *Phys. Rev. Lett., 70, 1010-1013, 1993.*

[13] D. Vanderbilt and R. D. King-Smith. *Phys. Rev. B, 48, 4442–4455, 1993.*

[14] N. A. Spaldin. *J. Solid State Chem., 195, 2-10, 2012.*

[15] M. V. Berry. *Proc. R. Soc. Lond. A, 392,45-57, 1984.*

[16] C. Hauf, M. Woerner, and T. Elsaesser. *Phys. Rev. B, 98, 054306, 2018.*

[17] F. Chen. *Phys. Rev. B, 94, 180104, 2016.*

[18] R. Mankowsky, A. von Hoegen, M. Foerst, and A. Cavalleri. *Phys. Rev. Lett., 118, 197601, 2017.*

[19] M. Kozina, T. van Driel, M. Chollet, T. Sato, J. M. Glownia, S. Wandel, M. Radovic, U. Staub, and M. C. Hoffmann. *Struct. Dyn., 4, 054301, 2017.*

[20] W. Cochran. *Phys. Rev. Lett., 3, 412-414, 1959.*

[21] W. Cochran. *Adv. Phys., 9, 387–423, 1960.*

[22] C. Rose-Petruck, R. Jimenez, T. Guo, A. Cavalleri, C. W. Siders, F. Rksi, J. A. Squier, B. C. Walker, K. R. Wilson and C. P. J. Barty. *Nature volume, 398, 310-312, 1999.*

[23] M. Bargheer, N. Zhavoronkov, Y. Gritsai, J. C. Woo, D. S. Kim, M. Woerner, and T. Elsaesser. *Science, 306, 1771-1773, 2004.*

[24] T. Elsaesser and M. Woerner. *J. Chem. Phys., 140, 020901, 2014.*

[25] M. Woerner, M. Holtz, V. Juve, T. Elsaesser, and A. Borgschulte. *Faraday Discuss, 171, 373–392, 2014.*

[26] J. Stingl, F. Zamponi, B. Freyer, M. Woerner, T. Elsaesser, and A. Borgschulte. *Physical Review Letters, 109, 147402, 2012.*

[27] T. Kubacka, J. A. Johnson, M. C. Hoffmann, C. Vicario, S. de Jong, P. Beaud, S. Grbel, S.-W. Huang, L. Huber, L. Patthey, Y.-D. Chuang, J. J. Turner, G. L. Dakovski, W.-S. Lee, M. P. Minitti, W. Schlotter, R. G. Moore, C. P. Hauri, S. M. Koohpayeh, V. Scagnoli, G. Ingold, S. L. Johnson, and U. Staub. *Science, 343, 1333-1336, 2014.*

[28] V. Esposito, M. Fechner, R. Mankowsky, H. Lemke, M. Chollet, J. M. Glownia, M. Nakamura, M. Kawasaki, Y. Tokura, U. Staub, P. Beaud, and M. Först. *Phys. Rev. Lett., 118, 247601, 2017.*

[29] F. Zamponi, P. Rothhardt, J. Stingl, M. Woerner, and T. Elsaesser. *Proc. Natl. Acad. Sci. (PNAS), 109, 5207-5212, 2012.*

[30] W. Känzig. Ferroelectrics and antiferroelectrics. *Academic Press (1957).*

[31] C. H. Ahn, K. M. Rabe, M. Dawber, C. Lichtensteiger and J.-M. Triscone. *Topics in Applied Physics, 105, 1-30, 2007.*

[32] P. Paruch, T. Giamarchi, T. Tybell, and J.-M. Triscone. *Journal of Applied Physics, 100, 051608, 2006.*

[33] C. Kittel. Festkörperphysik. *Oldenbourg Verlag, 14th edition, 2005.*

[34] O. D. Jefimenko and D. K. Walker. *Physics Teacher, 18, 651–659, 1980.*

[35] S. Hoshino, K. Vedam, Y. Okaya, and R. Pepinsky. *Phys. Rev.,112, 405–412, 1958.*

[36] C. B. Sawyer and C. H. Tower. *Phys. Rev., 35, 269, 1930.*

[37] I. Farnan, M. Dawber and J. F. Scott. *Am. J. Phys., 71, 819, 2003.*

[38] J. M. Perez-Mato, M. Aroyo, A. Garcia, P. Blaha, K. Schwarz, J. Schweifer, and K. Parlinski. *Phys. Rev. B, 70, 214111, 2004.*

[39] B. B. van Aken, T. T. Palstra, A. Filippetti, N. A. Spaldin. *Nature Mater., 3, 164, 2004.*

[40] M. Fiebig. *J. Phys. D, 38, R123, 2005.*

[41] W. Eerenstein, N. D. Mathur, J. F. Scott. *Nature, 442, 759, 2006.*

[42] T. Tybell, C. H. Ahn, J.-M. Triscone. *Appl. Phys. Lett., 75, 856, 1999.*

[43] T. Mitsui, S. Nomura, M. Adachi, J. Harada, T. Ikeda, E. Nakamura, E. Sawaguchi, T.Shigenari, Y. Shiozagi, J. Tatsuzaki, K. Toyoda, T. Yamada, K. Gesi, Y. Marita, M. Marutake, T. Shiosaki, and K. Wakino. Oxides, Landolt–Börnstein: Numerical data and functional relationships in science and technology (group iii, vol. 16, part a). *Springer, Berlin, 1981.*

[44] T. Mitsui, S. Nomura, M. Adachi, J. Harada, T. Ikeda, E. Nakamura, E. Sawaguchi, T.Shigenari, Y. Shiozagi, J. Tatsuzaki, K. Toyoda, T. Yamada, K. Gesi, Y. Marita, M. Marutake, T. Shiosaki, and K. Wakino. Oxides, Landolt–Börnstein: Numerical data and functional relationships in science and technology (group iii, vol. 28). *Springer, Berlin, 1981.*

[45] J. Valasek. *Physical Review., 15, 537, 1920.*

[46] A. von Hippel. U.S. national defense research committee (ndrc) report 300. *Boston (MA). 1944.*

[47] J. F. Scott, C. A. Araujo. *Science, 246, 1400, 1989.*

[48] M.L. Cohen. Electronic materials (p. 57). *Springer, Berlin, 1991.*

[49] R.E. Cohen, and H. Krakauer. *Phys. Rev. B, 42, 6416, 1990.*

[50] R. E. Cohen. *Nature, 358, 136, 1992.*

[51] C. Kittel. *Phys. Rev., 82, 729–732, 1951.*

[52] Compendium of chemical terminology: Gold book. *International Union of Pure and Applied Chemistry. 2014.*

[53] C. V. Raman and T. M. K. Nedungadi. *Nature, 145, 147, 1940.*

[54] R. Blinc. *Ferroelectrics, 74, 301-303, 1987.*

[55] S. C. Power. *Proc. Comb. phil. Soc., 38, 62, 1942.*

[56] H. Frohlick. Theory of dielectrics (p. 159). *Claredon Press, Oxford, 1949.*

[57] R. Lyddane, R. Sachs, and E. Teller. *Phys. Rev., 59, 673, 1941.*

[58] M. Born and K. Huang. Dynamical theory of crystal lattices. *Clarendon Press, Oxford, 1954.*

[59] A. D. B. Woods, W. Cochran, and B. N. Brockhouse. *Phys. Rev. 119, 980, 1960.*

[60] B. N. Brockhouse and P. K. Iyengar. *Phys. Rev., 111, 747, 1958.*

[61] A. S. Barker, Jr. and M. Tinkham. *Phys. Rev., 125, 1527, 1962.*

[62] R. A. Cowley. *Phys. Rev. Lett., 9, 159, 1962.*

[63] R. A. Cowley. *Phys. Rev. 134, A981, 1964.*

[64] J. Petzelt, J. Grigas, and I. Mayerova. *Ferroelectrics, 6, 225–234, 1974.*

[65] J. F. Scott. *Reviews of Modern Physics, 46, 83, 1974.*

[66] R. A. Cowley. *Advances in Physics, 12, 421–480, 1963.*

[67] G. Venkataraman. *Bull. Mater. Sci., 1, 129-170, 1979.*

[68] J. C. Slater. *J. Chem. Phys., 9, 16, 1941.*

[69] H.-G. Unruh and U. Rudiger. *J. Phys. Colloq., 33, 77-78, 1972.*

[70] W. G. Stirling. *J. Phys. C, 5, 2711, 1972.*

[71] S. Kwon and J. Kim. *J. Phys. Condens. Matter, 2, 10607–10613, 1990.*

[72] B. Torrie, C. Lin, S. Binbrek, and A. Anderson. *J. Phys. Chem. Solids, 33, 697–709, 1972.*

[73] N. W. Ashcroft, and N. D. Mermin. Solid state physics. *Cornell University, 1976.*

[74] M. Born und R. Oppenheimer. *Annalen der Physik, 84, 457-484, 1927.*

[75] D. Lide. The crc handbook of chemistry and physics (pp. 12–17). *The Chemical Rubber Publishing Company, 1998.*

[76] C. Kittel. Introduction to solid state physics. *Wiley, 2005.*

[77] R. W. Boyd. Handbook of laser technology and applications (three-volume set), nonlinear optics (ch. 3, pp. 161–183). *Taylor and Francis, 2003.*

[78] R. Resta and D. Vanderbilt. *Theory of Polarization: A Modern Approach. Physics of Ferroelectrics. Topics in Applied Physics (p. 105).*, Springer, Berlin, 2007.

[79] S. Baroni, P. Giannozzi, and A. Testa. *Phys. Rev. Lett., 58, 1861–1864, 1987.*

[80] R. Resta. *Europhysics Letters, 22, 133-138, 1993.*

[81] M. Born. *Z. Phys., 40, 167, 1926.*

[82] M. Born. *Z. Phys., 51, 165, 1928.*

[83] M. Woerner F. Zamponi, J. Stingl and T. Elsaesser. *Phys. Chem. Chem. Phys., 14, 6156, 2012.*

[84] C. Hauf, A.-A. Hernández, M. Holtz, M. Woerner, and T. Elsaesser. *Struct. Dyn., 6, 014503, 2019.*

[85] D. R. Lide. Crc handbook of chemistry and physics. *CRC Press., Boca Raton (FL.), 2006.*

[86] K.-H. Zapp. Ammonium Compounds in Ullmann's Encyclopedia of Industrial Chemistry. *Wiley-VCH, Weinheim, 2012.*

[87] L. S. Smirnov. *Journal of the Korean Physical Society, 32, 98-102, 1998.*

[88] A. Onodera, O. Cynshi, and Y. Shiozaki. *J. Phys. C (Solid State Phys.), 18, 2831, 1985.*

[89] A. T. Anistratov and V. G. Martynov. *Sov. Phys. Cryst., 15, 256, 1970.*

[90] R. Blinc and I. Levstek. *J. Phys. Chem. Solids, 12, 295, 1960.*

[91] T. Chiba. *J. Chem. Phys., 36, 1122, 1962.*

[92] D. E. O'Reilly and T. Tsang. *J. Chem. Phys., 46, 1291, 1967.*

[93] N. Shibata, R. Abe, and I. Suzuki. *J. Phys. Soc. Japan, 41, 2011, 1976.*

[94] R. Abe and N. Shibata. *J. Phys. Soc. Japan, 43, 1308, 1977.*

[95] M. Fujimoto, L. A. Dressel, and T. J. Yu. *J. Phys. Chem. Solids, 38, 97, 1977.*

[96] K. Hirabayashi and R. Abe. *J. Phys. Soc. Japan, 48, 520, 1980.*

[97] G. Kozlov, S. Lebedev, A. Volkov, J. Petzelt, B. Wyncke, and F. Brehat. *J. Phys. C: Solid State Phys., 21, 4883–4894, 1988.*

[98] Z. Iqbal and C. W. Christoe. *Ferroelectrics, 12, 177, 1976.*

[99] H. G. Unruh and O. Ayere. *Ferroelectrics, 12, 181, 1976.*

[100] S.-B. Kwon and J. J. Kim. *J. Phys.: Condens. Matter, 2, 10607, 1990.*

[101] P. Venkateswarlu, H. Bist, and Y. Jain. *J. Raman Spectrosc., 3, 143–151, 1975.*

[102] E. O. Schlemper and W. C. Hamilton. *J. Chem. Phys., 44, 4498, 1966.*

[103] K. Hsebe. *J. Phys. Soc. Japan, 50, 1266, 1981.*

[104] S. Ahmed, A. Shamah, K. Kamel, and Y. Badr. *Phys. Status Solidi A, 99, 131–140, 1987.*

[105] U. Dahlborg, K. E. Larsson, and E. Pirkmajer. *Physica, 49, 1, 1970.*

[106] J. J. Rush and T. I. Taylor. *Inelastic Neutron Scattering in Solids and Liquids (IAEA, Vienna), II, 33-345, 1965.*

[107] A. Bajorek, T. Matchekhina, and K. Parlinski. *Inelastic Neutron Scattering in Solids and Liquids (IAEA, Vienna), 2, 355-381, 1965.*

[108] H. J. Kim, P. S. Goyal, G. Venkataraman, B. A. Dasannacharya and C. L. Taper. *Solid State Commun., 8, 889, 1970.*

[109] P. P. Chandra, B. A. Dasannacharya, P. S. Goyal, P. K. Iyengar, K. R. Rao, C. L. Thaper and A. H. Venkatesh. *Phys. Lett., 57, 463, 1976.*

[110] P. S. Goyal and B. A. Dasannachary. *J. Chem. Phys., 68, 2430, 1978.*

[111] P. S. Goal, R. Chakravarthy, B. A. Dasannacharya and C. J. Carlile. *Phys. Stat. Sol. (A), 118, 425, 1990.*

[112] H. Unruh, E. Sailer, H. Hussinger, and O. Ayere. *Solid State Commun., 25, 871–874, 1978.*

[113] V. V. Udalova and Z. G. Pinsker. *Kristallografiya, 8, 538, 1963.*

[114] S. Ahmed, A.M. Shamah, A. Irrahim, and F. Hanna. *Phys. Stat. Sol. (A), 115, 149, 1989.*

[115] T. Ikeda, K. Fujibayashi, T. Nagai, and J. Kobayashi. *Phys. Stat. Sol. (A), 16, 279, 1973.*

[116] D. Swain and T. N. Guru Row. *Inorg. Chem., 46, 4411, 2007.*

[117] A. V. Desyatnichenko, A. P. Shamshin, and E. V. Matyushkin. *Ferrolelectrics, 307, 213, 2004.*

[118] A. Sawada, S. Ohya, and Y. Ishibashi. *J .Phys. Soc. Japan, 38, 1408, 1975.*

[119] B. T. Matthias, and J. P. Remeika. *Phys. Rev., 103, 262, 1956.*

[120] T. Hahn (Editor). Space-group symmetry band a in international tables for crystallography. *International Union of Crystallography, Chester, 2006.*

[121] T. Hahn (Editor). International tables for crystallography, volume a: Space-group symmetry. *Wiley, Chester, 2005.*

[122] W. Massa. Crystal structure determination. *CRC Press, Springer-Verlag, Berlin, (2004).*

[123] D. Schwarzenbach. Kristallographie. *Springer Verlag, Berlin, 2001.*

[124] C. H. Shomate. *J. Am. Chem. Soc., 67, 1096, 1945.*

[125] I. Nitta and K. Suenaga. *Bull. Chem. Soc. Japan, 13, 36, 1938.*

[126] B. Freyer, J. Stingl, F. Zamponi, M. Woerner, and T. Elsaesser. *Optics Express, 19, 15511, 2011.*

[127] H. Ibach and H. Lüth. Solid-state physics: An introduction to principles of materials science. *Springer, Berlin, 2009.*

[128] W. Demtroeder. Experimentalphysik 3: Atome, Moleküle und Festkörper. *Springer, Berlin, 2010.*

[129] J. Als-Nielsen, D. McMorrow. Elements of modern x-ray physics. *Wiley Pulishers, Berlin, 2011.*

[130] P. P. Ewald. *Physikalische Zeitschrift, 14, 465–472, 1913.*

[131] B. E. Warren. X-ray diffraction. *Dover Publications, New York. 1990.*

[132] P. Debye and P. Scherrer. Interferenzen an regellos orientierten teilchen im röntgenlicht i. *Nachrichten von der Gesellschaft der Wissenschaften zu Göttingen, 1916, 1-15, 1916.*

[133] A. Maksimchuk, S.-y. Chen and D. Umstadter. *Nature, 396, 653–655, 1998.*

[134] O. Klein and Y. Nishina. *Nature, 122, 398–399, 1928.*

[135] A. Compton. Secondary radiations produced by x-rays, and some of their applications to physical problems (bulletin of the national research council, n. 20.). *National Research Council of the National Academy of Sciences,Washington, D.C., 1922.*

[136] A. Compton. *Physical Review, 21, 483–502, 1923.*

[137] Efficiency of XR-100T-CdTe detectors, 2010. http://www.amptek.com/anczt1.html.

[138] D. Meschede. Gerthsen physik. *Springer, Berlin, 2006.*

[139] P. Auger. *Journal de Physique et Le Radium, 6, 205–208, 1925.*

[140] L. Meitner. *Zeitschrift fuer Physik, 11, 35-54, 1922.*

[141] H. Hertz. *Annalen der Physik, 267(8), 983-1000, 1887.*

[142] A. Einstein. *Annalen der Physik, 322, 132–148, 1905.*

[143] A. Thompson, D. Attwood, E. Gullikson, M. Howells, J. Kortright, A. Robinson, J. Underwood, K. Kim, J. Kirz, I. Lindau, P. Pianetta, H. Winick, G. Williams, and J. Scofield. X-ray data booklet. *Lawrence Berkeley National Laboratory, Berkely, 2009.*

[144] J. H. Hubbell. *Radiation Physics and Chemistry, 75, 614–623, 2006.*

[145] *Lord Rayleigh (John Strutt) refined his theory of scattering in successive works in the 1870s and 1880s, the most important of those papers are cited here:*
J. Strutt. On the light from the sky, its polarization and colour. Philosophical Magazine, 41, 107–120 and 274–279, 1871.
J. Strutt . On the scattering of light by small particles. Philosophical Magazine, 41, 447–454, 1871.
J. Strutt. On the electromagnetic theory of light. Philosophical Magazine, 12, 81–101, 1881.
J. Strutt . On the transmission of light through an atmosphere containing small particles in suspension, and on the origin of the blue of the sky. Philosophical Magazine, 47, 375–394, 1899.

[146] National Institute of Standards and Technology: Graph data comes from the database of NIST's XCOM. https://www.nist.gov.

[147] K. Kleinknecht. Detektoren für Teilchenstrahlung. *Springer, Berlin, 2005.*

[148] O. Klein and Y. Nishina. *Zeitschrift fuer Physik, 52, 853–868, 1929.*

[149] R. W. James. The optical principals of the x-ray diffraction. *Ox Bow Press, Woodbridge (CT) , 1962.*

[150] F. Zamponi, Z. Ansari, M. Woerner, and T. Elsaesser. *Optics Express, 18, 947-961, 2010.*

[151] V. Juvé, M. Holtz, F. Zamponi, M. Woerner, T. Elsaesser and A. Borgschulte. *Phys. Rev. Lett., 111, 217401, 2013.*

[152] S. Smaalen, L. Palatinus, and M. Schneider. *Acta Cryst. Sect. A, 59, 459-469, 2003.*

[153] L. Palatinus. Maximum entropy method in superspace crystallography, phd thesis, university of bayreuth, germany, 2003.

[154] H. C. Kapteyn. *Review of Scientific Instruments, 69, 1207–1223, 1998.*

[155] D. Strickland and G. Mourou. *Optics Communications, 56, 219–221, 1985.*

[156] F. Zamponi, Z. Ansari, C. v. Korff Schmising, P. Rothhardt, N. Zhavoronkov, M. Woerner, T. Elsaesser, M. Bargheer, T. Trobitzsch-Ryll, and M. Haschke. *Appl. Phys. A, 96, 51–58, 2009.*

[157] T. Brabec, Ch. Spielmann, P. Curley, and F. Krausz. *Optics Letters, 17, 1292–1294, 1992.*

[158] D. Spence, P. Kean, and W. Sibbett. *Optics Letters, 16, 42-44, 1991.*

[159] A. Rousse, C. Rischel, and J.-C. Gauthier. *Reviews of Modern Physics, 73, 17–31, 2001.*

[160] C. Rullière. Femtosecond laser pulses principles and experiments. *Springer, Berlin, 2004.*

[161] Spectra-physics tsunami mode-locked ti:sapphire laser user's manual. Tsunami mode-locked ti:sapphire laser manual. . (last opened june, 2019).

[162] Spectra-physics empower intracavity-doubled, diode-pumped nd:ylf laser system. *Spectra-Physics Empower User Manual. (last opened April, 2019).*

[163] E. Treacy. *Journal of Selected Topics in Quantum Electronics, 5, 454–458, 1969.*

[164] O. Martinez, J. Gordon, and R. Fork. *Journal of the Optical Society of America A, 1, 1003–1006, 1984.*

[165] J. Itatani, J. Faure, M. Nantel, G. Mourou, and S. Watanabe. *Optics Communications, 148, 70–74, 1998.*

[166] M. Nantel, J. Itatani, T. An-Chun, J. Faure, D. Kaplan, M. Bauvier, T. Buma, P. Van Rompay, J. Nee, P. P. Pronko, D. Umstadter, and G. A. Mourou. *Journal of Selected Topics in Quantum Electronics, 4, 449–458, 1998.*

[167] M. P. Kalashnikov, E. Risse, H. Schönnagel, and W. Sandner. *Optics Letters, 30, 923–925, 2005.*

[168] T. Kobayashi, J. Liu, K. Okamura, and Y. Kida. *Optics Express, 18, 22245–22254, 2010.*

[169] N. Zhavoronkov, Y. Gritsai, G. Korn, and T. Elsaesser. *Applied Physics, 79, 663–667, 2004.*

[170] N. Zhavoronkov and G. Korn. *Optics Letters, 29, 198–200, 2004.*

[171] J. Weisshaupt, V. Juvé, M. Holtz, S. Ku, M. Woerner, T. Elsaesser, S. Ališauskas, A. Pugzlys and A. Baltuška. *Nature Photonics, 8, 927-930, 2014.*

[172] M. Holtz, C. Hauf, J. Weisshaupt, A. A. Hernández Salvador, M. Woerner, and T. Elsaesser. *Structural Dynamics, 4, 054304, 2017.*

[173] R. Loudon. The quantum theory of light (chap. 5.). *Oxford University Press, Oxford. 2000.*

[174] T. Auguste, P. Monot, L. Lompre, G. Mainfray, and C. Manus. *Optics Communications, 89, 145–148, 1992.*

[175] M. Bargheer, N. Zhavoronkov, R. Bruch, H. Legall, H. Stiel, M. Woerner, and T. Elsaesser. *Applied Physics B, 80, 715–719, 2005.*

[176] B. L. Henke, E. M. Gullikson, and J. C. Davis. *Atomic Data and Nuclear Data Tables, 54, 181-342, 1993.*

[177] Dupont kapton polyimide films. .
Kapton polyimide film.. (last opened june, 2019).

[178] S. Yalunin, M. Gulde, and C. Ropers. *Physical Review B, 84, 195426, 2011.*

[179] J. Weisshaupt, V. Juvé, M. Holtz, M. Woerner, and T. Elsaesser. *Structural Dynamics, 2, 024102, 2015.*

[180] F. Brunel. *Physical Review Letters, 59, 52–56, 1987.*

[181] G. Andriukaitis, T. Balciunas, S. Alisauskas, A. Pugzlys, A. Baltuska, T. Popmintchev, M.-C. Chen, M. Murnane, and H. Kapteyn. *Optics Letters, 36, 2755-2757, 2011.*

[182] T. Popmintchev, M.-C. Chen, D. Popmintchev, P. Arpin, S. Brown, S. Alisauskas, G. Andriukaitis, T. Balciunas, O. Mücke, A. Pugzlys, A. Baltuska, B. Shim, S. Schrauth, A. Gaeta, C. Hernández-García, L. Plaja, A. Becker, A. Jaron-Becker, M. Murnane, and H. Kapteyn. *Science, 336, 1287–1291, 2012.*

[183] D. V. Davis, V. D. Mistry, and C. A. Quarles. *Physics Letters A, 38, 169-170, 1972.*

[184] D. Berenyi, G. Hock, S. Ricz, B. Schlenk, and A. Valek. *Journal of Physics B, 11, 709, 1978.*

[185] W. Demtroeder. Experimentalphysik 2: Elektrizitaet und optik. *Springer, Berlin, 2008.*

[186] J. Haase. *Chem. in unserer Zeit, 26, 219–231, 1992.*

[187] Filter transmission, 2010. http://henke.lbl.gov/optical_constants/filter2.html. (last opened june, 2019).

[188] M. Deutsch, G. Hoelzer, J. Haertwig, J. Wolf, M. Fritsch, and E. Foerster. *Physical Review A, 51, 283–296, 1995.*

[189] W. Heisenberg. *Zeitschrift fuer Physik A, 43, 172–198, 1927.*

[190] Dectris high-energy sensors. .
Dectris High energy sensors. . (last opened june, 2019).

[191] Dectris pilatus hybrid pixel technology for your laboratory. .
Dectris Pilatus Hybrid Pixel Technology for Your Laboratory. . (last opened june, 2019).

[192] Dectris pilatus 1m hybrid pixel technology: User manual-pilatus2 v1.4.
Dectris Pilatus 1M Camera Manual. . (last opened june, 2019).

[193] Amptek. X-ray and gamma Ray Detector of high resolution CdTe (Cadmium Telluride): XR-100T-CdTe.

[194] Xr-100cdte x-ray detector. .
Amptek. 100CdTe X-Ray and gamma ray detector . (last opened june, 2019).

[195] U. Shymanovich, M. Nicoul, K. Sokolowski-Tinten, A. Tarasevitch, C. Michaelsen, and D. Linde. *Applied Physics B, 92, 493-499, 2008.*

[196] P. Kirkpatrick and A. Baez. *Journal of the Optical Society of America, 38, 766–773, 1948.*

[197] M. Silies, H. Witte, S. Linden, J. Kutzner, I. Uschmann, E. Foerster, and H. Zacharias. *Applied Physics A, 96, 59–67, 2009.*

[198] N. Zhavoronkov, Y. Gritsai, M. Bargheer, M. Woerner, T. Elsaesser, F. Zamponi, I. Uschmann, and E. Foerster. *Optics Letters, 30, 1737–1739, 2005.*

[199] E. Fill, J. Bayerl, and R. Tommasini. *Review of Scientific Instruments, 73, 2190-2192, 2002.*

[200] T. K. Cheng, S. D. Brorson, A. S. Kazeroonian, J. S. Moodera, G. Dresselhaus, M. S. Dresselhaus, and E. P. Ippen. *Applied Physics Letters, 57, 1004–1006, 1990.*

[201] E. Möhr-Vorobeva A. Caviezel G. Ingold S. L. Johnson, P. Beaud and C. J. Milne. *Physical Review B, 87, 054301, 2013.*

[202] G. Sciaini J. Matsuo G. Moriena, M. Hada and R. J. Dwayne Miller. *Journal of Applied Physics, 111, 043504, 2012.*

[203] H. J. Zeiger, J. Vidal, T. K. Cheng, E. P. Ippen, G. Dresselhaus, and M. S. Dresselhaus. *Physical Review B, 45, 768–778, 1992.*

[204] D. M. Collins. *Nature, 298, 49-51, 1982.*

[205] M. Sakata and M. Sato. *Acta Crystallogr. Sec. A, 46, 263–270, 1990.*

[206] M. Bocher. *Annals of Mathethematics, 7, 81–152, 1906.*

[207] P. Coppens. X-ray charge densities and chemical bonding. international union of crystallography. *Oxford Science Publications, Oxford, 1997.*

[208] E. T. Jaynes. *Physical Review, 106, 4, 1957.*

[209] E. T. Jaynes. *IEEE Transactions on Systems Science and Cybernetics, 4 , 227-241, 1968.*

[210] R. J. Papoular. *Acta Cryst. A, 48, 244-246, 1992.*

[211] L. Palatinus and S. v. Smaalen. Baymem user manual (2005). http://www.crystal.uni-bayreuth.de/en/baymem/index.html.

[212] Baymem user handbook http://www.cdifx.univ-rennes1.fr/RECIPROCS/juin2012/TP/MEM/BayMEM_manual.pdf.

[213] A. Cavalleri, C. W. Siders, F. L. H. Brown, D. M. Leitner, C. Tóth, J. A. Squier, C. P. J. Barty, K. R. Wilson, K. Sokolowski-Tinten, M. Horn von Hoegen, D. von der Linde, and M. Kammler. *Physical Review Letters, 85, 586–589, 2000.*

[214] C. v. Korff Schmising. Phd thesis: Femtosecond x-ray scattering in condensed matter. *Mathematisch-Naturwissenschaftliche Fakultät, Humboldt-Universität zu Berlin, Berlin, 2008.*

[215] V. M. Fridkin. *Crystallography Reports, 46, 654–658, 2001.*

[216] G. Czycholl. Theoretische festkörperphysik (band 1, grundlagen): Phononen und elektronen in kristallen. *Springer-Verlag, Berlin, 2015.*

[217] R. Ruppin. *Surf. Sci., 34, 20, 1973.*

[218] G. Folpini, K. Reimann, M. Woerner, and T. Elsaesser. *Phys. Rev. Lett., 119, 097404, 2017.*

[219] L. Von Grafenstein, M. Bock, D. Ueberschaer, E. Zawilski, P. Schunemann, U. Griebner, and T. Elsaesser. *Optics Letters, 42, 3796-3799, 2017.*

[220] L. Von Grafenstein, M. Bock, D. Ueberschaer, U. Griebner, and T. Elsaesser. *Optics Letters, 41, 20, 2016.*

[221] Jana software. http://jana.fzu.cz/.. (last opened, june 2019).

[222] International union of crystallography. https://www.iucr.org/.
cif files: https://www.iucr.org/resources/cif/spec.

[223] M. Holtz, C. Hauf, A.-A. Hernandez, R. Costard, M. Woerner, and T. Elsaesser. *Phys. Rev. B, 94, 1043021-1043027, 2016.*

[224] R. A. Cowley. Soft modes. *Ferroelectrics, 53, 27-31, 1984.*

[225] D. Dougherty. Interpretive barriers to successful product innovation in large firms. *Organization science, 3, 179–202, 1992.*

[226] A. Sirenko, C. Bernhard, A. Golnik, A. M. Clark, J. Hao, W. Si, and X. Xi. Soft-mode hardening in $SrTiO_3$ thin films. *Nature, 404, 373–376, 2000.*

[227] P. J. Brown, A. G. Fox, E. N. Maslen, M. A. O'Keefe und B. T. M. Willis. Intensity of diffracted intensities (chapter 6.1). *Mathematical, physical and chemical tables Band C in International Tables for Crystallography. International Union of Crystallography, Chester, 2006.*

[228] S. F. Gull and G. J. Daniell. *Nature, 272, 686–690, 1978.*

[229] J. Soulié, G. Renaudin, R. Cerny and K. Yvon. *Journal of alloys and compounds, 346, 200-205, 2002.*

[230] M. Born. Das adiabatenprinzip in der quantenmechnik. *Z. Phys., 40, 167, 1926.*

[231] M. Born. *Zeitschrift für Physik, 51, 165-180, 1928.*

[232] P. G. De Gennes. *Solid State Commun., 1, 132, 1963.*

[233] D. McKie and C. McKie. Essentials of crystallography. *Blackwell Scientific Publications, Oxford, 1992.*

[234] E. Prince (Editor). Mathematical, physical and chemical tables band c in international tables for crystallography. *International Union of Crystallography, Chester, 2006.*

[235] D. T. Cromer and J. B. Mann. *Acta Crystallographica A, 24, 321-324, 1968.*

[236] Atomic form factors. *Technische Universität Graz*
Atomic Form Factors-TU Graz. . (last opened june, 2019).

[237] D. E. Sands. Introduction to crystallography. *Dover Publications, Mineola (N.Y.), 1993.*

[238] H. Haensel and W. Neumann. Physik: Bd. 4, moleküle und festkörper. *Spektrum Akad. Verl., Heidelberg, 1996.*

Publications List

- *Shift-current-induced strain waves in $LiNbO_3$ mapped by femtosecond X-Ray Diffraction.*
  M. Holtz, C. Hauf, A. Hernandez, R. Costard, M. Woerner, and T. Elsaesser
  Phys. Rev. B 94, 104302/1-7 (2016), doi:10.1103/PhysRevB.94.104302
  https://link.aps.org/doi/10.1103/PhysRevB.94.104302

- *Towards shot-noise limited diffraction experiments with table-top femtosecond hard x-ray sources.*
  Marcel Holtz, Christoph Hauf, Jannick Weisshaupt, Antonio-Andrés Hernández Salvador, Michael Woerner, and Thomas Elsaesser
  Structural Dynamics 4, 054304 (2017)
  https://doi.org/10.1063/1.4991355

- *Soft-mode driven polarity reversal in ferroelectrics mapped by ultrafast x-ray diffraction.*
  Christoph Hauf, Antonio-Andrés Hernández Salvador, Marcel Holtz, Michael Woerner, and Thomas Elsaesser
  Structural Dynamics 5, 024501 (2018)
  https://doi.org/10.1063/1.5026494

- *Phonon driven charge dynamics in polycrystalline acetylsalicylic acid mapped by ultrafast x-ray diffraction.*
  Christoph Hauf, Antonio-Andrés Hernández Salvador, Marcel Holtz, Michael Woerner, and Thomas Elsaesser
  Structural Dynamics 6, 014503 (2019)
  https://doi.org/10.1063/1.5079229

Acronyms and Terminology

Abbreviation	Description
XRD	X-Ray Diffraction
MBI	Max Born Institut
AS	Ammonium Sulphate
CPA	Chirped Pulse Amplification
UC	Unit Cell
FT	Fourier-Transformation
HHG	High Harmonic Generation
OPA	Optical parametric amplifier
OPCPA	Optical Parametric Chirped Pulse Amplifier
MEM	Maximum Entropy Method
BayMEM	Software application based on the Maximum Entropy Method
SNR	Signal-to-noise ratio
Ω_{UC}	Volume of the Unit Cell

Declarations

I declare that I have produced this doctor's thesis independently using only the literature and the tools I have specified, in accordance with section 7 para. 3 of the Faculty of Mathematics and Natural Sciences PhD regulations, published in the Official Gazette of Humboldt-Universität zu Berlin (*Amtliches Mitteilungsblatt*) no. 126/2014 on 18/11/2014.

I have not applied for a doctoral degree in the doctoral subject of Physics elsewhere, and I do not hold a doctoral degree in the doctoral subject of Physics.

I have taken due note of the Faculty of Mathematics and Natural Sciences PhD Regulations, published in the Official Gazette of Humboldt-Universität zu Berlin (*Amtliches Mitteilungsblatt*) no. 126/2014 on 18/11/2014.

Berlin, 26th June 2019 Antonio Andrés Hernández Salvador

Appendix

BayMEM Software

The methodology to derive the transient charge density with the help of the BayMEM software is described in this section.

To derive the transient charge densities, BayMEM needs as inputs the Static and Transient Structure Factors which are calculated from the measured variations of diffracted intensity by applying the procedure explained in Section 3.6. As previously stated in Section 4.5.1, the spatial-resolution of the Static and Transient Structure Factors needs to be reduced to avoid the appearance of artefacts due to the Gibbs phenomenon ([206]).

Other of the crucial elements of the MEM theory is the proper division of the Unit Cell in smaller polyhedra to facilitate the calculations of the BayMEM software. The key concept in the subdivision of the Unit Cell is the so-called *voxel*: it consists of an element in a three-dimensional grid that, which has associated a numerical value for the electronic charge density and with which we can represent its volumetric display. The number of voxels in which the unit cell is divided is calculated as: $N_{voxel} = N_a \cdot N_b \cdot N_c$, where N_a, N_b and N_c, correspond to the number of divisions for the x-, y- and z-axes respectively.

It is essential to properly set the number of voxels in which the Unit Cell is divided since the BayMEM Suite will not produce sensible results if certain operational rules are not followed (described in the BayMEM Handbook, Ref.[212]).

The user BayMEM software handbook outlines the conditions that the choosing of numer of voxels for the Unit Cell have to comply with:
BayMEM USER HANDBOOK

The distribution results generated by the BayMEM program are given in a simple text '*.dat' format in accordance with the pre-defined subdivision of the Unit Cell in voxels.

To better illustrate the process, in Fig. 5.33 can be seen a general summary of the whole procedure taking as starting point the Resolution-Reduced Static and Transient Structure Factors. The BayMEM software generates the transient electronic charge density by using as inputs the Reduced Static Structure Factors, and Transient Reduced Structure Factors.

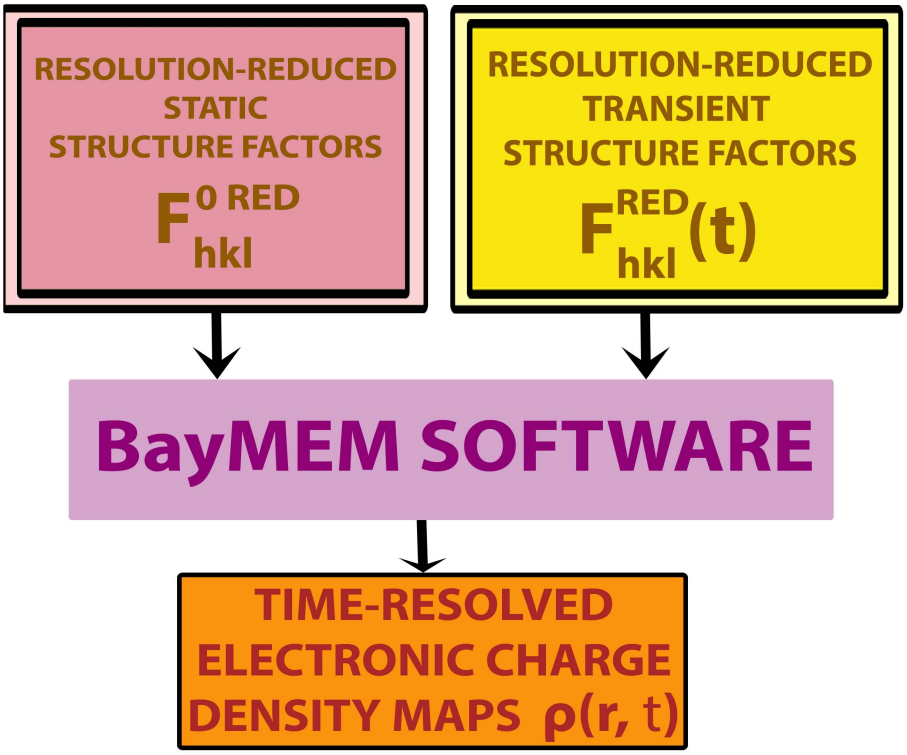

Figure 5.33: General Scheme describing the BayMEM working methodology. By following it, BayMEM can derive the transient electronic density by working with two sets of data as input: one is the Static Reduced Structure Factors, and the second is the Transient Reduced Structure Factors.

In the following, the whole proceeding is described in detail. Generally speaking, it consists of two differentiated stages:

- Firstly, the BAYMEM program generates the Degraded Prior Solution.
- Secondly, the BayMEM program generates the estimated transient electronic density ([152, 211]).

Calculation of Reduced Static (or Ground State) Charge Density

This section consists of the description of the algorithm to obtain the Reduced Static (or Ground State) Charge Density distribution (also Prior or Initial Solution in the language of the Maximum Entropy Method). The general concept is summarized in Figure 5.34, where it can be seen that the BayMEM program generates the Reduced Static Charge Density Distribution from the Static Reduced Structure Factors, and from the so-called 'Flat Prior Solution'. As mentioned before, this corresponds to the situation described in Figure 5.34, where there is no initial solution which is why to circumvent this problem, an initial solution is constructed artificially. It consists of a homogeneous distribution over all the space, i.e., a distribution characterized by having the highest possible entropy. To create the Flat Prior density, simply, the number of electrons in the Unit Cell are divided by the number of voxels in which the Unit Cell is divided, and finally every voxel in the Unit Cell is assigned with that fraction of electrons.

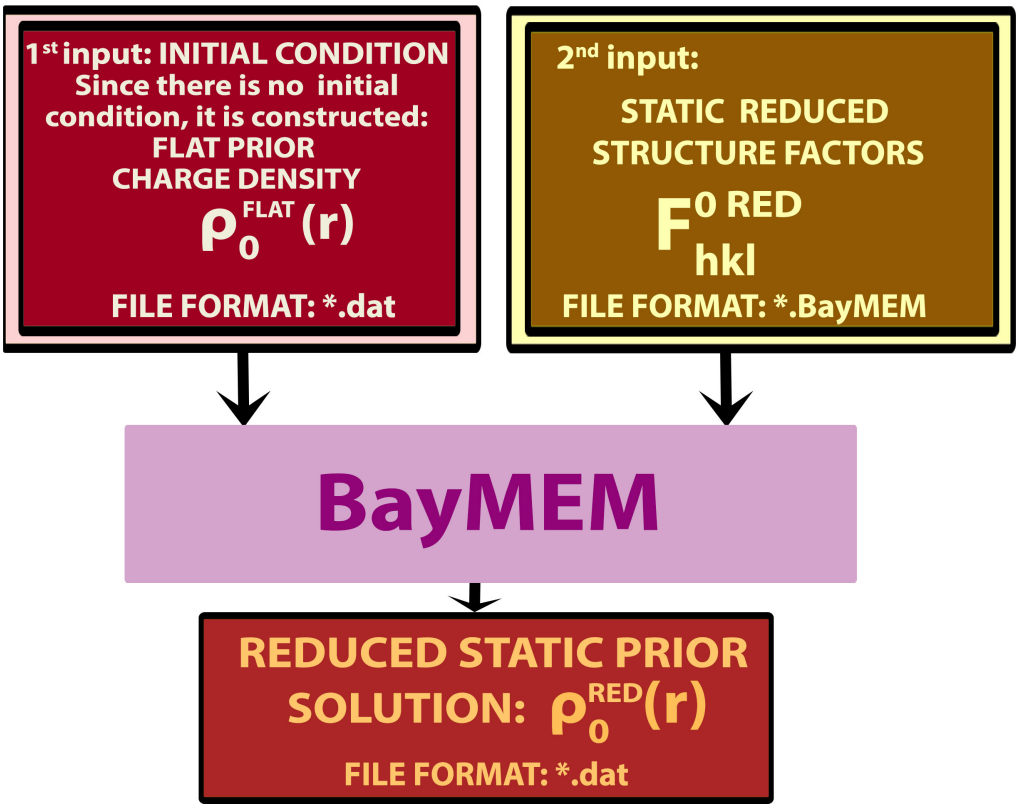

Figure 5.34: Schematic drawing of the general BAYMEM operation: it generates de Reduced Prior Distribution by taking as inputs the Flat Prior Distribution, and the Static Reduced Structure Factors.

In Figure 5.35 and Fig. 5.36, all the steps of which the process consists of can be seen:

1. The process starts with the *Crystallographic Information File* (CIF, *.cif), which is a format research-dedicated Standard text file that contains the relevant crystallographic information for a certain material. Its acronym stands for 'Crystallographic Information File' and/or 'Crystallographic Information Framewor', and it is designed and promoted and by the **International Union of Crystallography**
   https://www.iucr.org/.

   Its goal is to secure coherent exchange of crystallographic information.
   The formal specifications to standardize CIF files can be found in:
   https://www.iucr.org/resources/cif/spec

   The CIF file for ferroelectric Ammonium Sulphate was found in the Crystallography Open Database:
   http://www.crystallography.net/cod/search.html

2. After obtaining the CIF file, the Jana Computing System is used. It consists of a commonly-used freeware focused in solving and interpreting crystallographic structures ([221]). The CIF file is loaded into Jana, thereby generating a file called Crystallographic.BayMEM[1], where the file

[1] Jana, and the BayMEM software usually produce random file names without any significance. To avoid ambiguities and mistakes, we rename those files with the names as described in this section.

format *.BayMEM is the one required by the BayMEM program. MEM contains different crystal structure characteristics and a list of the the calculated Static Structure Factors.

3. The next step consist in extracting the list of Static Structure Factors and reducing their resolution by multiplying them by the gaussian factor described in Section 4.5.1:

$$\mathbf{F}_{\mathbf{hkl}}^{0\,RED} = \mathbf{F}_{\mathbf{hkl}}^{0} \cdot exp\{-ln(2) \cdot (\mathbf{q}_{\mathbf{hkl}}/q_{max})^2\} \tag{5.4}$$

4. Subsequently, a *.BayMEM file is built with the original crystallographic information which also contains the new list of resolution-reduced Structure Factors. This file is given the name of Reduced_Crystallographic.BayMEM to avoid ambiguities.

5. Finally, the BayMEM program is executed with the Flat Prior Distribution and the Static Reduced Structure Factors as inputs, with which the file called 'DEGRADED_PRIOR_DISTRIBUTION.dat' is obtained. As can be seen, it is given in a '*.dat' format that consists of a simple text file which contains the values of the electronic charge density values associated to their corresponding pre-defined voxels.

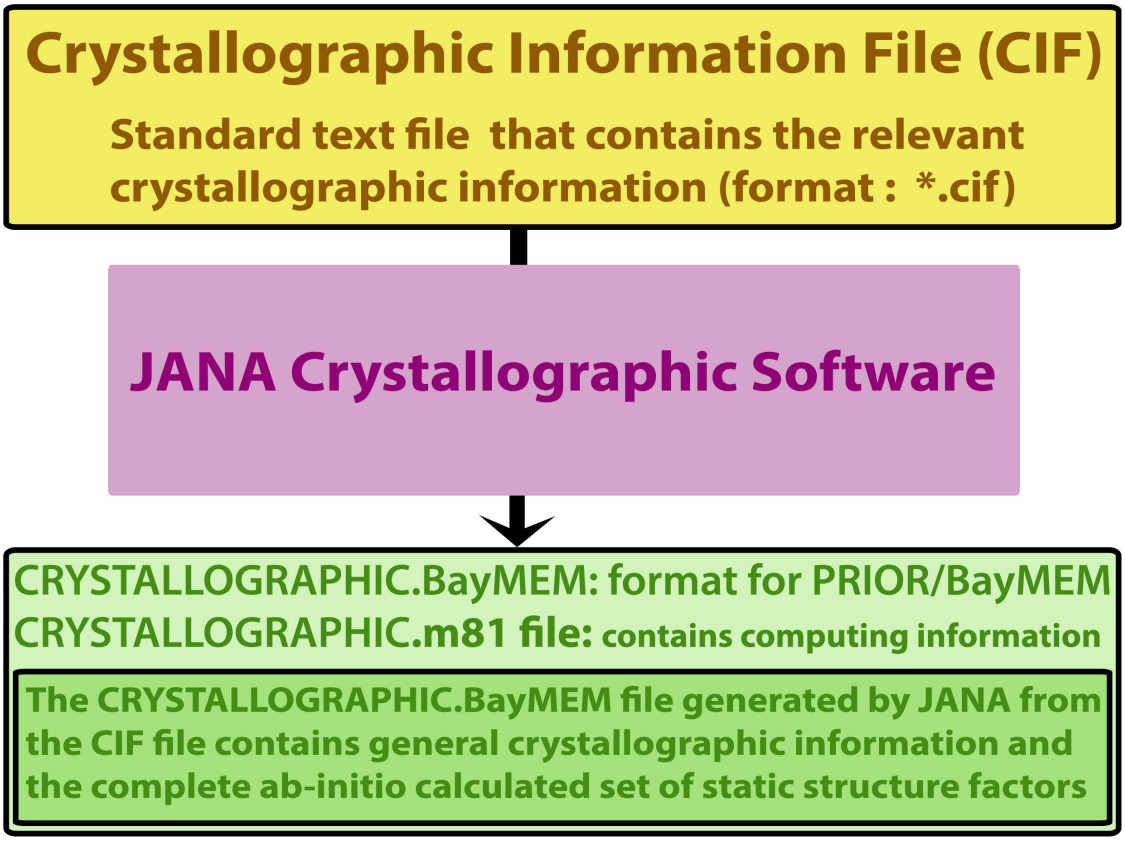

Figure 5.35: Algorithm that explains the generation of the *.BayMEM file with the CIF File as input by means of JANA. As output, JANA generates the so-called 'crystallographic.BAYMEM' file which contains the information of the structure of the crystal and the calculated static structure factors. JANA also produces another file (with format *.m81) with information of the computing process.

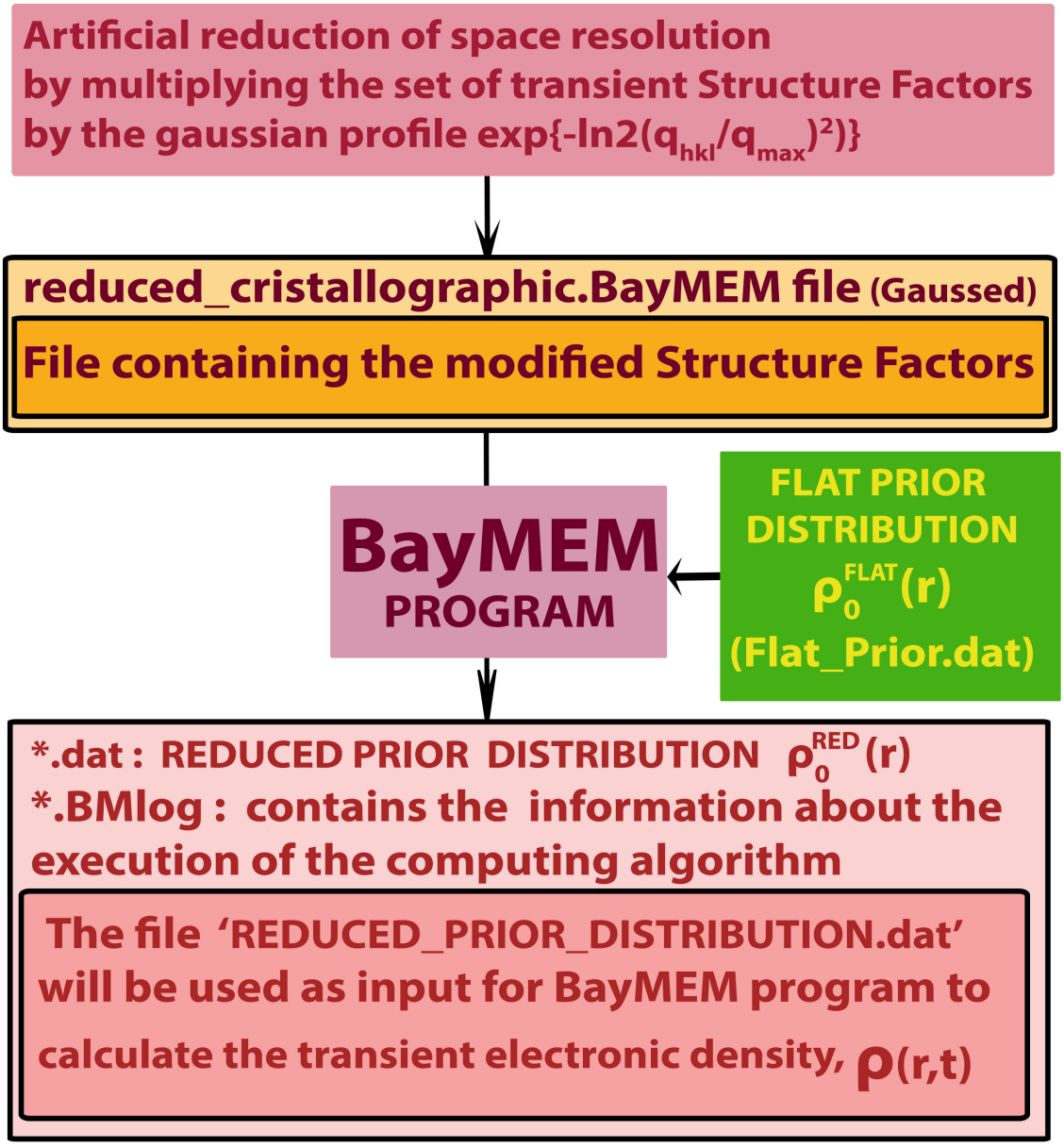

Figure 5.36: Algorithm to obtain the Degraded Prior Distribution.

In the flux diagram in Figure 5.37 an inclusive summary of the whole process of deriving the Degraded Prior Distribution is presented.

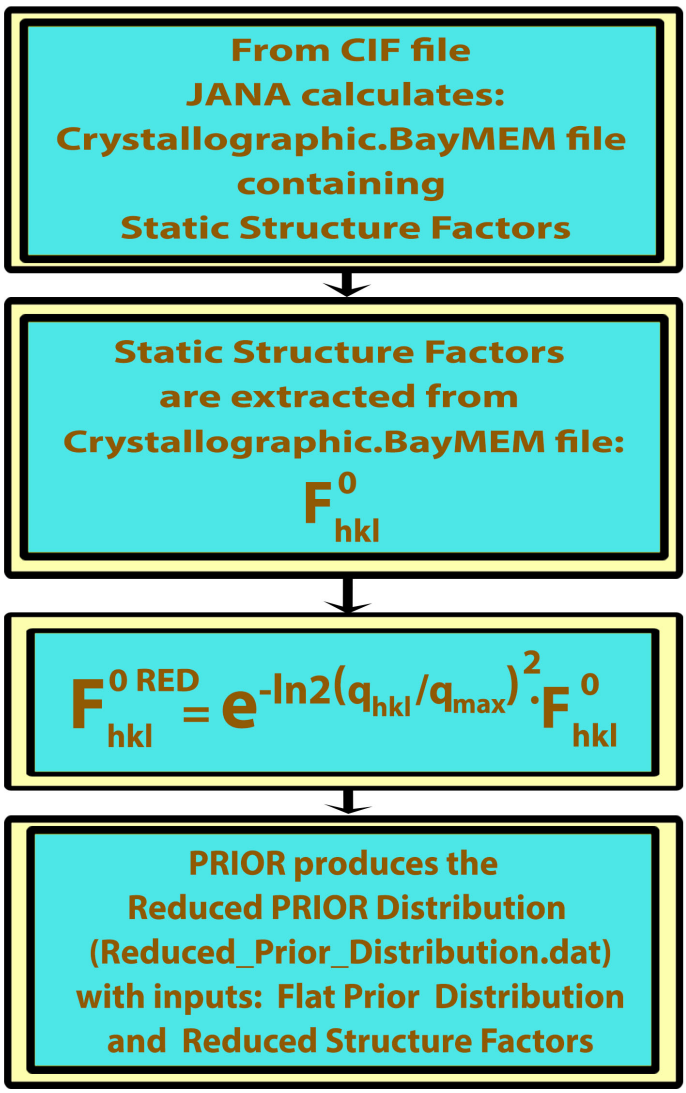

Figure 5.37: Fundamental stages of the algorithm to derive the Reduced Prior Solution from the initial CIF file.

App.: Calculation of the transient Reduced Structure Factors

In the flux diagram in Figure 5.38, all the steps to derive the Transient Reduced Structure Factors from the experimentally measured variations of diffracted intensity are presented.

1. Firstly, the Transient Structure Factors have to be derived from the measured variations of diffracted intensity by applying the procedure explained in Section 3.6.
2. Subsequently, the spatial resolution of the Transient Structure Factors needs to be reduced by multiplying them by the gaussian factor (as previously described in Section 4.5.1):

$$\mathbf{F}^{RED}_{\mathbf{hkl}} = \mathbf{F}_{\mathbf{hkl}}(t) \cdot exp\{-ln(2) \cdot (\mathbf{q}_{\mathbf{hkl}}/q_{max})^2\} \tag{5.5}$$

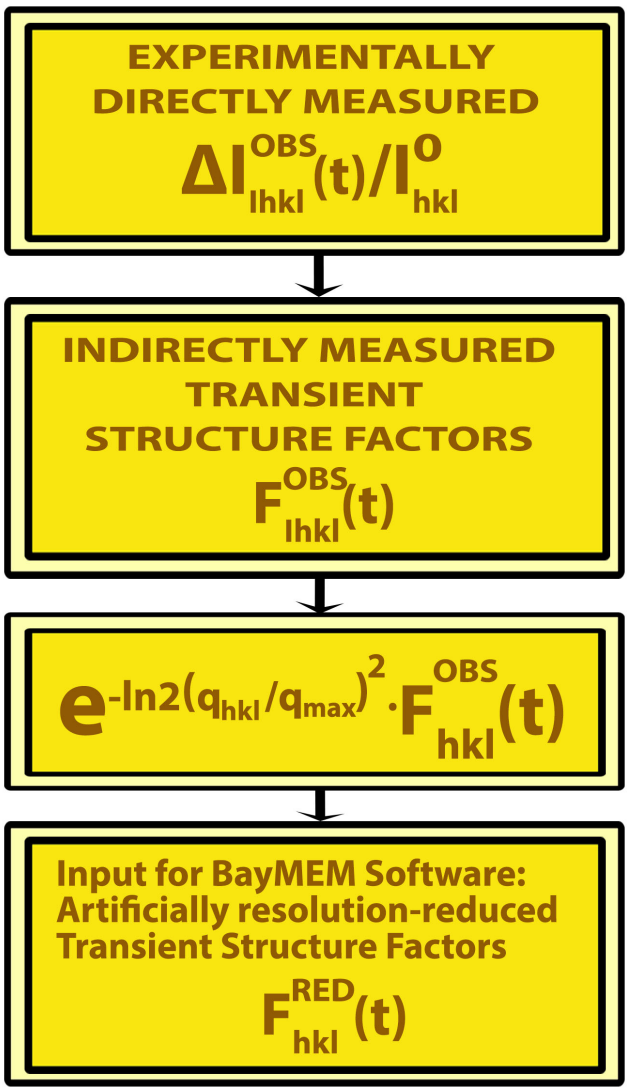

Figure 5.38: Scheme of the algorithm to derive the Transient Reduced Structure Factors from the measured variations of diffracted intensity.

Calculation of transient electronic charge density

3. Finally, the BayMEM program is executed with the Reduced Prior Distribution and the Transient Reduced Structure Factors as inputs, generating as output the transient elecronic density (file called TRANSIENT_ELECTRONIC_DENSITY.dat). As can be seen, the generated charge density maps have the same file format as the Reduced Prior Distribution (i.e., initial static charge density map), consisting of a *.dat file that associates the values for the electronic density to their respective voxels in the Unit Cell.

The general concept is summarized in Figure 5.39, where it can be seen how the BayMEM program generates the electronic transient density maps from the measured variation of diffracted intensity and the Reduced Static Charge Distribution.

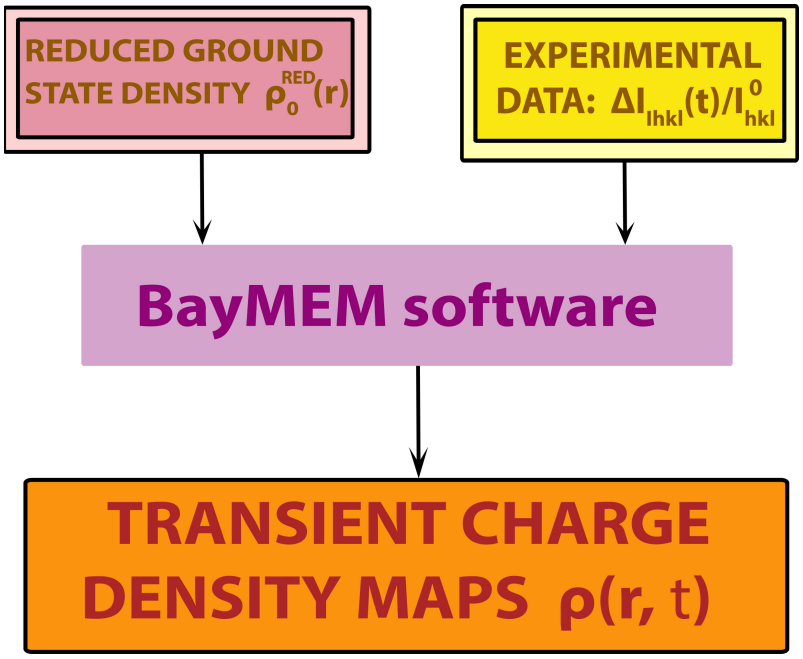

Figure 5.39: Depiction of the fundamental stages to derive the transient electronic charge density from the Reduced Prior Distribution and the measured variations of diffracted intensity.

5.6.1 App.: *.BayMEM Files

The BayMEM software makes use of the *.BayMEM format file, which is a text file that contains different general information about the structure of the crystal, e.g., the definition of the unit cell, the space group, the symmetry operations or the positions of the atoms in the unit cell, and it also contains a complete list with the structure factors.

There are a few questions to clarify about the *.BayMEM format:

- The *.BayMEM file format consists of a text file that contains different general crystallographic information of the material as can be the definition of the unit cell, the space group, the symmetry operations, the positions of the atoms in the unit cell, etc. and it also contains a list with the complete set of Structure Factors for the material.

- In the case of the file Crystallographic.BayMEM that is generated by JANA from the ferroelectric Ammonium Sulphate CIF file, it contains the crystallographic information of ferroelectric Ammonium Sulphate and the list of the complete set of ab-initio calculated Structure Factors for the unexcited state.

There is a full description of the BayMEM files and the generation of transient charge densities in: http://www.cdifx.univ-rennes1.fr/RECIPROCS/juin2012/TP/MEM/BayMEM_manual.pdf.

5.6.2 App.: Generation of Charge Density Maps

To generate the charge density maps, the BayMEM software makes use of the *.BayMEM format file. It is in the content of this file that the specifications needs to be set to ensure that the Initial Reduced Charge density is used as starting point to calculate the transient charge density maps.
The actual procedure takes place in two steps (we asume the name of the file is MaterialXXX.MEM):

In the first step, we execute the command (without the extension *.BayMEM):

BayMEM MaterialXXX ENTER

and we obtain the file MaterialXXX.asc, which contains the charge density distribution, and the file MaterialXXX.BMlog, which is a log file that contains the information of the BayMEM execution.

Now, as a second step we launch the command:

BayMEM2Dat MaterialXXX.asc ENTER

and we obtain a final Transient_Electronic_Density.dat which is a text file that contains the values of the electronic charge density maps associated to their corresponding pre-defined voxels. Also, another file that gives the information about the process is produced (*.m81).

List of Figures

List of Tables

Acknowledgements

I would like to thank my PhD supervisor Prof. Dr. Thomas Elsässer for giving me the opportunity of pursuing my PhD in the Max Born Institute. I would like to express my gratitude for his inspirational guidance, his patience and his motivation. I would also like to thank the rest of my thesis committee, i.e., Prof. Dr. Kurt Busch, Prof. Dr. Oliver Benson, Prof. Dr. Matias Bargheer, and Prof. Dr. Christoph Koch for their insightful commentaries.

I feel a sense of deep gratitude for the head of my department Dr. Michael Woerner and for Dr. Christoph Hauf, their deep understanding of physics and crystallography has contributed essentially to the success of this work.

Finally, I would also like to express my heartfelt thanks to Dr. Marcel Holz, Dr. Azize Koç, Dr. Shekhar Priyadarshi and Prof. Dr. Klaus Reinmann for their friendly working environment, and for their constant encouragement and support.